Synthesis and Characterization of Novel Sustainable Dual Crosslinked Sodium Carboxymethyl Cellulose Aerogels

by

Özge Payanda Konuk

A Dissertation Submitted to the
Graduate School of Sciences and Engineering in
Partial Fulfillment of the Requirements for
the Degree of

Doctor of Philosophy

in

Material Science and Engineering

KOÇ ÜNİVERSİTESİ

April 3, 2024

Synthesis and Characterization of Novel Sustainable Dual Crosslinked Sodium Carboxymethyl Cellulose Aerogels

Koç University

Graduate School of Sciences and Engineering

This is to certify that I have examined this copy of a doctoral dissertation by

Özge Payanda Konuk

and have found that it is complete and satisfactory in all respects,
and that any and all revisions required by the final
examining committee have been made.

Committee Members:

Prof. Dr. Can Erkey (Advisor)

Asst. Prof. Erkan Şenses

Research Asst. Prof. Selmi Erim Bozbağ

Asst. Prof. Zeynep Ülker Demir

Asst. Prof. Hamed Yousefzadeh

Date: 03.04.2024

To my family,

ABSTRACT

Synthesis and Characterization of Novel Sustainable Dual Crosslinked Sodium Carboxymethyl Cellulose Aerogels

Özge Payanda Konuk

Doctor of Philosophy in Material Science and Engineering

April 3, 2024

Aerogels are remarkable nanoporous materials with unique properties such as low density, high porosity, high specific surface area, and interconnected pore networks. In addition, their ability to be synthesized from various precursors such as inorganics, organics, or hybrid, and the tunability of their properties make them very attractive for many applications such as adsorption, thermal insulation, catalysts, tissue engineering, and drug delivery. The physical and chemical properties and pore structure of aerogels are crucial in determining their application areas. Moreover, it is possible to tailor the aerogel properties to meet the specific requirements of each application.

Synthesis of novel carboxymethyl cellulose (CMC) aerogels for thermal insulation applications is an essential area of research in finding alternative sustainable insulation materials instead of petroleum-based ones. Previous studies have been mainly focused on polysaccharide aerogels, especially cellulose aerogels. Although extensive research has been carried out on cellulose ether hydrogels or films, cellulose ethers and the effects of their functional groups on gelation mechanism, aerogels' morphology, and thermal properties have not been widely investigated. Moreover, when these cellulose ethers are used to synthesize aerogels, their functional groups can play a crucial role in controlling the morphology of the resulting aerogel. Modifying the synthesis parameters such as solvent choice, concentration, pH, and temperature makes it possible to tune the interactions between cellulose ethers and the solvent, leading to the formation of aerogels with tailored morphologies. Furthermore, adding crosslinking agents or other additives can also influence cellulose ether-based aerogels' gelation kinetics and final morphology. This tunability makes cellulose ether-based aerogels promising materials for various applications, including insulation, drug delivery, and tissue engineering.

The objective of this study is to synthesize CMC aerogels and also, at the same time, preserve their 3D porous structure and shape. To obtain CMC hydrogels with a 3D porous structure, the freeze-thaw induced gelation method was used and effecting factors were investigated. Since CMC aerogels obtained via supercritical drying have not been studied extensively in the literature, solvent exchange conditions for CMC hydrogels were determined. We aimed to elucidate the pore size distribution, specific surface area, and porosity of these novel materials, thereby paving the way for future exploration of

their potential applications in diverse fields. Our work expands the available synthesis methods for CMC aerogels and provides crucial insights into their fundamental pore characteristics, contributing to the ongoing development of sustainable and environmentally friendly aerogels.

In this study, sustainable maleic anhydride crosslinked CMC aerogels were synthesized by freeze-thaw induced gelation method. The effect of precursor concentration, crosslinker concentration, and gelation parameters on the aerogel properties, such as density, volumetric shrinkage, surface area, pore diameter, and thermal properties, were investigated. The prepared aerogels exhibited low density between 0.051 g/cm^3 and 0.204 g/cm^3, high porosity (> 93%), and high specific surface areas up to 214 m^2/g. The crosslinking mechanisms in CMC aerogels were examined by Fourier Transform Infrared Spectroscopy (FTIR) and Nuclear Magnetic Resonance (NMR) analysis. The lowest thermal conductivity was measured as 0.038 W/mK. A theoretical equation was also developed to calculate the thermal conductivity of aerogels. The results indicated that it is possible to tune the aerogel properties by adjusting biopolymer or crosslinker concentration and changing the freeze-thaw parameters.

PVA was incorporated into CMC aerogels to promote intermolecular crosslinking and, therefore, reduce the pore diameter. CMC/PVA hybrid aerogels from 4 and 6 wt% aqueous solutions were prepared, and the porous structures of hybrid aerogels were investigated. CMC/PVA hybrid aerogels had low bulk density and high porosity (> 95%). FTIR and NMR analyses were conducted to confirm the esterification reaction. The thermal conductivity of CMC/PVA hybrid aerogel was measured as 0.055 W/mK.

Finally, sulfuric acid catalyzed aerogels were synthesized, and it was seen that it is possible to reduce the gelation time with an acid catalyst. The effect of acid concentration on the aerogel properties, such as density, volumetric shrinkage, surface area, pore diameter, and thermal properties, was investigated. The crosslinking reaction was confirmed by FTIR analysis. Contrary to expectations, sulfuric acid catalyzed aerogels had low porosity, low surface area, and high pore size. However, these results shed light on the potential to tailor aerogel properties using acid catalysts precisely. These findings provide valuable insights for optimizing aerogel synthesis tailored to specific applications.

ÖZETÇE

Yenilikçi Sürdürülebilir Çift Çapraz Bağlı Sodyum Karboksimetil Selüloz Aerojellerin Sentezi ve Karakterizasyonu

Özge Payanda Konuk

Malzeme Bilimi ve Mühendisliği, Doktora

3 Nisan 2024

Aerojeller, düşük yoğunluk, yüksek gözeneklilik, yüksek yüzey alanı ve birbirine bağlı ağsı nano boyuttaki gözenek yapıları ile benzersiz özelliklere sahip malzemelerdir. Ayrıca, inorganic ve organik çeşitli öncüllerden sentezlenebilmeleri veya hibrit yapılabilmeleri, yapısal özelliklerinin istenilen uygulamalara göre ayarlanabilirliği, aerojellerin adsorpsiyon, termal yalıtım, katalizör, doku mühendisliği ve ilaç taşınımı gibi birçok uygulamada kullanımını sağlar. Aerojellerin fiziksel, kimyasal ve yapısal özellikleri, uygulama alanlarının belirlenmesinde önemlidir ve aerojelleri farklı uygulamaların isterlerini karşılayacak şekilde geliştirmek mümkündür.

Isı yalıtımı uygulamaları için yenilikçi karboksimetil selüloz (CMC) aerojellerinin sentezi, petrol bazlı olanlar yerine alternatif sürdürülebilir yalıtım malzemeleri bulma konusunda önemli bir araştırma alanıdır. Literatürdeki önceki çalışmalar esas olarak polisakkarit aerojellere, özellikle de selüloz aerojellere odaklanmıştır. Selüloz eter hidrojelleri veya filmleri üzerinde kapsamlı araştırmalar yapılmasına rağmen, selüloz eterler ve fonksiyonel gruplarının jelleşme mekanizması, aerojellerin morfolojisi ve termal özellikleri üzerindeki etkileri geniş çapta araştırılmamıştır. Bu fonksiyonel gruplar elde edilen aerojellerin morfolojisinin kontrol edilmesinde çok önemli bir rol oynayabilir. Çözücü seçimi, konsantrasyon, pH ve sıcaklık gibi sentez parametrelerinin değiştirilmesi, selüloz eterler ile çözücü arasındaki etkileşimlerin ayarlanmasını mümkün kılarak özel morfolojilere sahip aerojellerin oluşumuna yol açabilir. Ayrıca çapraz bağlayıcı ajanların veya diğer katkı maddelerinin eklenmesi, selüloz eter bazlı aerojellerin jelleşme kinetiğini ve morfolojisini de etkileyebilir. Selüloz eter aerojellerin özelliklerinin bu şekilde modifiye edilebilir olması bu aerojelleri ısı yalıtımı, ilaç taşınımı ve doku mühendisliği gibi çeşitli uygulamalar için umut verici malzemeler haline getirmektedir.

Bu çalışmanın amacı 3 boyutlu gözenek yapısına sahip CMC aerojel sentezlemektir. Bu amaçla, donma-çözülme ile indüklenen jelleşme yöntemi ile CMC hidrojel elde edilmiştir ve bu yöntemi etkileyen faktörler araştırılmıştır. Süperkritik kurutma yoluyla elde edilen CMC aerojeller henüz literatürde kapsamlı bir şekilde araştırılmamıştır, bu nedenle CMC hidrojelleri için solvent değişimi koşulları belirlenmiştir. Bu çalışmadaki amacımız, CMC aerojellerin gözenek boyutu özelliklerini, spesifik yüzey alanını ve gözenekliliğini incelemek ve böylece farklı alanlardaki potansiyel uygulamalarının gelecekte araştırılmasının önünü açmaktır. Bu çalışma aynı

zamanda, CMC aerojeller için yeni bir sentez yöntemi sunmaktadır ve CMC aerojellerin temel gözenek özelliklerine ilişkin önemli bilgiler sağlayarak sürdürülebilir ve çevre dostu aerojellerin süregelen gelişimine katkıda bulunmaktadır.

Bu çalışmada, maleik anhidrit çapraz bağlı CMC aerojeller, donma-çözülme ile indüklenen jelleşme yöntemi ile sentezlenmiştir. Öncül konsantrasyonu, çapraz bağlayıcı ajan konsantrasyonu ve jelleşme parametrelerinin, yoğunluk, hacimsel küçülme, yüzey alanı, gözenek çapı ve termal özellikler gibi aerojel özelliklerinin üzerindeki etkileri incelenmiştir. Sentezlenen aerojellerin 0,051 g/cm^3 ile 0,204 g/cm^3 arasında düşük yoğunluğa, yüksek gözenekliliğe (> %93) ve 214 m^2/g'a kadar yüksek spesifik yüzey alanına sahip olduğu gözlemlenmiştir. CMC aerojellerindeki esterleşme reaksiyonu Fourier Dönüşümü Kızılötesi Spektroskopisi (FTIR) ve Nükleer Manyetik Rezonans (NMR) analizleri ile incelenmiştir. En düşük termal iletkenlik katsayısı ise 0,038 W/mK olarak ölçülmüştür. Aerojellerin termal iletkenlik katsayılarını hesaplamak için teorik bir denklem geliştirilmiştir. Sonuçlar, biyopolimer veya çapraz bağlayıcı ajan konsantrasyonunu ayarlayarak ve donma-çözülme parametrelerini değiştirerek aerojel özelliklerini ayarlamanın mümkün olduğunu göstermiştir.

Moleküller arası çapraz bağlanmayı arttırmak ve dolayısıyla gözenek çapını azaltmak için CMC aerojellerine PVA eklenmiştir. Ağırlıkça %4 ve %6 sulu çözeltilerden CMC/PVA hibrit aerojeller hazırlanmıştır ve hibrit aerojellerin gözenekli yapıları incelenmiştir. CMC/PVA hibrit aerojellerinin düşük yoğunluğa ve yüksek gözenekliliğe (> %95) sahip olduğu gözlemlenmiştir. Esterleşme reaksiyonlarını doğrulamak için FTIR ve NMR analizleri yapılmıştır. CMC/PVA hibrit aerojelinin termal iletkenliği ise 0,055 W/mK olarak ölçülmüştür.

Son olarak, CMC aerojeller katalizör olarak sülfürik asit kullanılarak sentezlenmiştir ve böylece jelleşme için gereken sürenin azaldığı görülmüştür. Sülfürik asit konsantrasyonunun yoğunluk, hacimsel küçülme, yüzey alanı, gözenek çapı ve termal özellikler gibi aerojel özelliklerine etkisi araştırılmıştır. Çapraz bağlanma reaksiyonu FTIR analizi ile doğrulanmıştır. Beklenenin aksine, sülfürik asit eklenen aerojellerin düşük gözenekliliğe, düşük yüzey alanına ve yüksek gözenek boyutuna sahip olduğu görülmüştür. Ancak bu sonuçlar doğrultusunda, asit katalizör kullanarak aerojellerin jelleşme sürelerinin, gözenek özelliklerinin ve dolayısıyla termal özelliklerinin optimize edilebileceği anlaşılmıştır.

ACKNOWLEDGEMENTS

First and foremost, I would like to express my sincere gratitude to my thesis advisor, Prof. Can Erkey, for giving me the opportunity to pursue a Ph.D. under his guidance and expertise. I am truly grateful for his support, encouragement, and patience. I have learned so much from him, especially from the challenging questions that made me understand more about science and engineering. His mentorship has been invaluable, and it was an honor to work with Prof. Erkey and be one of his Ph.D. students.

I would like to acknowledge the financial support of the Scientific and Technological Research Council of Turkey (TÜBİTAK) under project no. 118C124 and Koç University during my graduate study. I also would like to thank Arçelik A.Ş. This study would not be possible without their funding.

I acknowledge the support provided by Koç University Surface Science and Technologies Center (KUYTAM) for SEM images. I also acknowledge the use of the services and facilities of n2STAR-Koç University Nanofabrication and Nanocharacterization Center for Scientific and Technological Advanced Research for NMR analysis. I am also grateful to Ashland Specialty Ingredients for kindly providing samples.

I would like to sincerely thank my thesis committee members, Asst. Prof. Zeynep Ülker Demir and Asst. Prof. Erkan Şenses for their insightful feedback and constructive criticism. I would like to express my appreciation to my thesis committee members, Asst. Prof. Selmi Erim Bozbağ and Asst. Prof. Hamed Yousefzadeh for accepting to be a committee member.

My sincere thanks to my colleagues in Energy Technologies and Supercritical Fluids Research Group, Dr. Selmi Erim Bozbağ, Dr. Işık Sena Akgün Güldür, Dr. Şansım Bengisu Barım, Dr. Hande Güneş, Dr. Zeynep İnönü, Dr. Hamed Yousefzadeh, Tarık

Bercan Sarı, Ala Alsuhile and Ayça Tüter.

I am very grateful for my dear friends Tuğba Yalçın, İlayda Terzi, Asım Önal, and Güncem Özgün Eren. We have always tried to keep ourselves motivated during our coffee breaks. It would be impossible to finish this degree without their friendship and support.

I am extremely grateful to my lovely parents and brother for all the love, support, encouragement, and patience. They have always been great role models; I still have much to learn from them. I am grateful to my grandmother for all the love and support. I am also thankful to my grandmother and grandfather, who have passed away. I know you are always watching me, and I hope you are proud of me. I also would like to thank my mother-in-law, father-in-law, and sister-in-law for their continuous support and faith in me.

Last but not least, I express my deepest appreciation to my husband, the love of my life, for his endless love, support, patience, and encouragement. It would only be possible to complete my Ph.D. with him by my side. Thank you for being the sunshine even in the darkest of times.

Contents

ABSTRACT iv
ÖZETÇE vi
ACKNOWLEDGEMENTS viii
Contents x
LIST OF FIGURES xii
LIST OF TABLES xiv
ABBREVIATIONS xv
CHAPTER 1 INTRODUCTION 1
1.1 Energy Consumption in White Goods 3
CHAPTER 2 LITERATURE REVIEW 2
2.1 Aerogels 2
2.2 Synthesis of Aerogels 2
2.3 Solvent Exchange 3
2.4 Drying Techniques 5
2.4.1 Ambient pressure drying 5
2.4.2 Freeze drying 5
2.4.3 Supercritical drying 6
2.5 Classification of Aerogels 7
2.5.1 Inorganic 7
2.5.2 Organic 8
2.5.3 Carbon 9
2.5.4 Hybrid 10
2.5.5 Composite 10
2.6 Cellulose and Cellulose Ethers 11
2.7 Crosslinkers and cellulose ether hydrogels 13
2.8 Freeze-Thaw Induced Gelation 15
2.9 Heat Transfer Mechanisms in Aerogels 16
2.10 Solid Thermal Conductivity 17
2.11 Gaseous Thermal Conductivity 21
2.12 Radiative Thermal Conductivity 24
2.12.1 Optically thick approximation 25
CHAPTER 3 EXPERIMENTAL METHODS AND CHARACTERIZATION TECHNIQUES 27
3.1 Materials 27
3.2 Thermogelation of cellulose ethers 27
3.3 Freeze-thaw induced gelation of cellulose ethers 28

3.4 Synthesis of sodium carboxymethyl cellulose hydrogels 28
3.5 Optimization of solvent exchange conditions and supercritical drying of alcogels 30
3.6 CMC/PVA hybrid aerogels 30
3.7 Sulfuric acid catalyzed CMC aerogels 31
3.8 Characterization of Aerogels 31
CHAPTER 4 RESULTS AND DISCUSSION 34
4.1 Determination of gelation temperature of cellulose ethers 34
4.2 Freeze-thaw induced gelation of cellulose ethers and effect of crosslinkers 36
4.3 Determination of freeze-thaw induced gelation conditions for CMC 38
4.4 Effect of solvent exchange conditions 39
4.5 Freeze-Thaw induced gelation of CMC solutions 40
4.5.1 Effect of frozen storage time and crosslinker concentration on gelation 40
4.5.2 Effect of CMC molecular weight and concentration on gelation 42
4.6 Morphology of CMC aerogels 43
4.6.1 Effect of frozen storage time and crosslinker concentration on morphology 43
4.6.2 Effect of molecular weight and concentration on morphology 48
4.7 Crosslinking of CMC aerogels 53
4.8 Thermal properties of CMC aerogels 57
4.9 Effect of intermolecular crosslinking on CMC aerogels 59
4.9.1 Morphology of CMC/PVA hybrid aerogels 60
4.9.2 Crosslinking of CMC/PVA hybrid aerogels 64
4.9.3 Thermal properties of CMC/PVA hybrid aerogels 66
4.10 Effect of acid catalyst on CMC aerogels 66
4.10.1 Morphology of sulfuric acid catalyzed CMC aerogels 67
4.10.2 Crosslinking of acid catalyzed CMC aerogels 70
4.10.3 Thermal properties of sulfuric acid catalyzed CMC aerogels 71
CHAPTER 5 CONCLUSION 72
Bibliography 74
Appendix 88

LIST OF FIGURES

Figure 1.1. Largest end uses by sector (IEA, 2018) [2] 1
Figure 1.2. Shares of residential energy consumption by end use (IEA, 2018) [2] 2
Figure 2.1. Hydrolysis and polycondensation sol-gel processing 3
Figure 2.2. General synthesis of biopolymer aerogels 3
Figure 2.3. Chemical structure of cellulose. Adapted from the reference [77]. 11
Figure 2.4. Etherification reactions of cellulose. Adapted from the references [82][81]. 12
Figure 2.5. Chemical structure of cellulose ether. Adapted from the reference [81]. ... 12
Figure 2.6. Chemical structure of sodium carboxymethyl cellulose. Adapted from the reference [84] 13
Figure 2.7. Chemical structure of citric acid. Adapted from the reference [87] 14
Figure 2.8. Chemical structure of oxalic acid. Adapted from the reference [90] 14
Figure 2.9. Chemical structure of maleic anhydride. Adapted from the reference [94] 14
Figure 2.10. 1, macromolecules in a solution; 2, solvent; 3, low-molecular solutes; 4, polycrystals of frozen solvent; 5, unfrozen liquid microphase; 6, polymeric framework of a cryogel; 7, macropores; 8, solvent [105]. 15
Figure 2.11. Heat transfer mechanisms in a porous media [112]. 17
Figure 2.12. Solid unit structure model of silica aerogel [70]. 19
Figure 3.1. The schematic illustration of the experimental procedure used to determine the gelation temperatures of cellulose ethers. 28
Figure 3.2. Schematic illustration of the CE hydrogel synthesis. 28
Figure 3.3. Schematic illustration of the CMC aerogel synthesis 29
Figure 4.1. a) 6 wt% HPMC solution b) Heating HPMC solution c) Gelation of HPMC solution at 72 °C d) HPMC gel 35
Figure 4.2. Prepared hydrogels a) CMC and b) CMC/PVA hybrid 38
Figure 4.3. Effect of frozen storage time on the number of FT cycles 39
Figure 4.4. The change in the mass loss of CMC aerogels with the solvent exchange process. 40
Figure 4.5. Photos of CMC aerogels from 6 wt % CMC solutions. 41
Figure 4.6. Effect of crosslinker concentration and frozen storage time on the number of FT cycles. 41
Figure 4.7. Photos of CMC aerogels from different CMC types and concentrations. ... 42
Figure 4.8. Effect CMC molecular weight and CMC concentration on the number of FT cycles. 43
Figure 4.9. Volumetric Shrinkage of CMC aerogels. 44
Figure 4.10. Densities of CMC aerogels. 44
Figure 4.11. BET Isotherms of CMC aerogels a) 8h frozen storage b) 24h frozen storage. 45
Figure 4.12. Mesoporous pore size distributions of CMC aerogels a) 8h frozen storage b) 24h frozen storage. 46
Figure 4.13. S_{BET} as a function of the crosslinker concentration. 47
Figure 4.14. SEM images of CMC aerogels. a) L6_MA1.2_8h b) L6_MA1.2_24h c) L6_MA1.8_8h d) L6_MA1.8_24h e) L6_MA2.4_8h f) L6_MA2.4_24h, 10KX magnification. 48
Figure 4.15. Densities of CMC aerogels from different CMC sources and aqueous concentrations. 49

Figure 4.16. BET Isotherms of CMC aerogels from a) 6 wt% CMC aqueous solution b) 4 wt% CMC aqueous solution. 50
Figure 4.17. Mesoporous pore size distributions of CMC aerogels from a) 6 wt% CMC aqueous solution b) 4 wt% CMC aqueous solution. 51
Figure 4.18. SEM images of CMC aerogels a) L6_MA1.8_8h b) M6_MA1.8_8h c) M31F6_MA1.8_8h d) H6_MA1.8_8h, 20KX magnification. 52
Figure 4.19. SEM images of CMC aerogels a) L4_MA1.2_8h b) M4_MA1.2_8h c) M31F4_MA1.2_8h d) H4_MA1.2_8h, 10KX magnification. 52
Figure 4.20. S_{BET} as a function of the CMC sources and aqueous concentrations. 53
Figure 4.21. The proposed crosslinking mechanism between CMC-CMC-MA. 54
Figure 4.22. FTIR spectra of CMC and MA. 54
Figure 4.23. FTIR spectra of MA crosslinked CMC aerogels. 55
Figure 4.24. a) The chemical structure of NaCMC b) The solid-state 13C-NMR spectrum of CMC aerogel. 56
Figure 4.25. FTIR spectra of CMC aerogels from 6 wt% aqueous CMC concentration. 56
Figure 4.26. FTIR spectra of CMC aerogels from 4 wt% aqueous CMC concentration. 57
Figure 4.27. Thermal Conductivities of the CMC aerogels from a) different crosslinker concentrations and frozen storage times and b) different CMC sources and aqueous concentrations. 58
Figure 4.28. Theoretical thermal conductivity values of CMC aerogels. 59
Figure 4.29. A photo of CMC/PVA hybrid aerogel. 60
Figure 4.30. Volumetric Shrinkage of CMC and CMC/PVA hybrid aerogels. 60
Figure 4.31. Densities of CMC and CMC/PVA hybrid aerogels. 61
Figure 4.32. BET Isotherms of CMC/PVA hybrid aerogels from a) 4 wt% aqueous solution b) 6 wt% aqueous solution. 62
Figure 4.33. Mesoporous pore size distributions of CMC/PVA hybrid aerogels. 63
Figure 4.34. SEM images of CMC/PVA hybrid aerogels a) from 4 wt% aqueous concentration b) from 6 wt% aqueous concentration, 10KX magnification. 63
Figure 4.35. The proposed crosslinking mechanism between CMC-PVA-MA. 64
Figure 4.36. FTIR spectra of CMC, PVA and MA. 64
Figure 4.37. FTIR spectra of MA crosslinked CMC/PVA hybrid aerogels. 65
Figure 4.38. a) The chemical structure of PVA b) The solid-state 13C-NMR spectrum of CMC/PVA hybrid aerogel. 66
Figure 4.39. The sulfuric acid catalyzed a) hydrogel b) alcogel c) aerogel. 67
Figure 4.40. Volumetric shrinkages and densities of sulfuric acid catalyzed CMC aerogels. 67
Figure 4.41. BET Isotherms of sulfuric acid catalyzed CMC aerogels. 68
Figure 4.42. Mesoporous pore size distributions of sulfuric acid catalyzed CMC aerogels. 69
Figure 4.43. SEM images of sulfuric acid catalyzed CMC aerogels (a,c) 0.175M and (b,d) 0.35M. 70
Figure 4.44. FTIR spectra of sulfuric acid catalyzed CMC aerogels. 71

LIST OF TABLES

Table 2.1. Alkyl groups of cellulose ethers [82][83]. 12
Table 3.1. Formulations of prepared CMC aerogels. 29
Table 4.1. Summary of the prepared cellulose ether solutions with citric acid and oxalic acid and their gel formation. 36
Table 4.2. Summary of the prepared cellulose ether solutions with citric acid and oxalic acid and their gel formation. 37
Table 4.3. Properties of CMC aerogels. 45
Table 4.4. Properties of CMC aerogels from different CMC sources and aqueous concentrations. 49
Table 4.5. Properties of CMC and CMC/PVA hybrid aerogels. 61
Table 4.6. Properties of sulfuric acid catalyzed CMC aerogels. 68
Table 4.7. The thermal conductivities of sulfuric acid catalyzed CMC aerogels 71

ABBREVIATIONS

BET	Brauner, Emmet and Teller
BJH	Barret, Joyner and Halenda
c	Speed of light
CA	Citric acid monohydrate
CE	Cellulose Ether
CMC	Carboxymethyl cellulose
C_v	Specific heat at constant volume
DS	Degree of substitution
EC	Ethyl cellulose
EtOH	Ethanol
E_s	Rosseland mean extinction coefficient
$E_s(l)$	Spectral extinction coefficient
EU	European Union
FT	Freeze-Thaw
FTIR	Fourier transform infrared spectroscopy
h	Planck's constant
HEC	Hydroxyethyl cellulose
HPC	Hydoxypropyl cellulose
HPMC	Hydroxypropyl methylcellulose
IEA	International Energy Agency
$I_b(l)$	Spectral blackbody flux
I_b	Black-body flux
k_B	Stefan– Boltzmann constant
l	Radiation wavelength of photons

l_g	Mean free path of the gas molecules
MA	Maleic anhydride
MC	Methyl cellulose
NaCMC	Sodium carboxymethyl cellulose
NMR	Nuclear magnetic resonance
OA	Oxalic acid dihydrate
P_c	Critical pressure
P_r	Prandtl number
PVA	Polyvinyl alcohol
RT	Room temperature
S_{BET}	Specific surface area (m^2/g)
$scCO_2$	Supercritical carbon dioxide
SCF	Supercritical fluid
SEM	Scanning electron microscopy
T_c	Critical Temperature

Greek letters

α	Accommodation coefficient
β	Gas coefficient
γ	Adiabatic coefficient
K_n	Knudsen number
Λ_{ph}	Phonon mean free path
λ	Thermal conductivity
ϕ	Porosity
ρ	Density
v_{ph}	Phonon velocity
Θ_D	Debye temperature

τ_{ph}	Average relaxation time

CHAPTER 1 INTRODUCTION

Energy production and consumption are increasing around the world. Although the share of energy from renewable sources has been steadily increasing, 82% of the world's energy is still produced from coal, oil, and natural gas sources, according to the Energy Institute's 2022 data [1]. Using fossil fuels leads to the emission of greenhouse gases, which causes environmental pollution, global warming, and climate change. In addition, it threatens human health, nature and biodiversity.

Energy saving and sustainability are getting more and more attention to protect the environment and natural resources. For this purpose, the number of studies on developing products with low energy consumption is increasing. According to the International Energy Agency (IEA), residential energy consumption in the world accounts for 20% of all energy consumption, as shown in Figure 1.1.

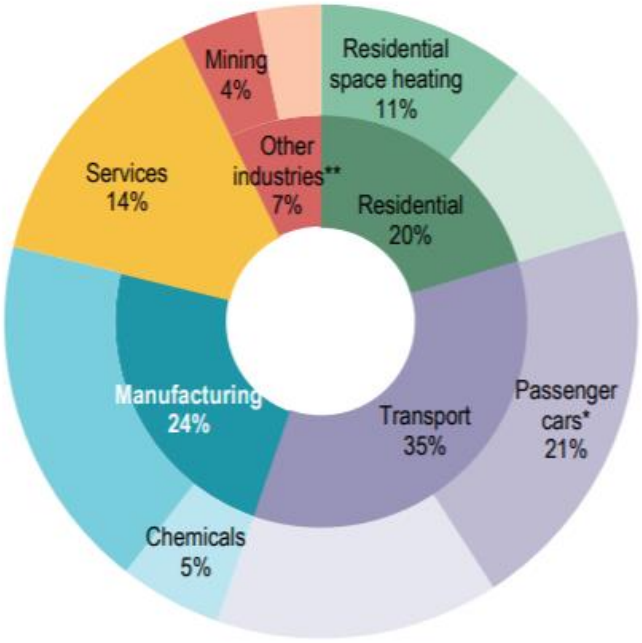

Figure 1.1. Largest end uses by sector (IEA, 2018) [2]

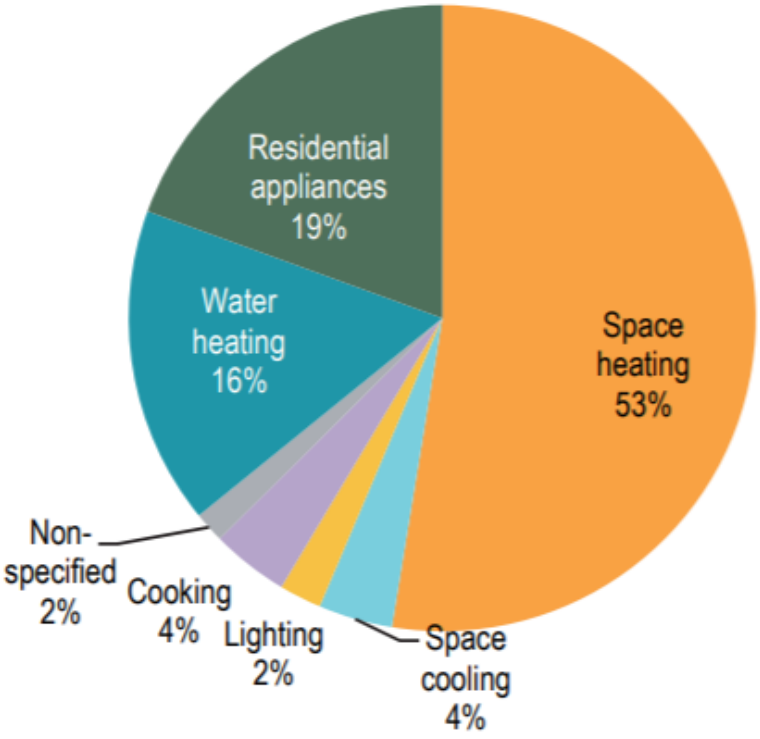

Figure 1.2. Shares of residential energy consumption by end use (IEA, 2018) [2]

The breakdown of residential energy consumption is given in Figure 1.2. It indicates that residential appliances, including refrigerators/freezers, dishwashers, clothes washers and dryers, televisions, home entertainment devices, computers, other information technology devices, and other small home appliances account for 19% of total residential energy consumption [2].

Therefore, energy-saving measures in residential appliances are being enforced by regulations. European Union (EU) energy labels have been in use since 1994 and are important guides for consumers when purchasing electrical appliances. The other aim of EU energy labels is to encourage manufacturers to develop products that consume less energy. For this purpose, energy levels were created from A to G, with A being the best category. With improving technology, manufacturers began to develop more energy-efficient products. As the energy efficiency of the new products exceeded the efficiency of products with the energy levels A, A +, A ++, and even A +++ were added to the classification system. In addition, some products with lower categories (E, F, G) have become less preferred or been removed due to eco-design requirements.

To raise consumer awareness and encourage the industry to develop products that consume less energy, the European Commission established a simpler scale of EU energy

labels in which only the letters A to G are used (Regulation (EU) 2017/1369). The new regulations are also much stricter in terms of energy consumption. For example, according to the new labeling, a refrigerator with an A +++ label in the old system has a C label, although it is as energy efficient as before. As another example, an A ++ dishwasher has an E label [3].

For this reason, white good companies have been focused on improving the energy efficiencies of their products.

1.1 Energy Consumption in White Goods

Thermal insulation materials play a crucial role in white goods. They act as a barrier, preventing heat transfer between the appliance's internal and external environment. Thermal insulation materials are used to reduce energy consumption and improve the food preservation and lifespan of white goods by minimizing temperature fluctuations. There are several thermal insulation materials, such as polyurethane, vacuum insulation panels (VIP), expanded polystyrene (EPS), extruded polystyrene (XPS), glass wool, and rock wool, and the choice of thermal insulation material depends on the specific appliance, desired performance, and cost. In addition to conventional insulation materials, aerogels have recently been studied for potential applications in white goods [4]. Besides their outstanding thermal insulation properties, the fact that they can be produced from sustainable materials makes aerogels an attractive candidate.

This study introduces a novel approach to synthesizing CMC aerogels, utilizing a relatively non-toxic crosslinker and supercritical CO_2 drying and pioneering investigation into the thermal conductivity characteristics of CMC aerogels. Initially, we developed CMC hydrogels with a 3D porous structure using the freeze-thaw-induced gelation method. The prepared hydrogels were also chemically crosslinked by maleic anhydride to obtain mechanically strong and chemically stable gels. Stable gel means having a consistent and enduring structure, resisting deformation or breakdown during the removal from mold and solvent exchange process. Furthermore, we optimized the solvent exchange conditions to reduce the loss of the CMC polymer and enhance the strength of CMC alcogels. Upon supercritical drying, we investigated the pore morphology of CMC aerogels and evaluated the influence of precursor materials and preparation conditions on their structural properties. By employing a different gelation technique, we aimed to elucidate the impact of the gelation method on the resulting aerogel structure and,

consequently, its thermal behavior. We explored the effect of frozen storage duration on the gelation of CMC. Furthermore, we examined the impact of the molecular weight of CMC and the initial solution concentration on gelation, pore properties, and thermal conductivity. Through this comprehensive examination, we contributed significant insights into the synthesis and characterization of CMC aerogels for potential applications in various fields.

The synthesis techniques, classification, and properties of aerogels are given in Chapter 2. An extensive review of heat transfer mechanisms in aerogels is also presented.

Experimental methods are provided in Chapter 3, including the synthesis of carboxymethyl cellulose aerogel and the techniques used to characterize aerogels.

Experimental results of this study are presented in Chapter 4. This chapter includes the physical and thermal properties of CMC aerogels prepared from different CMC sources and insights into the effect of various synthesis conditions on aerogel properties. The physical and thermal properties of CMC/PVA hybrid aerogels and sulfuric acid catalyzed CMC aerogels are also included.

Chapter 5 concludes the study's outcomes and proposes insights for future investigation.

CHAPTER 2 LITERATURE REVIEW

2.1 Aerogels

Aerogels are solid, open porous networks formed by replacing the liquid phase in a gel with air. Inorganic and organic aerogels were first synthesized by Samuel Kistler in 1932 [5]. Since then, aerogels from various precursors have been studied. They can be classified based on their chemical compositions as inorganic (silica, alumina, titania), organic (resorcinol formaldehyde, cellulose, pectin), carbon (via pyrolysis of organic aerogels), and hybrid/composite aerogels. Aerogels have low density, high porosity, high specific surface area, and open porous structure [6,7]. These distinctive properties make them very attractive for many applications such as thermal insulation [8,9], acoustic insulation [10], solar systems [11], drug delivery [12][13], tissue engineering [14], catalysts and supports [15–22], adsorption [23–25], sensors [26], and energy conversion and storage applications [27,28].

Briefly, to produce an aerogel, first of all, a gel is formed. After that, the gel is aged and subjected to a series of solvent exchanges with a suitable solvent. Finally, the obtained wet gel is dried to obtain an aerogel.

2.2 Synthesis of Aerogels

The network structure of the gels, and therefore the properties of the aerogels, are affected by the properties of precursors and the reaction parameters of the gelation processes. Gels are prepared by sol-gel processing, and the type of sol-gel processing can be divided into two main sub-groups. One method is hydrolysis, followed by polycondensation reactions, which starts with the dissolution of a monomer in a solvent [29]. All of the inorganic aerogels (such as silica, alumina, and zirconium) and some organic aerogels, such as resorcinol–formaldehyde (RF) and melamine-formaldehyde (MF) aerogels, are prepared with this sol-gel processing (Figure 2.1) [30–32].

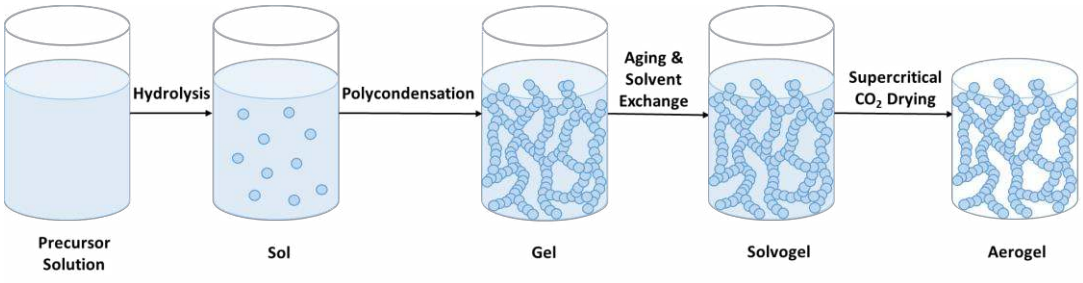

Figure 2.1. Hydrolysis and polycondensation sol-gel processing

The other method (Figure 2.2) is first dissolving the polymer in a solution and then regenerating the polymer network with physical crosslinking (such as temperature or pH) or chemical crosslinking. This method is generally used for biopolymer aerogels such as cellulose, alginate, starch, carrageenan, and pectin [13,29,33].

Figure 2.2. General synthesis of biopolymer aerogels

2.3 Solvent Exchange

One of the most crucial steps in the synthesis of aerogels is the solvent exchange, during which the pore liquid is exchanged with a solvent suitable for the subsequent drying method. During the process, not only is the pore filling liquid replaced, but all unreacted monomers, oligomers, and the solvent used in the synthesis are removed [34]. The solvent exchange, previously described in Kistler's initial work in the 1930s, is necessary to prepare intact, non-fractured aerogels at the end of the drying [5]. Drying the wet gels without solvent exchange or using non-suitable solvents would result in fractured and shrunken aerogels due to the creation of high capillary pressures inside the pores [35]. One method to decrease these high capillary pressures is to select a solvent with a lower interfacial surface tension [36] and replace pore filling liquid with this new solvent, thereby controlling how much the aerogel would shrink. The cause of this gel shrinkage, the most problematic part of the aerogel preparation, has also been indicated by Kistler as the exchange of water to organic solvent and supercritical drying [36].

Wet gels subjected to solvent exchange can either swell or shrink depending on the selection of different process parameters [37]. It is known that especially organic aerogels shrink to a greater extent [38] due to the formation of hydrogen bonds between

the polymer strands, leading to a denser network. A higher density, in turn, would affect some properties such as pore volume, surface area, thermal conductivity, and many others. Thus, to obtain better physical properties, it is of utmost importance to understand shrinkage.

If supercritical drying is used, solvent exchange is especially important for the gels that are prepared in aqueous solutions or in solvents that are not soluble in $scCO_2$ [39]. Thus, they should be exchanged with more suitable solvents, commonly alcohols or acetone, with lower critical points and chemical activities to perform supercritical drying under more convenient and economic conditions [36][40]. Moreover, the selected solvent should not destroy the structure of the wet gel by dissolving it or by any other means.

Since Kistler's time, the solvent exchange process has been carried out in the same manner by placing the synthesized wet gels in an excess new solvent (one step) or by performing a multistep procedure in which new solvent/water mixtures with increasing content of the solvent is used [36][41][42]. Although one-step solvent exchange seems to shorten the lengthy solvent exchange process, it usually causes a more drastic shrinkage [40][41]. That is why multi-step solvent exchange is commonly performed for various aerogels [40][41]. Using a mixture of solvents with water rather than the pure solvent reduces the concentration gradient on the gel, making gels more resistant to shrinkage. Thus, adding one or more intermediate steps in the solvent exchange with increasing solvent concentrations would result in lower shrinkage. However, the reduction in shrinkage will also depend on the solvent concentration and the number of solvent exchange steps. Even with changing the solvent exchange period from four to six concentration steps, the volume reduction was reduced by 25-30% [43]. Moreover, using lower initial concentrations of solvent resulted in reduced shrinkage even if it leads to a slower process [40]. Based on various factors affecting the solvent exchange, understanding its kinetics is a challenging task as the duration of the solvent exchange can vary significantly from hours to several days [34][39].

In conclusion, it is crucial to carefully select the solvent that will be used to wash the wet gels prior to drying. Another important point would be to know how much solvent exchange is necessary before drying the wet gels. In other words, it is critical to investigate the required concentration of the new solvent in the pores, considering both solvent recycling and final physical properties.

2.4 Drying Techniques

Drying the wet gels is the final step of aerogel synthesis, which includes replacing the solvent filling the gel pores with air while the original gel structure is preserved. Removal of the solvent from the gel pores can be problematic since the capillary stresses in these pores, originating from the gas-liquid phase boundary, can be significant due to the nano-sized pores in the gel structure. These capillary stresses can destroy the pores in terms of pore size and shape, collapse of the pores, and cracks in macroscopic gel structure [44]. Therefore, drying is a remarkably delicate step, where even slight variations in process conditions can result in the destruction of pores in the final product. Three methods can be used for drying the gels: ambient drying, freeze drying, and supercritical drying [35].

2.4.1 Ambient pressure drying

In ambient pressure drying, the liquid phase in the wet gel evaporates at ambient pressure and temperatures ranging from room temperature up to 200 °C, which is highly susceptible to making enormous changes in the gel structure and significant shrinkages [45]. During the evaporation of the liquid from the pores, a meniscus forms in the vapor-liquid interface. Due to this capillary pressure, the gel shrinks, forming a denser gel called xerogel [35]. Some studies for silica aerogels show that it is possible to reduce shrinkage by the spring-back effect, which is the re-expansion of the gel. The patent for this technique was issued in 1996. After the solvent exchange step, the hydroxyl groups on the internal surface of the alcogels were reacted with organic substances of the form R_xMX_y where R is usually an organic group such as CH_3, C_2H_5; M is Si or Al, and X is a halogen which is usually Cl. The replacement of hydrophilic hydroxyl groups with organic groups resulted in hydrophobic aerogels. This process was performed to modify the contact angle between the pore liquid and the pore walls during drying to reduce capillary stresses. During ambient pressure drying, a “spring back” effect was observed with the re-expansion of the wet gel since neighboring surface silyl groups were chemically inert and did not interact with each other [13]. In addition, the gel structure can be strengthened to stand the capillary pressure, or solvents with low surface tension can be used [46].

2.4.2 Freeze drying

Freeze drying is another method of drying the wet gels, during which the solvent

is extracted from the pores by sublimation. This occurs after freezing the gels below the solvent's freezing point and then decreasing the pressure below the sublimation pressure. After the sublimation of the solid in the pores, temperature, and pressure are brought to ambient conditions. The resulting gels are called cryogels. In this method, the destruction of the network may occur due to the stresses in the pore being applied during the freezing of the gels due to the growth of the solvent crystals, especially in the case of water, when it expands during the freezing. It can be further problematic when a solvent with an extremely low freezing point, such as ethanol, is used [45].

2.4.3 Supercritical drying

Supercritical drying is an alternative method for drying wet gels, where supercritical fluids (SCF) are used to extract the solvent from the pores of the gel network since these fluids do not have any interfaces in supercritical conditions. In this method, the solvent, usually an alcohol, is first dissolved in the diffused SCF inside the pores, where a single-phase binary mixture is formed. The continuous flow of fresh SCF drains the solvent of the pores, leading to a complete exchange of the solvent with SCF inside the pores. Subsequently, lowering the system pressure at temperatures above the critical temperature of the fluid leads to the removal of SCF from the pores without the formation of a phase boundary and huge capillary stresses, where the fluid phase inside the pores moves directly from supercritical to gas state without leaving any liquid solvent residue [35][47]. Liquid-like density along with gas-like viscosity of SCFs enable them to be used as promising solvents in supercritical drying where zero surface tension of SCF and the absence of a phase boundary during vessel depressurization significantly minimize the shrinkage and deformation of the gel network. Zero surface tension of SCFs avoids pore collapse and permits better penetration and wetting of pores than liquid solvents do [48]. Furthermore, enhanced mass transfer characteristics due to higher diffusion coefficients in SCFs than liquids make supercritical drying an efficient and harmless gel drying technique, resulting in aerogel products with higher porosity and surface area than those dried with ambient and freeze-drying methods [49][50].

In general, supercritical CO_2 ($scCO_2$) is used as supercritical fluid as CO_2 has easily accessible critical points (critical temperature 31°C and critical pressure 73.8 bar) [51]. Moreover, CO_2 is chemically inert, non-toxic, non-flammable, and low-cost.

The gels are first placed inside a high-pressure vessel filled with the parent solvent

and heated above the critical temperature of the $scCO_2$-solvent mixture. This is followed by pressurizing the vessel with the corresponding fluid up to the above critical pressure of the $scCO_2$-solvent mixture. Subsequently, the solvent is extracted from the gel pores, followed by opening the vessel outlet and continuously charging the fresh fluid. The mixture of $scCO_2$-solvent is finally flashed into a solvent collecting container at atmospheric pressure, which leads to the separation of CO_2 rich gas phase and the solvent-rich liquid phase from each other. This step is continued until the complete removal of the solvent from the gel, after which the vessel is discharged by closing the inlet valve and depressurization, during which the phase of CO_2 inside the gel pores is changed from $scCO_2$ to gas phase $CO_{2(g)}$. Finally, dried gels are removed from the vessel, after which air is gradually exchanged with $CO_{2(g)}$ inside the pores [45].

2.5 Classification of Aerogels

Based on their chemical compositions, aerogels can be classified as inorganic, organic, carbon, and hybrid/composite aerogels.

2.5.1 Inorganic

First inorganic aerogels were synthesized by Kistler through the sol-gel process and supercritical drying of gels of silica, alumina, tungsten oxide, ferric oxide, stannic oxide, and nickel tartrate [5]. Since then, various inorganic aerogels have been prepared [52]. Silica aerogels are the most extensively studied and used aerogels for thermal insulation due to their very low thermal conductivity. Sol-gel polymerization is the commonly employed method for preparing inorganic aerogels. Metal alkoxides such as tetraethylorthosilicate (TEOS) or tetramethylorthosilicate (TMOS) are the generally used chemical precursors for synthesizing silica aerogels. First, these precursors are hydrolyzed in a mixture of water and alcohol, where the alkoxide groups of the precursor are replaced with hydroxyl groups, as shown in Equation 2.1.

$$Si(OR)_4 + 4H_2O \leftrightarrow Si(OH)_4 + 4R - OH \quad (2.1)$$

Adding an acid or a base catalyst can accelerate the kinetics of the hydrolysis reaction. Subsequently, $Si(OH)_4$ molecules go through water (Equation 2.2) and alcohol (Equation 2.3) condensation reactions, forming a silica network. This step can be accelerated by the addition of a base catalyst.

$$\equiv Si - OH + HO - Si \equiv \rightarrow \equiv Si - O - Si \equiv + H_2O \quad (2.2)$$

$$\equiv Si - OR + HO - Si \equiv \rightarrow \equiv Si - O - Si \equiv + R - OH \quad (2.3)$$

The mixture finally forms a gel, which is mostly composed of SiO_2.

However, some side chains might remain unreacted (Si-OR) or partially reacted (Si-OH) at the end of the condensation reactions. These Si-OH groups render the aerogel hydrophilic and make it susceptible to water adsorption, leading to structural collapse. To improve the mechanical strength of these wet gels and to finish the hydrolysis and condensation reactions of unreacted precursors in the gels, they are placed in an aging solution consisting of water and alcohol. This step is necessary to obtain more compact structures which are more resistant to shrinkage and any damage. Then, the gel is subjected to a solvent exchange step, during which it is placed in a pure solvent, which is generally alcohol, to replace water and to remove any impurities remaining in the pores. The final step is to dry this wet gel, also called alcogel, without damaging its structure [13].

Other inorganic aerogels, such as titania aerogels, zirconia aerogels, and alumina aerogels, are prepared using the same sol-gel route but with different precursors. For instance, titania aerogels can be prepared from tetrabutyl ortho-titanate, titanium n-butoxide, and titanium tetraisopropoxide [13]. Zirconia aerogels can synthesized from zirconium n-propoxide and zirconium n-butoxide butanol complex [53]. Alumina aerogels are typically prepared from aluminum alkoxide precursors, such as aluminum isopropoxide or aluminum-tri-sec-butoxide [54][55].

2.5.2 Organic

Kistler also synthesized the first organic aerogels from cellulose, nitrocellulose, gelatin, agar, egg albumin, and rubber in 1932 [5]. In 1989, Pekala synthesized an organic aerogel by polycondensation of resorcinol–formaldehyde (RF) in an aqueous solution using Na_2CO_3 as a catalyst. The gelation mechanism was similar to silica's sol-gel processing, and he used supercritical CO_2 drying to obtain RF aerogel [31]. Since then, several organic aerogels have been prepared from different organic precursors such as melamine-formaldehyde, phenol-furfural, phenol-melamine and polyurethane, polyimide, poly(vinyl alcohol) and poly(vinyl chloride) [32][56]. The primary step is to form a hydrogel from an aqueous starting solution triggered by a cross-linking promoter, which can have either a chemical nature (chemical cross-linker) or a physical nature (pH, temperature) [41]. The subsequent step, the aging/solvent exchange step, involves

replacing the water within the porous structure with an appropriate solvent, usually alcohol. The next and final step is to dry the wet gel supercritically with carbon dioxide [13].

Furthermore, polysaccharide aerogels have attracted increasing attention in recent years since they are natural, abundant, renewable, biocompatible, biodegradable, and low-cost [57]. These polysaccharide aerogels are mostly synthesized from cellulose, cellulose derivatives, alginate, starch, pectin, chitin, and chitosan. As a result of their biocompatibility and biodegradability, polysaccharide aerogels are being investigated for use in tissue engineering, wound care applications, and drug delivery [13][41][58][59]. Among them, cellulose aerogels are also being investigated for thermal insulation applications [60].

2.5.3 Carbon

Carbon aerogels are prepared by pyrolyzing organic aerogels at elevated temperatures under an inert atmosphere. The first carbon aerogel was synthesized by Pekala by pyrolysis of RF aerogel at 1050 °C under an inert atmosphere, and RF is the most widely studied organic precursor [61]. Carbon aerogels can be fabricated by pyrolyzing bio-based aerogels [56][62]. In addition, there are also self-assembled carbon aerogels, which are graphene aerogels and carbon nanotube aerogels [63].

Carbon aerogels have high specific surface area, high porosity, low density, and significantly high electrical conductivity [56]. The structure of carbon aerogel can be manipulated by tuning the pyrolysis conditions such as temperature, heating rate, pressure, and duration [64]. For instance, between 600 °C and 900 °C, the aerogel's surface area and pore volume reduce as the pyrolysis temperature increases. Moreover, aerogels pyrolyzed at 1200 °C are much denser than those pyrolyzed at 600 °C. In addition, high pyrolysis temperature increases electrical conductivity [56][64].

Carbon aerogels are burned in oxidizing atmospheres; therefore, they should be used in an evacuated system, which also suppresses the gaseous thermal conductivity in the aerogel. Since carbon aerogels are good IR absorbers, radiative thermal conductivity is also reduced. Besides, the solid thermal conductivity of carbon aerogels is low due to high porosity and low density. Thus, the overall thermal conductivity of carbon aerogels is very low [64][65].

2.5.4 Hybrid

Hybrid aerogels are attracting increased attention due to their enhanced and multi-functional properties. These kinds of aerogels can be synthesized by polymerization during the sol step or after the gelation step. Hybrid aerogels are comprised of inorganic and organic components, and they are either formed by electrostatic forces, van der Waals forces, hydrogen bonding, or covalent bonds [66].

Several studies of hybrid aerogels have been conducted, such as polymethylmethacrylate-silica aerogels, cellulose-silica aerogels, and chitosan-silica aerogels. According to these studies, it can be deduced that combining inorganic and organic components improves the aerogel properties such as specific surface area, thermal conductivity, and Young modulus in comparison to individual aerogels [67][68][69].

2.5.5 Composite

There are also various studies on composite aerogels in which clay, SiO_2, carbon nanotube, cellulose nanofibrils, graphene, or graphene oxide are added to strengthen the structure of aerogels. In addition to better mechanical properties, it is possible to give new features to aerogels, such as hydrophobicity, lipophilicity, or electrical conductivity [56]. For instance, silica aerogels are rigid and brittle. Also, silica aerogels are transparent and adsorb moisture, which increases effective thermal conductivity [30]. Some nanoparticles or fibers, such as SiC and carbon fibers, have been added to overcome these drawbacks and improve mechanical and thermal properties.

Moreover, adding ZrO_2 and TiO_2 as an opacifier increases the thermal resistance of silica aerogels [70]. Clays in silica aerogel also enhance mechanical properties [71][72]. As another example, due to the brittleness and frailty of carbon aerogels, they are reinforced with carbon fibers, graphene, graphene oxide, and carbon nanotubes [64]. Additionally, carbon aerogels are incorporated with metal oxides, metal hydroxides, and metal sulfides to impart new properties for different applications [56].

In the last decade, metal−organic framework/aerogel composites (MOFACs) were introduced as a new class of composite aerogels. MOFs also have high surface area, high pore volume, high porosity, and low density. Therefore, integrating MOFs into aerogels leads to hierarchically porous materials with superior properties [73].

2.6 Cellulose and Cellulose Ethers

Among various polysaccharides, cellulose aerogels are the most investigated for thermal insulation applications [60][74]. Cellulose has a linear polymer chain structure without branching, linked by β-1,4-glycosidic bonds (Figure 2.3). Each glucose unit is rotated by 180° around its longitudinal axis, which forms a cellobiose disaccharide repeating unit. There are intramolecular hydrogen bonds between the C_3 hydroxy group and the adjacent to the ring oxygen, as well as between the C_2 hydroxy group and the hydroxymethyl group oxygen at C_6. This arrangement of the molecular chains forms intermolecular hydrogen bonds between oxygen atoms $O_{3'}$ … O_5 and O_2 … $O_{6'}$ [75]. Due to the extensive intra- and inter-molecular hydrogen bonding between these chains, cellulose shows a crystal lattice structure, resulting in insolubility in water and most organic solvents [76].

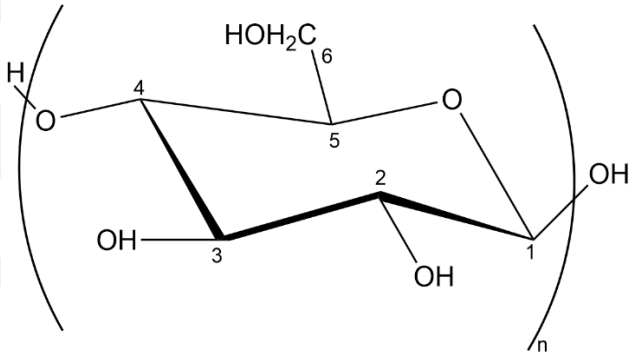

Figure 2.3. Chemical structure of cellulose. Adapted from the reference [77].

N-methylmorpholine N-oxide (NMMO) monohydrate, calcium thiocyanate octahydrate (CTO) [78], 8% NaOH–water solution [59], LiCl/DMAc [79], or ionic liquids such as 1-ethyl-3-methylimidazolium acetate (EMIMAc) and 1-butyl-3-methylimidazolium chloride (BMIMCl) are some of the solvents that are used to dissolve cellulose [80]. Many cellulose solvents pose significant hazards and present challenges in safe disposal. Additionally, their limited ability to fully dissolve cellulose complicates the investigation of high molecular weight and cellulose concentrations, thereby hindering the tailoring of aerogel properties.

To improve cellulose solubility in water, the cellulose chain's regularity and hydrogen bonding are decreased. For this purpose, cellulose is chemically modified by etherification or esterification reactions. The production of cellulose ethers involves the reaction between the hydroxyl groups of cellulose and either alkyl halides or epoxides in an alkaline environment (Figure 2.4) [81].

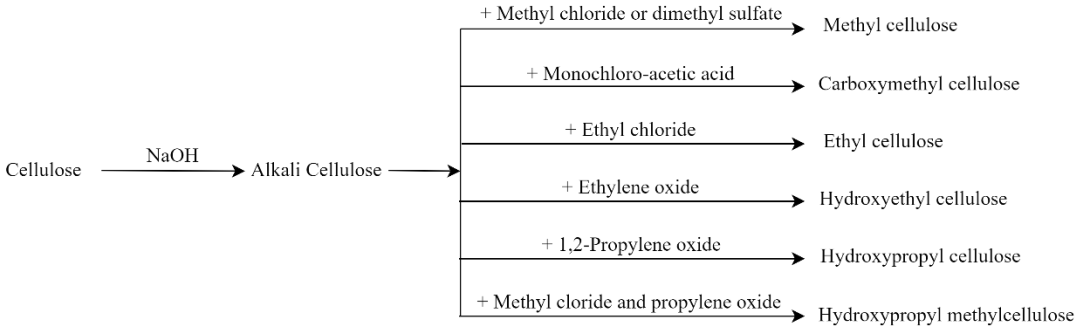

Figure 2.4. Etherification reactions of cellulose. Adapted from the references [82][81].

Cellulose ethers (CEs) are nontoxic, biodegradable, and biocompatible, and they are commonly used as thickeners, binders, stabilizers, and emulsifiers in various industries such as food, pharmaceuticals, cosmetics, and construction [82][81]. Different types of cellulose ethers have different -R groups, such as methylcellulose (MC), ethyl cellulose (EC), sodium carboxymethyl cellulose (NaCMC), hydroxyethyl cellulose (HEC), hydroxypropyl cellulose (HPC) and hydroxypropyl methylcellulose (HPMC) (Figure 2.5, Table 2.1).

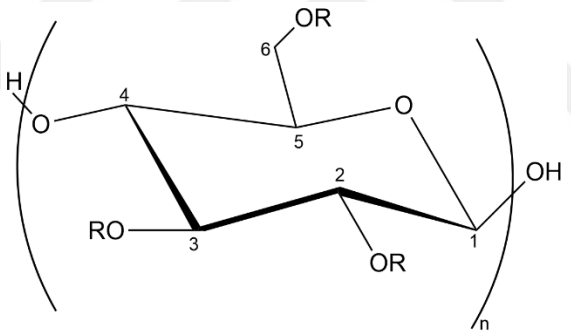

Figure 2.5. Chemical structure of cellulose ether. Adapted from the reference [81].

Table 2.1. Alkyl groups of cellulose ethers [82][83].

Cellulose Ether	Alkyl Group
Methyl cellulose	-H or -CH_3
Carboxymethyl cellulose	-H or -CH_2COOH
Ethyl cellulose	-H or -CH_2CH_3
Hydroxyethyl cellulose	-H or -CH_2CH_2OH
Hydroxypropyl cellulose	-H or -$CH_2CH_2CH_2OH$
Hydroxypropyl methylcellulose	-H or -CH_3 or - $CH_2CH_2CH_2OH$

Among these cellulose ethers, sodium carboxymethyl cellulose (Figure 2.6) is studied the most as a precursor material since it is highly soluble in water and forms clear,

viscous solutions due to its ionic nature. It is also stable in acidic and alkaline environments [82][81]. The molecular weight, the degree of substitution (DS), and the distribution of carboxymethyl substituents along the polymer chains impact the properties of CMC [84].

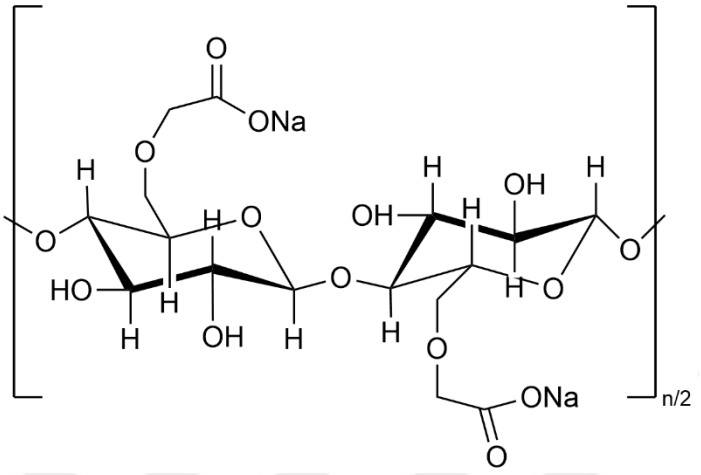

Figure 2.6. Chemical structure of sodium carboxymethyl cellulose. Adapted from the reference [84]

2.7 Crosslinkers and cellulose ether hydrogels

First of all, a gel should be obtained to produce aerogel. Hydrogels are three-dimensional polymeric networks, and they can be prepared by physical or chemical gelation methods. Physical gelation is triggered by heating, pH adjusting, or changing the ionic strength. Physical gels are bonded by non-covalent interactions such as van der Waals forces, hydrogen bonding, or electrostatic interactions, and they are generally reversible. On the other hand, chemical gelation is described as the formation of covalent bonds between polymer chains by cross-linking reactions and is an irreversible process. The gels produced by chemical gelation generally have high mechanical strength and stability. Furthermore, chemical gelation enables tuning of the pore properties of hydrogels, therefore aerogels, by changing the chemical compositions of the reactants and the reaction conditions. In addition, scaling up a chemical gelation process is easier [85][86].

Citric acid (CA), a non-toxic weak organic tricarboxylic acid, is an effective crosslinker in polymer chemistry applications. Citric acid ($C_6H_8O_7$), abundant in citrus fruits, is used in food, pharmaceutical, and chemical applications [87]. Its biocompatibility makes it suitable for biopolymer formulations such as edible films for food packaging. As it is shown in Figure 2.7, citric acid has one hydroxyl and three

carboxyl groups [88]. The carboxyl groups of citric acid react with hydroxyl groups in polymers to form ester linkages, creating stable three-dimensional networks that enhance mechanical properties and structural integrity [88].

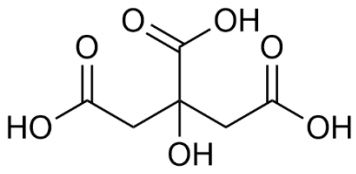

Figure 2.7. Chemical structure of citric acid. Adapted from the reference [87]

Oxalic acid (OA) is a non-toxic, weak organic dicarboxylic acid. It naturally occurs in plants and is commonly used for cleaning applications. The chemical structure of oxalic acid ($C_2H_2O_4$) is given in Figure 2.8. In an aqueous solution, oxalic acid dissociates in oxalate ions and protons, leading to an increase in polymer dissolution and ionic crosslinking in hydrogels [89]. Therefore, oxalic acid is used as a physical crosslinking agent in synthesizing hydrogels and polymer networks [90][91].

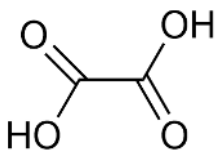

Figure 2.8. Chemical structure of oxalic acid. Adapted from the reference [90]

Maleic anhydride ($C_4H_2O_3$) is a cyclic dicarboxylic anhydride (Figure 2.9) commonly used as a crosslinker in polymer chemistry. When maleic anhydride reacts with polymers containing functional groups such as hydroxyl or amine, it undergoes a ring-opening reaction to form covalent bonds, crosslinking between polymer chains [92]. This process enhances the polymer network's mechanical strength, thermal stability, and chemical resistance. Its versatility, biocompatibility with various polymers, and low cytotoxicity make it a valuable crosslinking agent in polymer synthesis and material science [93].

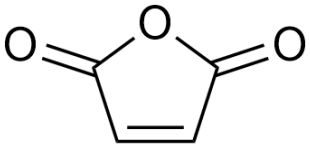

Figure 2.9. Chemical structure of maleic anhydride. Adapted from the reference [94]

Various CMC-based hydrogels/cryogels/aerogels were prepared and investigated in the literature. The studies either involved mixing CMC with other polymers like HEC

[95], chitosan [96], starch [88], and PVA [97][98] or employed toxic crosslinkers such as divinylsulphone [99], glutaraldehyde [88], and epichlorohydrin [100]. Alternatively, some studies utilized direct freeze-drying methods. Demitri et al. prepared CMC hydrogels by crosslinking with citric acid. They also added HEC to the precursor solution to improve intermolecular crosslinking. During the hydrogel synthesis, they dried the hydrogel at 30°C and then crosslinked it at 80°C, which unfortunately led to the collapse of the 3D porous structure [101]. Seki et al. also synthesized CMC-HEC-based hydrogels and investigated fumaric and malic acids as crosslinkers. They prepared CMC-HEC films by removing the water inside the pores of CMC hydrogels, achieved by drying the gels at 80°C for 16 hours [102]. Wang et al. fabricated CMC-based magnetic aerogels by using citric acid as a crosslinker. After preparing the solution, they crosslinked it at 80°C to form a hydrogel, which was then directly freeze-dried. Prepared aerogels showed high porosities (>94) [103]. Baldino et al. prepared CMC-HEC-based aerogels using 0.04 M divinyl sulfone as a crosslinker and potassium hydroxide as a catalyst. However, they did not investigate the effect of CMC characteristics on aerogel pore properties [99]. Recently, Yu and Budtova prepared CMC aerogels using non-solvent induced phase separation followed by supercritical drying with CO_2, which was the first time in the literature. They examined the influence of molecular weight, degree of substitution, and initial concentration of CMC on the properties of the aerogels. They had bulk densities below 0.25 g/cm^3 and specific surface areas between 25 and 143 m^2/g [104].

2.8 Freeze-Thaw Induced Gelation

Freeze-thaw induced gelation is a physical method (Figure 2.10) utilized in various fields such as food science, pharmaceuticals, and materials engineering to create gels with tailored properties. This method involves subjecting a solution to cycles of freezing and thawing, leading to the formation of a gel network.

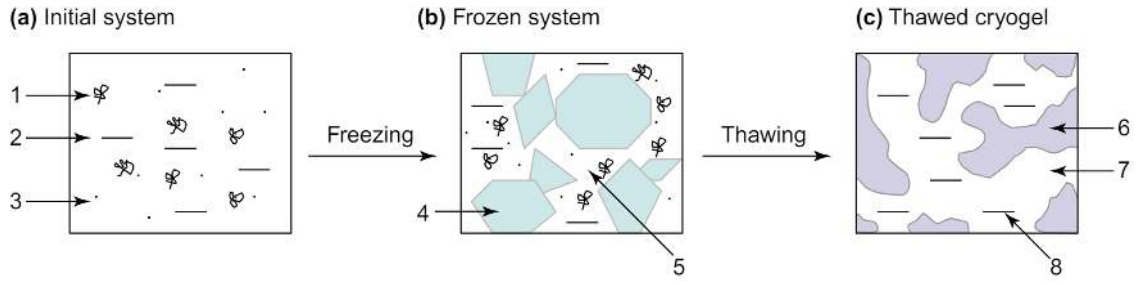

Figure 2.10. 1, macromolecules in a solution; 2, solvent; 3, low-molecular solutes; 4, polycrystals of frozen solvent; 5, unfrozen liquid microphase; 6, polymeric framework of a cryogel; 7, macropores; 8, solvent [105].

During the freezing and frozen storage stages, the solvent is crystallized, resulting in a reduction in the space between polymer chains; therefore, the polymer gets concentrated, and chains interact with each other. After thawing, junction zones of the three-dimensional network are formed due to these chain interactions. Then, freeze-thaw cycles are repeated to obtain a more stable hydrogel [106][107][108]

Several parameters can affect the freeze-thaw induced gelation. One significant parameter is the freezing rate, which influences the size and distribution of ice crystals formed during the process. A faster freezing rate leads to smaller pore sizes. On the other hand, a slower freezing rate typically leads to larger ice crystals and a more concentrated liquid phase, potentially resulting in a denser gel network upon thawing. As the porous structure is more ordered, hydrogels have better physical properties [109]. The number of freeze-thaw cycles and the duration of each cycle also affect gel properties, with multiple cycles typically resulting in denser gels due to repeated concentration and aggregation [91][110]. Additionally, the composition and concentration of polymer in the initial solution or dispersion significantly impact gelation behavior, with higher concentrations often promoting more robust gel networks [110]. Therefore, tuning the pore structure by adjusting the gelation conditions, such as frozen storage time and the number of freeze-thaw cycles, is possible [111]. Additionally, freeze-thaw-induced gelation is relatively simple and may be economical since high temperatures and toxic chemicals are not required.

2.9 Heat Transfer Mechanisms in Aerogels

Heat transfer in a porous media is classified into three mechanisms: conduction, convection, and radiation. Figure 2.11 shows a schematic representation of the heat transfer mechanisms in a porous media.

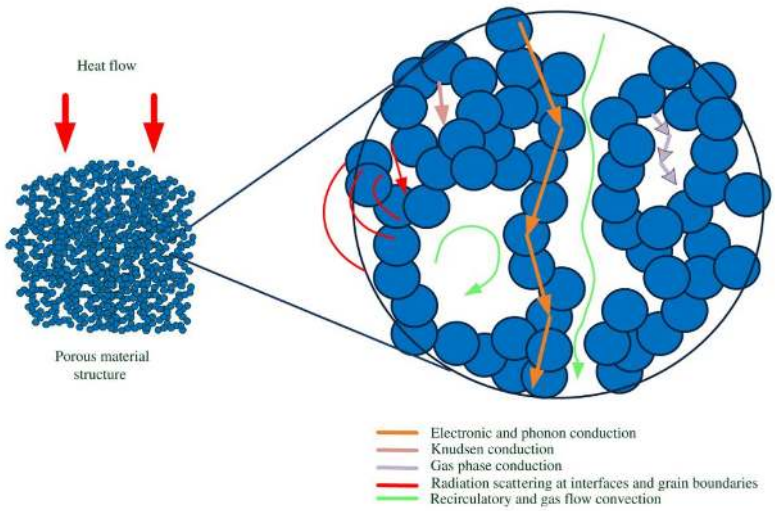

Figure 2.11. Heat transfer mechanisms in a porous media [112].

Conduction heat transfer can occur through the solid and the gas due to the motions and collisions of phonons and gas molecules, respectively. The gas convection in aerogels is negligible since the mean aerogel pore diameters are nanoscale. Radiative heat transfer is affected by photon scattering.

According to the three heat transfer modes in aerogel, there are three thermal conductivity types: solid, gaseous, and radiative thermal conductivity. The overall thermal conductivity is called effective thermal conductivity [70].

2.10 Solid Thermal Conductivity

Solid thermal conductivity depends on the phonon transport. Phonons are quantized lattice vibrations that are the source of many physical properties of the crystals, such as heat transfer and heat capacity [113]. Although aerogels are usually amorphous materials, localized vibrations are used to determine the solid thermal conductivity [70].

The general equation of solid thermal conductivity based on the kinetic theory is given in Equation 2.4:

$$\lambda_s = \frac{1}{3} c_v \rho v_{ph} \Lambda_{ph} \tag{2.4}$$

where c_v is specific heat at constant volume, ρ is the density of the solid backbone, v_{ph} is the phonon velocity and Λ_{ph} is the mean free path of a phonon between two consecutive collisions [114] [113]. The specific heat is a function of temperature, and it is calculated by Debye theory (Equation 2.5):

$$\bar{c_v}(T) = 9Nk_B\left(\frac{T}{\Theta_D}\right)^3 \int_0^{x_D} \frac{x^4 e^x}{(e^x-1)^2}\,dx \tag{2.5}$$

where N is the number of atoms, k_B is the Stefan– Boltzmann constant, $x_D = \Theta_D/T$ and Θ_D is the Debye temperature. The specific heat is almost constant at temperatures that are close to the Debye temperature or higher than the Debye temperature [115].

The mean free path of phonons is the product of phonon velocity v_{ph} and average relaxation time τ_{ph} [70]. The mean free path of phonons depends on scattering mechanisms: Umklapp phonon-phonon scattering, phonon-defect scattering, phonon-electron scattering, and phonon-boundary scattering [115]. The average relaxation time of phonons can be calculated by Matthiessen's rule, which is given in Equation 2.6 [70]:

$$\frac{1}{\tau_{ph}} = \frac{1}{\tau_U} + \frac{1}{\tau_M} + \frac{1}{\tau_S} + \cdots \tag{2.6}$$

Thus, the mean free path of phonons can be calculated by Equation 2.7 [70]:

$$\frac{1}{\Lambda_{ph}} = \frac{1}{\Lambda_U} + \frac{1}{\Lambda_M} + \frac{1}{\Lambda_S} + \cdots \tag{2.7}$$

The scattering mechanisms are categorized into three groups: volumetric scattering Λ_V (scattering due to the phonons, defects, impurities, and grain boundaries), boundary scattering Λ_S and interfacial scattering Λ_T, which can be expressed by Equation 2.8 [70].

$$\frac{1}{\Lambda_{ph}} = \frac{1}{\Lambda_V} + \frac{1}{\Lambda_S} + \frac{1}{\Lambda_T} \tag{2.8}$$

Λ_V is calculated as (Equation 2.9),

$$\Lambda_V = \Lambda_{bulk} = \frac{3\lambda_{bulk}}{c_v \rho v_{ph}} \tag{2.9}$$

where λ_{bulk} is the thermal conductivity of the bulk material and Λ_{bulk} is the mean free path of the bulk material. Also, v_{ph} is the mean sound velocity of the solid backbone [70].

Λ_T is calculated as (Equation 2.10),

$$\Lambda_T = 3LT_D \tag{2.10}$$

where T_D is the energy transmissivity from one particle to another. If the particles are the same material, the T_D will be 0.5. In addition, L is the segment length of the solid phase

and calculated by Equation 2.11:

$$L = \sqrt{{d_p}^2 - a^2} \tag{2.11}$$

where d_p is the particle diameter and a is the contact diameter of the two adjacent particles [70].

Liu classified the heat flux into two types, which are longitudinal (perpendicular) heat flux and transverse (parallel) heat flux (Figure 2.12).

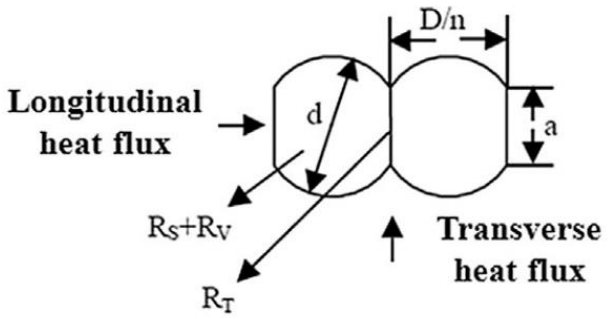

Figure 2.12. Solid unit structure model of silica aerogel [70].

According to that, Λ_s is calculated as (Equation 2.12 & 2.13),

$$\Lambda_s = \frac{1+p}{1-p} a \tag{2.12}$$

$$\Lambda_s = \frac{1+p}{1-p} d_p \tag{2.13}$$

where p is the boundary specularity. If it is assumed that the boundary is completely diffused, p will be equal to zero [70].

Consequently, the longitudinal $\lambda_{eff,L}$ and transverse $\lambda_{eff,T}$ solid thermal conductivity can be calculated by Equation 2.14 & 2.15 [70]:

$$\lambda_{eff,L} = \frac{\lambda_b}{1 + \frac{\Lambda_{bulk}}{a} + \frac{\Lambda_{bulk}}{3LT_D}} \tag{2.14}$$

and

$$\lambda_{eff,T} = \frac{\lambda_b}{1 + \frac{\Lambda_{bulk}}{d_p}} \tag{2.15}$$

Bi et al. declared that the above model is not convenient for aerogels since aerogel

backbones have interconnected structures and particle sizes are larger than contact diameters, resulting in interfacial resistance as heat is transferred through the interconnected particles. They also stated that Λ_s depends on both the contact diameter and particle diameters. Therefore, Bi et al. developed a new model for Λ_s including the size effect and the interfacial resistance of the interconnected particles, which is shown in Equation 2.16 [116]:

$$\Lambda_s = \frac{1}{a}\frac{2A_{inter}}{A_{eff}} + \frac{1}{d_p}\frac{A_{sphere}}{A_{eff}} \tag{2.16}$$

where A_{inter} and A_{sphere} are the areas of the interface and spherical cap, respectively. A_{eff} is the effective atomic scattering area of a single particle (Equation 2.17):

$$A_{eff} = 2A_{inter} + A_{sphere} \tag{2.17}$$

Based on the cylindrical superlattice nanowire models derived by Dames et al. (Equation 2.18) [117]

$$\Lambda_T = 3LT_D/2 \tag{2.18}$$

and Chen et al. (Equation 2.19) [118]

$$T_D = \frac{C_{V,B}v_B}{C_{V,B}v_B + C_{V,A}v_A} \tag{2.19}$$

(where A and B indicates the two adjacent segments of the superlattice nanowire) Bi et al. developed a new model for interfacial scattering Λ_T. They declared that the contact diameter of the interconnected particles a is always smaller than the particle diameter d_p and the energy transmission area is $\pi a^2/4$ instead of $\pi d_p^2/4$. Therefore, Equation 2.19 is modified as Equation 2.20 [116],

$$T_D = \frac{C_{V,B}v_B}{C_{V,B}v_B + C_{V,A}v_A}\frac{a^2}{d_p^2} \tag{2.20}$$

where A and B indicates the two adjacent particles of aerogel backbone.

Several factors affect the solid thermal conductivity of aerogels. Heat conduction paths in aerogels are longer than those of bulk materials due to their complex nano-porous structures. Besides, the characteristic lengths of aerogels are equal to or less than the phonon mean free path. Therefore, these size effects suppress the solid thermal conductivity in aerogels [71] [70].

Density also has a significant effect on solid thermal conductivity. As the density increases, solid thermal conductivity increases. However, density affects all three types of thermal conductivity; therefore, to obtain the lowest thermal conductivity, an optimum density should be found [119].

Increasing porosity is also another important method to suppress solid conductivity. Since it decreases the density and restricts the motions of phonons in the solid structure [60].

2.11 Gaseous Thermal Conductivity

Gaseous heat transfer in porous materials is reduced compared to heat transfer in free gas due to the restricted collisions of the gas molecules in the porous structure [120].

The first gaseous thermal conductivity model was based on the kinetic theory, and it was developed by Kistler in 1935 (Equation 2.21) [121]:

$$\lambda_g = BC_{V,g}\eta_g \tag{2.21}$$

where B is a constant, $C_{V,g}$ is the specific heat at constant volume, and η_g is the viscosity which can be calculated by Equation 2.22 [121]:

$$\eta_g = 0.35\rho_g v_g l_g \tag{2.22}$$

where ρ_g is the density, v_g is the arithmetical average velocity of the molecules, and l_g is the mean free path of the gas molecules. From the above equations, the gaseous thermal conductivity was finally derived as Equation 2.23[121]:

$$\lambda_g = 0.058\alpha\sqrt{\frac{m_g}{T}}C_{V,g}l_0\frac{D^2}{\frac{2Ll_0(1-\alpha)}{p}+\alpha L\left(L+\frac{l_0}{p}\right)} \tag{2.23}$$

where m_g is the molecular weight, T is the temperature, p is the pressure, D is the average pore diameter, L mean free path of a highly attenuated gas within the aerogel and l_0 is the normal mean free path of the gas molecules. In this equation, α is the accommodation coefficient which is the fraction of the gas molecules comes to thermal equilibrium when they collide to the surface, accordingly, 1- α is specularly reflected fraction [121].

In 1969, Kaganer derived Knudsen formula (Equation 2.24) which describes the gaseous thermal conductivity of free gas between two parallel plates [70]:

$$\lambda_g = \frac{\lambda_g^0}{1 + 2\beta K_n} \tag{2.24}$$

where $\lambda_g{}^0$ is the thermal conductivity of the gas in free space. β is a coefficient that is calculated as in Equation 2.25 [70]:

$$\beta = \frac{2\gamma}{\gamma + 1}\frac{2 - \alpha}{\alpha}\frac{1}{P_r} \tag{2.25}$$

where α is the accommodation coefficient, γ is the adiabatic coefficient of the gas and P_r is the Prandtl number. β is 1.4, 1.8, 1.6, 10.2 and almost 2 for CO_2, Ar, N_2, He and air, respectively [122][123].

In Equation 2.24, K_n is the Knudsen number, which is the ratio of the mean free path of the gas molecules l_g and the mean pore diameter D as given in Equation 2.26 [124]:

$$K_n = l_g / D \tag{2.26}$$

The mean free path of the gas molecules can be calculated from Equation 2.27 [124]:

$$l_g = \frac{k_B T}{\sqrt{2}\pi d_g^2 p} \tag{2.27}$$

where k_B is the Boltzmann's constant, T is gas temperature, d_g is the diameter of a gas molecule and p is the gas pressure inside porous material [124].

If the mean pore diameter is smaller than the mean free path of the gas molecules, K_n will be greater than 1, which means there is molecular heat transfer. In this case, gas molecules mostly collide with the solid backbone; therefore, the contribution of the thermal conductivity is proportional to the number of gas molecules. On the contrary, if the mean pore diameter is greater than the mean free path of the gas molecules, K_n will be less than 1, which means there is diffusive heat transfer. In this case, gas molecules mostly collide with each other, and the gaseous thermal conductivity is equal to the thermal conductivity of free gas, which does not depend on gas pressure at ambient and moderate pressures.

After Kaganer's formula, several models are proposed to obtain thermal conductivity more accurately. Kaganer used the mean free path of the free space instead of the mean free path of the gas in a porous material, leading to large computational

deviations. Consequently, in 1995, Zeng et al. derived the mean free path of gas molecules in silica aerogel and proposed a new analytical model based on gas kinetics (Equation 2.28) [120] [125]:

$$\lambda_g = \frac{(2.25\gamma - 1.25)0.461\left(\frac{p}{k_B T}\right)\left(\frac{8k_B T}{m_g \pi}\right)^{0.5}}{\frac{0.25S\rho}{\phi} + \sqrt{2}\left(\frac{p}{k_B T}\right)\pi {d_g}^2}\frac{C_v}{N_A} \tag{2.28}$$

where γ is the adiabatic coefficient of the gas, m_g is the molecular weight, N_A is Avogadro constant, C_v is the specific heat at constant volume, ρ is the density of aerogel, ϕ is the aerogel porosity, and S is the specific surface area of aerogel.

There were still some significant errors due to aerogels' non-uniform pore size distribution. Thus, Reichenauer et al. proposed a new model (Equation 2.29) assuming that there are two different mean pore diameters (D_1 and D_2) and two different corresponding porosity ($\phi_1$and ϕ_2) and the sum of porosities is unity [71]:

$$\lambda_g = \frac{{\lambda_g}^0 \phi_1}{1 + \frac{2\beta\Lambda_g}{D_1}} + \frac{{\lambda_g}^0 \phi_2}{1 + \frac{2\beta\Lambda_g}{D_2}} \tag{2.29}$$

After that, Reichenauer et al. modified the model by assuming that there is a Gaussian distribution function for the pore size distribution, and it is shown in Equation 2.30:

$$\lambda_g = \frac{1}{N}\int \frac{{\lambda_g}^0}{1 + \frac{2\beta\Lambda_g}{D'}} e^{-\frac{(D'-D)^2}{2\sigma^2}} dD' \quad (D' > 0) \tag{2.30}$$

where D is the mean pore size, D' is the convolution variable, σ is the standard deviation of the Gauss distribution function (the distribution width of the pore size), and N is a factor that normalizes the integration to provide the correct total porosity. Although Equation 2.30 is easy to apply, it is not convenient since N must be calculated separately after the integration [124].

In order to make an easier and more convenient computation, Bi et al. developed an approximate equation in which all the pores act as parallel paths (Equation 2.31) [124]:

$$\lambda_g = \sum_{i=1}^{n} \phi_i K(D_i) \tag{2.31}$$

where n is the number of pores, i is the pore index, ϕ_i is the contribution to the total porosity and $K(D_i)$ is a simplified form of Equation 2.24 ϕ_i was calculated as as in Equation 2.32:

$$\phi_i = \int_{D_i}^{D_i+\Delta D} \frac{1}{\sqrt{2\pi}\sigma} e^{-\frac{(D'-D)^2}{2\sigma^2}} dD' \approx \frac{\Delta D}{\sqrt{2\pi}\sigma} e^{-\frac{(D_i-D)^2}{2\sigma^2}} \quad (D_i > 0) \tag{2.32}$$

Thus, if n is large enough, the total gaseous thermal conductivity can be written as in Equation 2.33:

$$\lambda_g \approx \sum_{i=1}^{n} \left[\frac{\Delta D}{\sqrt{2\pi}\sigma} e^{-\frac{(D_i-D)^2}{2\sigma^2}} \right] K(D_i) \quad (D_i > 0) \tag{2.33}$$

Bi et al. also derived the total proportion of the pore size distribution when it is in the confidence interval $[D - 3\sigma, D + 3\sigma]$ as in Equation 2.34:

$$\lim_{n\to\infty} \sum_{i=1}^{n} \phi_i = \int_{D-3\sigma}^{D+3\sigma} \frac{1}{\sqrt{2\pi}\sigma} e^{-\frac{(D'-D)^2}{2\sigma^2}} dD' \approx 0.9974 \quad (D - 3\sigma > 0) \tag{2.34}$$

However, the pore size distributions in aerogels are generally non-uniform. In addition, the contributions of the large pores to the gaseous thermal conductivity are greater than those of the small pores. Based on these considerations, Bi et al. developed an improved model using a double times probability of $[D + \sigma, D + 3\sigma]$ and the random and non-uniform pore size distribution function which is given in Equation 2.35 [124]:

$$\phi_i = \begin{cases} \frac{\Delta D}{\sqrt{2\pi}\sigma} e^{-\frac{(D_i-D)^2}{2\sigma^2}}, & D_i \in [D - \sigma, D + \sigma]\ D_i - \sigma > 0 \\ \frac{2\Delta D}{\sqrt{2\pi}\sigma} e^{-\frac{(D_i-D)^2}{2\sigma^2}}, & D_i \in [D + \sigma, D + 3\sigma] \end{cases} \tag{2.35}$$

There are various methods to suppress gaseous heat transfer. Small pore diameters increase the Knudsen effect, and therefore, the gaseous thermal conductivity decreases. Preparing an aerogel with a more uniform pore size distribution can decrease the gaseous thermal conductivity [71]. Decreasing porosity reduces the gaseous thermal conductivity and increases the solid-gas coupling effect [112][126]. Therefore, optimum density and porosity should be found. In addition, a vacuum can be applied to aerogels to reduce gaseous thermal conductivity. For this purpose, evacuation to 10 mbar is sufficient [119].

2.12 Radiative Thermal Conductivity

The radiative heat transfer occurs from electromagnetic radiation emissions from

a material surface. Aerogels are participating materials, which means that aerogels absorb, emit, and scatter electromagnetic radiation. In participating materials, radiation exchange occurs between the volume and surface elements and between the surface elements [127].

Radiative transfer equation (RTE) for aerogels is derived as in Equation 2.36:

$$\frac{dI_\lambda(s,\boldsymbol{s})}{ds} = -(\sigma_{a\lambda}+\sigma_{s\lambda})I_\lambda(s,\boldsymbol{s}) + \sigma_{a\lambda}I_{b\lambda}(s) + \frac{\sigma_{s\lambda}}{4\pi}\int_{4\pi} I_\lambda(s,\boldsymbol{s_i})\phi_\lambda(\boldsymbol{s_i},s)d\Omega\Omega_i \quad (2.36)$$

where $I_\lambda(s,\boldsymbol{s})$ is the spectral radiation intensity, s is the spatial location, $\boldsymbol{s}$ is the direction radiation intensity and λ is the wavelength. $\sigma_{a\lambda}$ and $\sigma_{s\lambda}$ indicate the spectral absorption and scattering coefficient, respectively and the summation of $\sigma_{a\lambda}$ and $\sigma_{s\lambda}$ is the spectral extinction coefficient $\sigma_{e\lambda}$. Moreover, $\phi_\lambda(\boldsymbol{s_i},s)$ is the phase function [127].

RTE is an integro-diffential and nonlinear equation. In order to solve RTE, some approximations should be applied. These approximations are categorized into two groups: neglecting physical processes owing to the intrinsic characteristics of the material and making mathematical approximations [70]. Most of the organic aerogels and carbon aerogels are optically thick materials.

2.12.1 Optically thick approximation

In optically thick mediums, photons can travel a short distance before they are absorbed or scattered. Radiative heat transfer is diffusive in optically thick aerogels, and radiative thermal conductivity can be derived from the Stefan-Boltzmann equation for photons as given in Equation 2.37 [71]:

$$\lambda_r = \frac{16}{3}\frac{n^2 k_B}{\rho E_s(T)}T^3 \quad (2.37)$$

where n is the refractive index, k_B is the Stefan-Boltzmann constant, T is the temperature, ρ is the density, and E_s is the temperature dependent Rosseland mean extinction coefficient, which is calculated from the Equation 2.38 [71]:

$$\frac{1}{E_s(T)} = \int_0^\infty \frac{1}{E_s(l)}\frac{\partial I_b(l)}{\partial I_b}dl \quad (2.38)$$

with

$$\frac{\partial I_b(l)}{\partial I_b} = \frac{15}{4\pi^4 z^6}\frac{\exp(1/z)}{[\exp(1/z)-1]^2} \quad (2.39)$$

and

$$z = \frac{k_B T}{hc} l \tag{2.40}$$

where $E_s(l)$ is the spectral extinction coefficient, l is the radiation wavelength of photons, $I_b(l)$ is the spectral blackbody flux, I_b is the black-body flux, k_B is the Boltzmann constant, h is the Planck's constant, and c is the speed of light [71].

Two assumptions are made to calculate Rosseland mean extinction coefficient. One of the assumptions is that the radiative heat transfer is far enough from the boundaries, and the other is that the temperature change with respect to the optical thickness is small [114].

The spectral extinction coefficient describes the attenuation of electromagnetic waves by absorption or scattering processes, and it depends on the chemical composition and structure of the materials. Tang et al. stated that the spectral extinction coefficient cannot be obtained directly; however, it can be obtained by experimental measurements or numerical simulations [71][128].

At high temperatures, the radiative thermal conductivity increases and becomes dominant. This increase is greater in transparent and translucent aerogels. In order to suppress the radiative heat transfer, some opacifiers such as SiC, carbon black, carbon fibers, TiO_2, and ZrO_2 can be added to aerogels. Due to their highly porous structure, aerogels are usually fragile. Therefore, opacifiers, which are added to reduce radiative thermal conductivity, will also improve the mechanical properties of aerogels. However, these doping materials can also increase the solid thermal conductivity of aerogel [70][71][114].

CHAPTER 3 EXPERIMENTAL METHODS AND CHARACTERIZATION TECHNIQUES

3.1 Materials

Benecel™ HPMC K100 LV PH PRM (164,000 Da), Benecel™ MC A15 LV PH PRM (~15,000 Da), Aqualon™ EC N22 Pharm (140,000 Da), Natrosol™ 250 HEC L Pharm (90,000 Da), and four types of CMCs with a trade name of Aqualon™ were kindly provided by Ashland Specialty Ingredients: 7LP PH (90,500 Da and DS 0.7), 7MF PH (250,000 Da and DS 0.7), 7 M31F PH (395,000 Da and DS 0.7) and 7HF PH (725,000 Da and DS 0.7). Polyvinyl alcohol (PVA) was also kindly provided by Ashland Specialty Ingredients. Citric acid monohydrate (purity 99.0%) and oxalic acid dihydrate (purity 99.0%) were purchased from Sigma Aldrich. Maleic anhydride (purity 99.0%) was purchased from Fluka. Ethanol with 99.9% purity and sulfuric acid were purchased from Isolab. Carbon dioxide (purity 99.9%) and nitrogen (purity 99.9%) were purchased from Air Liquide. All materials were used without further purification.

3.2 Thermogelation of cellulose ethers

The schematic illustration of the experimental procedure used to determine the gelation temperatures of cellulose ethers is given in Figure 3.1. Initially, an aqueous solution of 6 wt% cellulose ether (MC, HPMC, CMC) was prepared. The solution was put in a closed test tube, placed in a water bath, and then heated gradually on a hot plate while continuously stirring to ensure uniform heating. The temperature was monitored using a thermometer, and changes in gel formation were observed. The temperature at which gel formation began was noted as the thermogelation temperature of cellulose ethers. The experiment also included observing if the gel reverted to a solution state upon cooling, confirming the reversible nature of gelation.

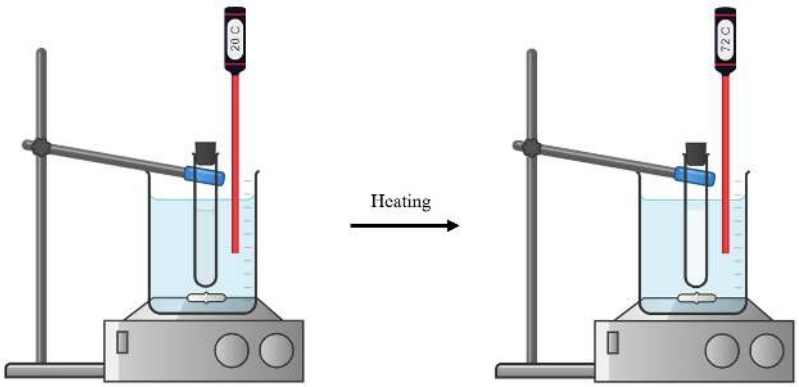

Figure 3.1. The schematic illustration of the experimental procedure used to determine the gelation temperatures of cellulose ethers.

3.3 Freeze-thaw induced gelation of cellulose ethers

An aqueous solution of CE was prepared by adding X g of CE to (90-X) g water, where X was 4, 6, and 8 g. The prepared solution was mixed with a stirring rate of 600 rpm at room temperature until a clear solution was obtained (Figure 3.2). At the same time, different amounts of crosslinker were dissolved in 10 g water. Then, the crosslinker solution was added to the CE solution. Solutions without crosslinkers were also prepared to see the effect of crosslinker, where X g of CE to (100-X) g water, X was varied as 4, 6, and 8 g. Freeze-thaw induced gelation was conducted by subjecting the cellulose ether solution to freezing at -19°C, frozen storage for 24 hours, and thawing at RT cycles.

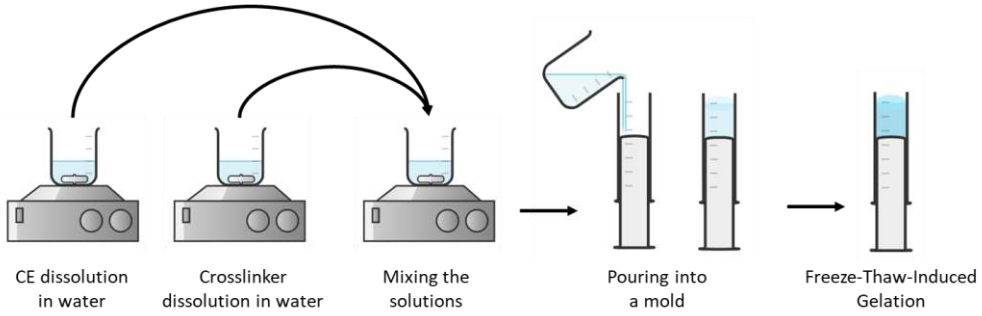

Figure 3.2. Schematic illustration of the CE hydrogel synthesis.

3.4 Synthesis of sodium carboxymethyl cellulose hydrogels

An aqueous solution of CMC was prepared by adding X g of CMC to (90-X) g water, where X was 4 and 6 g. The prepared solution was mixed with a stirring rate of 600 rpm at room temperature until a clear solution was obtained (Figure 3.3). At the same time, different amounts of crosslinker maleic anhydride were dissolved in 10 g water, as given in Table 3.1. Then, the maleic acid solution was added to the CMC solution. To see the effect of crosslinker, solutions without MA were also prepared, where X g of CMC

to (100-X) g water, X was varied as 4 and 6 g.

CMC gels and aerogels are named "CMC nameX_MAY_Nh," where X is the CMC concentration in the solution, Y is the MA concentration in the solution, and N is the frozen storage time (h).

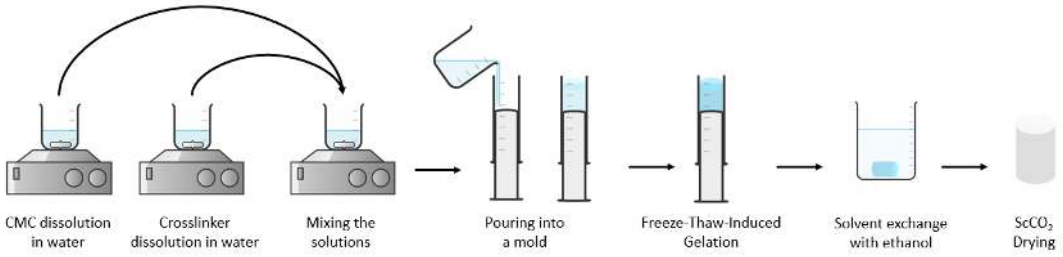

Figure 3.3. Schematic illustration of the CMC aerogel synthesis

Table 3.1. Formulations of prepared CMC aerogels.

CMC	Code	CMC Amount (g)	MA Amount (g)	DIW Amount (g)	Frozen Storage (h)
7LF PH	L6_MA1.2_8h	6	1.2	94	8
7LF PH	L6_MA1.8_8h	6	1.8	94	8
7LF PH	L6_MA2.4_8h	6	2.4	94	8
7LF PH	L6_MA1.2_24h	6	1.2	94	24
7LF PH	L6_MA1.8_24h	6	1.8	94	24
7LF PH	L6_MA2.4_24h	6	2.4	94	24
7 MF PH	M6_MA1.8_8h	6	1.8	94	8
7 M 31F PH	M31F6_MA1.8_8h	6	1.8	94	8
7 HF PH	H6_MA1.8_8h	6	1.8	94	8
7LF PH	L4_MA1.2_8h	4	1.2	96	8
7 MF PH	M4_MA1.2_8h	4	1.2	96	8
7 M 31F PH	M31F4_MA1.2_8h	4	1.2	96	8
7 HF PH	H4_MA1.2_8h	4	1.2	96	8

To see the effect of crosslinker, solutions without MA were prepared, with 6 g of CMC and 94 g of water.

The mixture was stirred overnight at RT. After that, 3 ml of the mixture was poured into 5 ml syringes used as cylindrical molds. For gelation, molds were placed in a freezer at -19°C. To investigate the effect of frozen storage time on gelation, molds were kept in the freezer for 8 and 24 hours (Table 3.1). The thawing of the frozen solutions was conducted at RT for 1 h. After several freeze-thaw cycles, CMC hydrogels were

obtained.

3.5 Optimization of solvent exchange conditions and supercritical drying of alcogels

Carboxymethyl cellulose exhibits polar characteristics [129]. This similarity in polarity between ethanol and CMC facilitates better solubility compared to acetone, which is less polar. Consequently, ethanol was selected for the solvent exchange. Preliminary tests showed that CMC hydrogels can swell and lose the polymer during the solvent exchange. Therefore, the solvent exchange procedure was determined to minimize the polymer loss. Three solvent exchange procedures were examined:

- Starting from 10% ethanol by volume, increasing by 10% EtOH every 2 hours
- Starting from 10% ethanol by volume, increasing by 10% EtOH every 24 hours
- Starting from 50% ethanol by volume, increasing by 10% EtOH every 12 hours

Since CMC is soluble in water/ethanol solutions, starting solvent exchange from lower concentrations of ethanol results in swelling; the initial concentration of solvent exchange was determined as 50% ethanol for further gels. The prepared hydrogels were subjected to a series of solvent exchange steps using solutions with increasing ethanol concentrations (50%, 60 %, 70%, 80%, 90%, and %100 ethanol by volume) every 12 h. CMC alcogels were dried by supercritical CO_2 in an Applied Separations Speed SFE unit at 50°C and 85 bars. To ensure the reproducibility of the findings, the experiments were conducted a minimum of three times at identical conditions.

3.6 CMC/PVA hybrid aerogels

In order to increase intermolecular crosslinking in CMC aerogels, CMC/PVA hybrid aerogels were fabricated. An aqueous solution of polymer (CMC and PVA with a weight ratio of 3/1) was prepared by adding X g of polymer to (90-X) g water, where X was 4 and 6 g. The prepared solution was mixed with a stirring rate of 600 rpm at room temperature until a clear solution was obtained. At the same time, maleic anhydride (40% w/w of polymer) was dissolved in 10 g water. The mixture was stirred overnight at RT. After that, 3 ml of the mixture was poured into 5 ml syringes used as cylindrical molds. For gelation, molds were placed in a freezer at -19°C for 24 hours. The prepared hydrogels were subjected to a series of solvent exchange steps using solutions with increasing ethanol concentrations (50%, 60 %, 70%, 80%, 90%, and %100 ethanol by volume) every 12 h. CMC alcogels were dried by supercritical CO_2 in an Applied Separations Speed SFE unit at 50°C and 85 bars. CMC/PVA gels and aerogels are named “CMC/PVAX”

where X is the total polymer concentration in the solution.

3.7 Sulfuric acid catalyzed CMC aerogels

Sulfuric acid (H_2SO_4) was used to increase the esterification reaction rate, improve the yield, and reduce the gelation time. An aqueous solution of 6 wt% CMC was prepared by adding 6 g of CMC to 84 g of water. The prepared solution was mixed with a stirring rate of 600 rpm at room temperature until a clear solution was obtained. At the same time, 2.4 g maleic anhydride was dissolved in 10 g water. While stirring these two mixtures, 0.175 M or 0.35 M sulfuric acid was added dropwise. The mixture was stirred overnight at RT. After that, 3 ml of the mixture was poured into 5 ml syringes used as cylindrical molds. For gelation, molds were placed in a freezer at -19°C for 24 hours. The prepared hydrogels were subjected to a series of solvent exchange steps using solutions with increasing ethanol concentrations (50%, 60 %, 70%, 80%, 90%, and %100 ethanol by volume) every 12 h. CMC alcogels were dried by supercritical CO_2 in an Applied Separations Speed SFE unit at 50°C and 85 bars. Sulfuric acid catalyzed CMC gels, and aerogels are named "CMC_XM" where X is the concentration of the sulfuric acid.

3.8 Characterization of Aerogels

Skeletal and bulk density, porosity, and pore volume and volume shrinkage

Skeletal density (ρ_{sk}) of prepared aerogel was measured with helium pycnometer, Micromeritics AccuPyc II 1340.

Bulk density (ρ_{bulk}) was calculated by the ratio of aerogel mass to volume. Aerogel mass was measured with digital analytical balance with a precision of 0.1 mg and the volume of aerogels was measured with the volume displacement of silica beads.

Porosity and total pore volume (V_p) were calculated by following equations:

$$Porosity\ (\%) = \left(1 - \frac{\rho_{bulk}}{\rho_{sk}}\right) \times 100\%$$

$$V_p(cm^3/g) = \frac{1}{\rho_{bulk}} - \frac{1}{\rho_{sk}}$$

The volumetric shrinkage of the gels was determined as follows:

$$Volume\ shrinkage\ (\%) = \frac{V_i - V_f}{V_i} \times 100\%$$

where V_i is the gel volume before solvent exchange and V_f is the aerogel volume.

The volumetric shrinkage and the density of the rest of the aerogels were determined by the average of a minimum of 5 samples.

Specific Surface Area BET & Pore size distribution

Specific surface area, micro and meso pore size, and pore volume of CMC aerogels were measured by nitrogen adsorption/desorption on Micromeritics ASAP 2020. Adsorption/desorption isotherms were obtained with a relative pressure (P/P_0) ranging from 10^{-7} to 0.995. Before the analysis, the samples were primarily degassed at 60°C under a vacuum for 30 h. Since the BJH approach is not applicable to biopolymer aerogels (due to the highly macroporous structure), the average pore size (D) is calculated with the following equation:

$$D = 4 \times \frac{V_p}{S_{BET}}$$

where V_p is the total pore volume and S_{BET} is the BET surface area [130].

Morphology by SEM

Morphology analyses of CMC aerogels were performed by ZEISS Ultra Plus scanning electron microscopy (SEM). Before SEM imaging, aerogels were sputtered with a 25 nm gold layer, and during SEM imaging, a charge compensator was used to avoid charging.

FTIR

FTIR (Thermo Scientific iS10 FT-IR, single reflection diamond ATR) was used to characterize the molecular structure of the precursors, hydrogels, and aerogels to validate the crosslinking reaction between them. FTIR spectra were obtained in the wavenumber range from 4000 to 650 cm^{-1}. A total of 64 transients were collected for each spectrum with a resolution of 4 cm^{-1}. The measurements were taken at room temperature.

Solid State NMR

Solid state 13C cross-polarization-magic angle spinning (13C CP-MAS) NMR spectra of CMC aerogel were recorded using Bruker 500 MHz Ascend NEO NMR Spectrometer equipped with Broad band solid state probe, with a spinning speed of 15 KHz. The number of scans, relaxation delay, and sweep width were fixed at 128 scans, 10 s, and 37 kHz, respectively.

Thermal conductivity measurement

Thermal conductivities of the prepared aerogels were measured with a TPS 1500 Hot Disk Thermal Constant Analyzer. Samples 13 mm in diameter and 5 mm in thickness were used for measurements.

CHAPTER 4 RESULTS AND DISCUSSION

4.1 Determination of gelation temperature of cellulose ethers

Among the five cellulose ethers, MC, CMC, and HPMC were studied since EC cannot be gelled with water [131] and HEC cannot form gels [132]. In the experiment conducted, gelation temperatures for MC, CMC, and HPMC were determined as 60, 65, and 72°C, respectively. The thermogelation of HPMC is given in Figure 4.1. However, it was observed that the gelation was reversible; after the HPMC gel was cooled down to RT, it returned to the solution form. The same thermogelation behavior was also obtained for MC and CMC. This behavior of cellulose ethers is attributed to their distinct molecular structure and their interactions with solvent molecules. In solution, cellulose ethers become fully hydrated, with minimal polymer-polymer interactions. At higher temperatures, polymer-polymer interactions are favored over polymer-solvent interactions, resulting in gel formation. Upon cooling, these interactions weaken, causing the gel to revert to the sol state [133][134].

Consequently, it was not possible to produce cellulose ether hydrogels with thermogelation. In addition, since preserving the 3D porous structure of the hydrogels is crucial, the freeze-thaw induced gelation method was used for further studies.

Figure 4.1. a) 6 wt% HPMC solution b) Heating HPMC solution c) Gelation of HPMC solution at 72 °C d) HPMC gel

4.2 Freeze-thaw induced gelation of cellulose ethers and effect of crosslinkers

Initially, cellulose ether solutions were prepared without crosslinker addition and then subjected to freezing and thawing cycles. However, CE hydrogels with 3D structures could not be obtained. Therefore, due to their eco-friendly properties, citric acid and oxalic acid were employed as crosslinkers. The prepared cellulose ether solutions, the crosslinker concentrations, and the formation of gels are given in Table 4.1. In the literature, the esterification of cellulose ethers with carboxylic acids is typically achieved by first evaporating the water and then crosslinking the hydroxyl groups of cellulose ethers at high temperatures [95]. The absence of gel formation may be because the carboxyl groups of citric acid and oxalic acid cannot attack the hydroxyl groups, which may be attributed to the water in the system and gelation at low temperatures.

Table 4.1. Summary of the prepared cellulose ether solutions with citric acid and oxalic acid and their gel formation.

CE	CE Aqueous Solution Concentration (%)	Crosslinker Type - Concentration (% w/w of polymer)	Gel Formation
MC	4	CA-10	No
		CA-20	No
		OA-10	No
		OA-20	No
MC	6	CA-10	No
		CA-20	No
		OA-10	No
		OA-20	No
MC	8	CA-10	No
		CA-20	No
		OA-10	No
		OA-20	No
HPMC	4	CA-10	No
		CA-20	No
		OA-10	No
		OA-20	No
HPMC	6	CA-10	No
		CA-20	No
		OA-10	No
		OA-20	No
HPMC	8	CA-10	No
		CA-20	No
		OA-10	No
		OA-20	No
CMC	4	CA-10	No

		CA-20	No
		OA-10	No
		OA-20	No
CMC	6	CA-10	No
		CA-20	No
		OA-10	No
		OA-20	No
CMC	8	CA-10	No
		CA-20	No
		OA-10	No
		OA-20	No
CMC/HEC	4	CA-10	No
		CA-20	No
		OA-10	No
		OA-20	No
CMC/PVA	4	CA-10	No
		CA-20	No
		OA-10	No
		OA-20	No
CMC/PVA	6	CA-10	No
		CA-20	No
		OA-10	No
		OA-20	No

Since maleic anhydride is a highly reactive compond [135], it was used as a crosslinker for cellulose ethers. The prepared formulations and formation of gels are given in Table 4.2; among those formulations, only CMC and CMC/PVA hybrid hydrogels are obtained (Figure 4.2).

Table 4.2. Summary of the prepared cellulose ether solutions with citric acid and oxalic acid and their gel formation.

CE	CE Aqueous Solution Concentration (%)	Crosslinker Type - Concentration (% w/w of polymer)	Gel Formation
MC	6	MA-10	No
		MA-20	No
		MA-30	No
HPMC	6	MA-10	No
		MA-20	No
		MA-30	No
CMC	6	MA-10	No
		MA-20	Yes
		MA-30	Yes
CMC/HEC	6	MA-10	No
		MA-20	No

		MA-30	No
CMC/PVA	6	MA-10	No
		MA-20	Yes
		MA-30	Yes

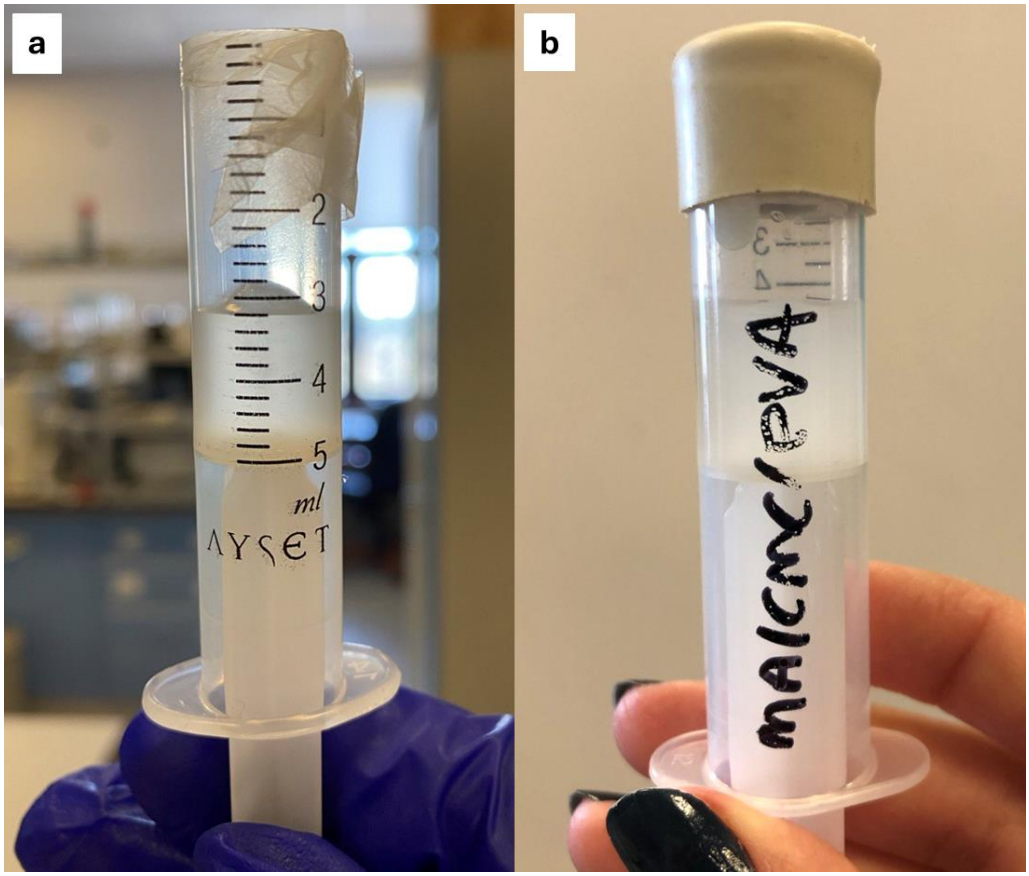

Figure 4.2. Prepared hydrogels a) CMC and b) CMC/PVA hybrid

4.3 Determination of freeze-thaw induced gelation conditions for CMC

Understanding the relationship between frozen storage time and the number of freeze-thaw cycles required to obtain a gel in prepared hydrogels is essential for optimizing their stability and properties. This relationship was investigated by subjecting 6 wt % CMC aqueous solutions with a crosslinker concentration equal to 30% of the weight of CMC to various storage times in the freezer.

As depicted in Figure 4.3, the results revealed a significant difference in the number of freeze-thaw cycles needed for different frozen storage times. For instance, there was a substantial reduction in the number of cycles required between 2, 4, and 6 hours of frozen storage. Interestingly, 6 and 8 hours of frozen storage exhibited similar trends. In contrast, a frozen storage time of 24 hours significantly decreased the number of freeze-thaw cycles needed. It is conceivable that prolonged freezing alters the physical

and chemical properties of the hydrogel matrix, thereby reducing the energy required for gel formation upon thawing.

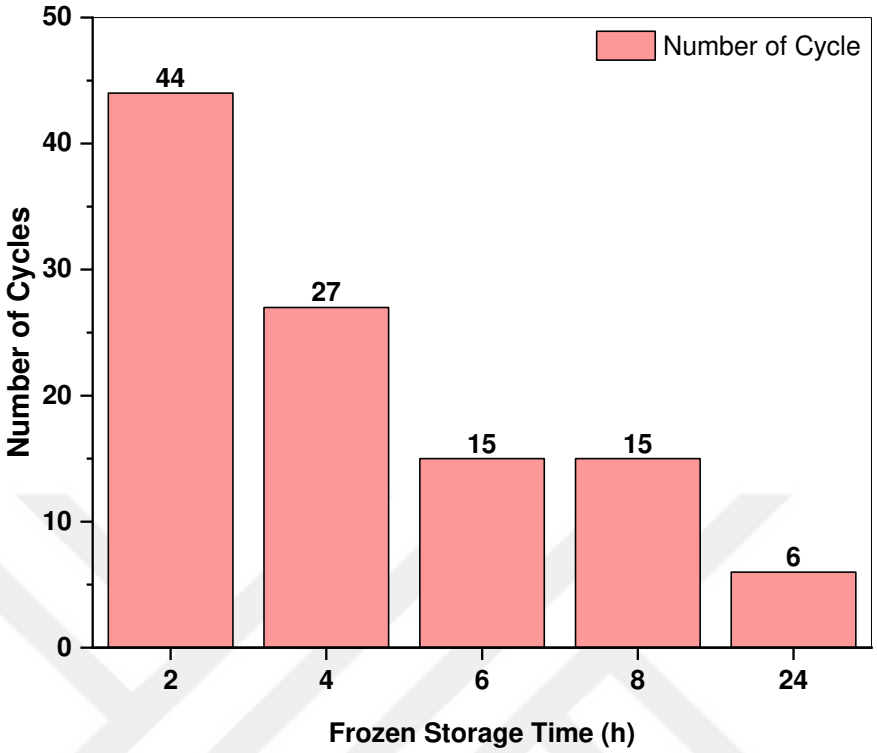

Figure 4.3. Effect of frozen storage time on the number of FT cycles

The effect of thawing temperature on gelation was also investigated. 6 wt % CMC aqueous solutions with a crosslinker concentration equal to 30% of the weight of CMC were prepared and subjected to different thawing temperatures, which are 4 °C, 50 °C, and RT. However, no significant effect was observed.

4.4 Effect of solvent exchange conditions

The effect of the solvent exchange conditions on aerogels was determined by the calculation of the mass loss of aerogels (Appendix A.1). This relationship was investigated by subjecting 6 wt % CMC aqueous solutions with a crosslinker concentration equal to 30% of the weight of CMC to various solvent exchange conditions.

According to the results (Figure 4.4), minimum mass loss was seen when the solvent exchange started from 50% EtOH and changed every 12 hours. The mass loss of the aerogel subjected to 24 hours of solvent exchange starting from 10% EtOH with a 10% increment is not given in Figure 4.4 since, during the solvent exchange, hydrogel dissolved in the solution.

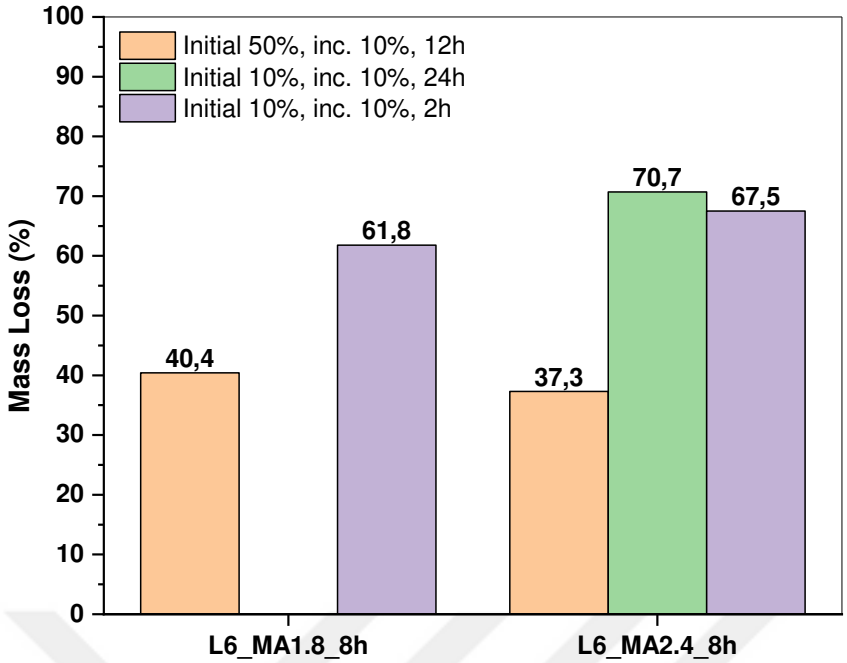

Figure 4.4. The change in the mass loss of CMC aerogels with the solvent exchange process.

4.5 Freeze-Thaw induced gelation of CMC solutions

CMC aerogels were prepared in 3 main steps: first, CMC hydrogels were formed, then solvent exchange with ethanol took place, and finally, alcogels were supercritically dried with CO_2.

4.5.1 Effect of frozen storage time and crosslinker concentration on gelation

Various gels have been prepared to investigate the effects of frozen storage time and crosslinker concentration on gelation. Frozen storage times of 8 hours and 24 hours were chosen. The concentration of the crosslinker was 20%, 30%, and 40% of the weight of carboxymethyl cellulose, respectively. The prepared aerogels using the formulations given in Table 3.1 are shown in Figure 4.5.

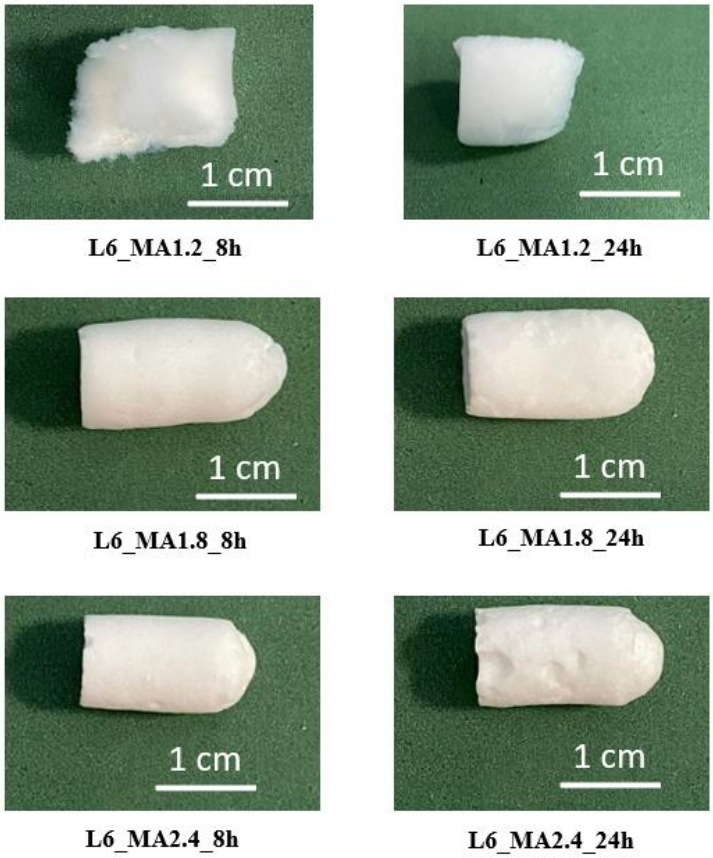

Figure 4.5. Photos of CMC aerogels from 6 wt % CMC solutions.

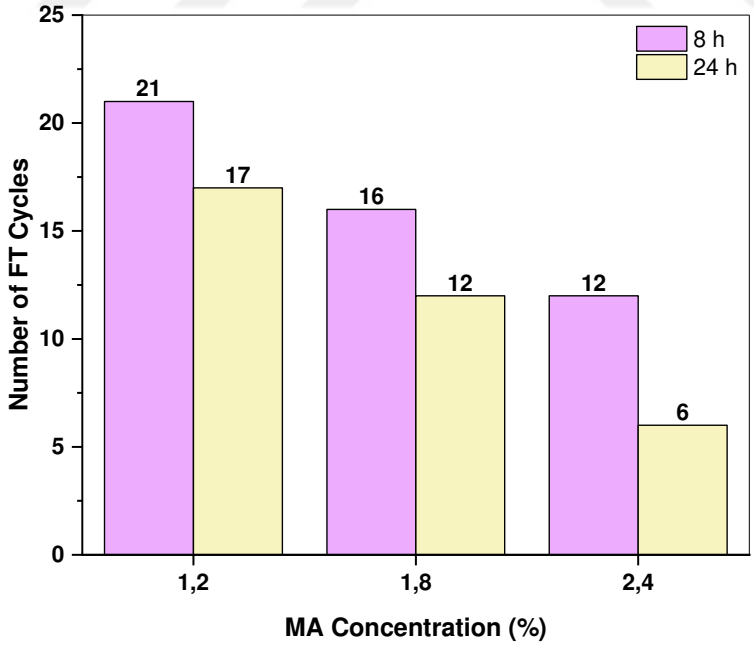

Figure 4.6. Effect of crosslinker concentration and frozen storage time on the number of FT cycles.

Figure 4.6. demonstrates the effect of crosslinker concentration and frozen storage time on gelation. The results showed that increasing crosslinker concentration decreased

the number of freeze-thaw cycles necessary to prepare a hydrogel. The reason is that during the frozen storage step, an esterification reaction occurs between CMC and the crosslinker, and increasing crosslinker concentration results in a more interconnected and stable network. In addition, as expected, increasing frozen storage time decreased the number of freeze-thaw cycles since gelation is a time-dependent process, and extending this duration allowed the biopolymer and the crosslinker to interact and form intermolecular bonds more, leading to a more robust hydrogel structure.

4.5.2 Effect of CMC molecular weight and concentration on gelation

To elucidate the impact of both the molecular weight and concentration of carboxymethyl cellulose on gelation, solutions were prepared with a crosslinker concentration equal to 30% of the weight of carboxymethyl cellulose, and the frozen storage time for gelation was determined to be 8 hours. The prepared aerogels using the formulations given in Table 3.1 are shown in Figure 4.7.

Figure 4.7. Photos of CMC aerogels from different CMC types and concentrations.

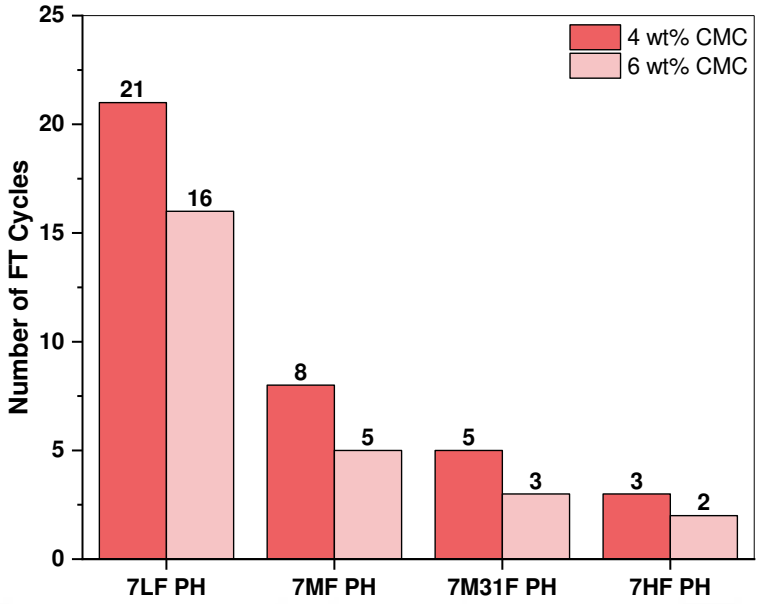

Figure 4.8. Effect CMC molecular weight and CMC concentration on the number of FT cycles.

Figure 4.8 shows the effect of CMC molecular weight and CMC concentration on the number of FT cycles to obtain a gel. An increase in both the molecular weight and concentration of CMC reduced the number of freeze-thaw cycles required to obtain a gel and led to a stronger gel. The impact of concentration may be attributed to the availability of more molecules that can participate in the esterification reaction. In addition, since CMC chains with a higher molecular weight have more entanglement points, the impact of high molecular weight can be explained by increased cellulose chain interactions.

4.6 Morphology of CMC aerogels

The network structure of the gels, and therefore the properties of the aerogels, are affected by the properties of precursors and the reaction parameters of the gelation processes.

4.6.1 Effect of frozen storage time and crosslinker concentration on morphology

CMC hydrogels with 1.2 wt% (w/w polymer) MA had weak networks, and due to the dissolution of the non-crosslinked polymer during the solvent exchange, hydrogels could not preserve their shape. Therefore, these aerogels' volumetric shrinkage and density could not be measured.

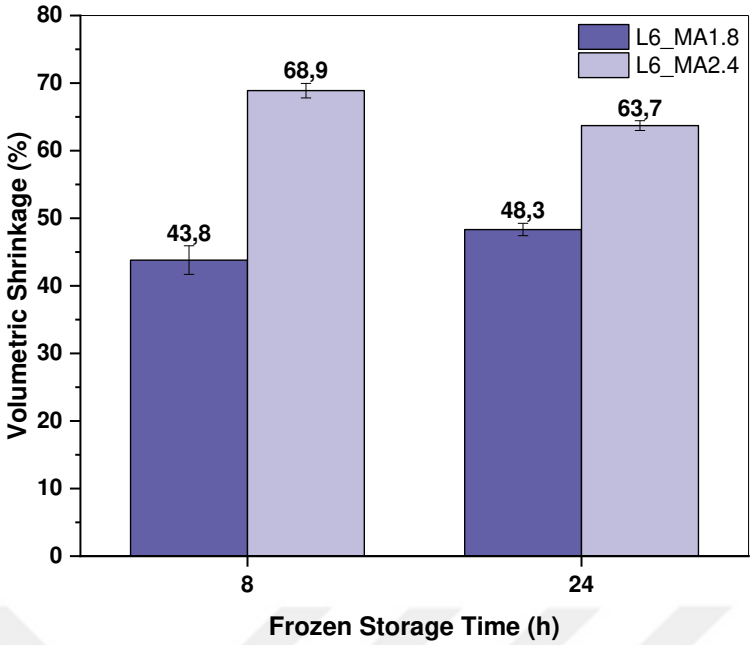

Figure 4.9. Volumetric Shrinkage of CMC aerogels.

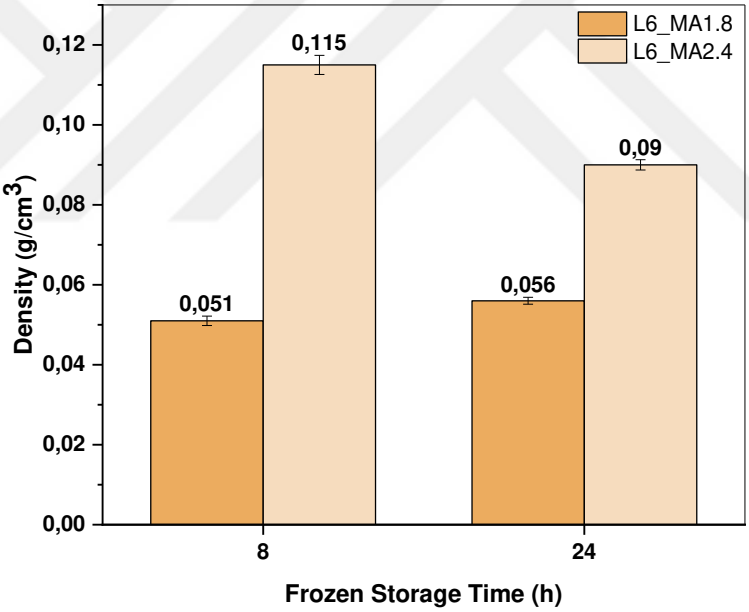

Figure 4.10. Densities of CMC aerogels.

As shown in Figures 4.9 and 4.10, aerogels with 1.8 wt% crosslinkers showed lower volumetric shrinkage, which is caused by the swelling during the initial solvent exchange steps. The swelling can be ascribed to a weaker structure due to the lower crosslinker concentration [40]. In addition, lower volumetric shrinkage of these aerogels led to lower densities.

The skeletal density of the prepared CMC aerogels was measured as 1.65 g/cm^3. The pore properties and the specific surface area (S_{BET}) of CMC aerogels were determined

by N_2 physisorption and are listed in Table 4.3.

Table 4.3. Properties of CMC aerogels.

Sample	Bulk Density (g/cm³)	Skeletal Density (g/cm³)	Porosity (%)	S_{BET} (m^2/g)	Single point pore Volume (cm^3/g)	Total Pore Volume (cm^3/g)	Macropore Volume (cm^3/g)	Average Pore Size - BJH (nm)	Average Pore Size - Macropore (nm)
L6_MA1.2_8h	-	1.65	-	122	1.52	-	-	49.7	-
L6_MA1.2_24h	-	1.65	-	166	1.84	-	-	44.3	-
L6_MA1.8_8h	0.051	1.65	96.91	214	1.82	19.00	17.18	34.0	355
L6_MA1.8_24h	0.056	1.65	96.61	208	1.82	17.25	15.43	35.0	332
L6_MA2.4_8h	0.115	1.65	93.03	176	0.92	8.09	7,17	20.9	184
L6_MA2.4_24h	0.090	1.65	94.55	180	0.99	10.51	9.52	21.8	233

Adsorption-desorption isotherms (Figure 4.11) showed that all CMC aerogels had isotherms of Type IV, indicating the presence of mesopores [136]. Additionally, the difference between the BJH pore volume and the total pore volume indicated the existence of macropores (Table 4.3).

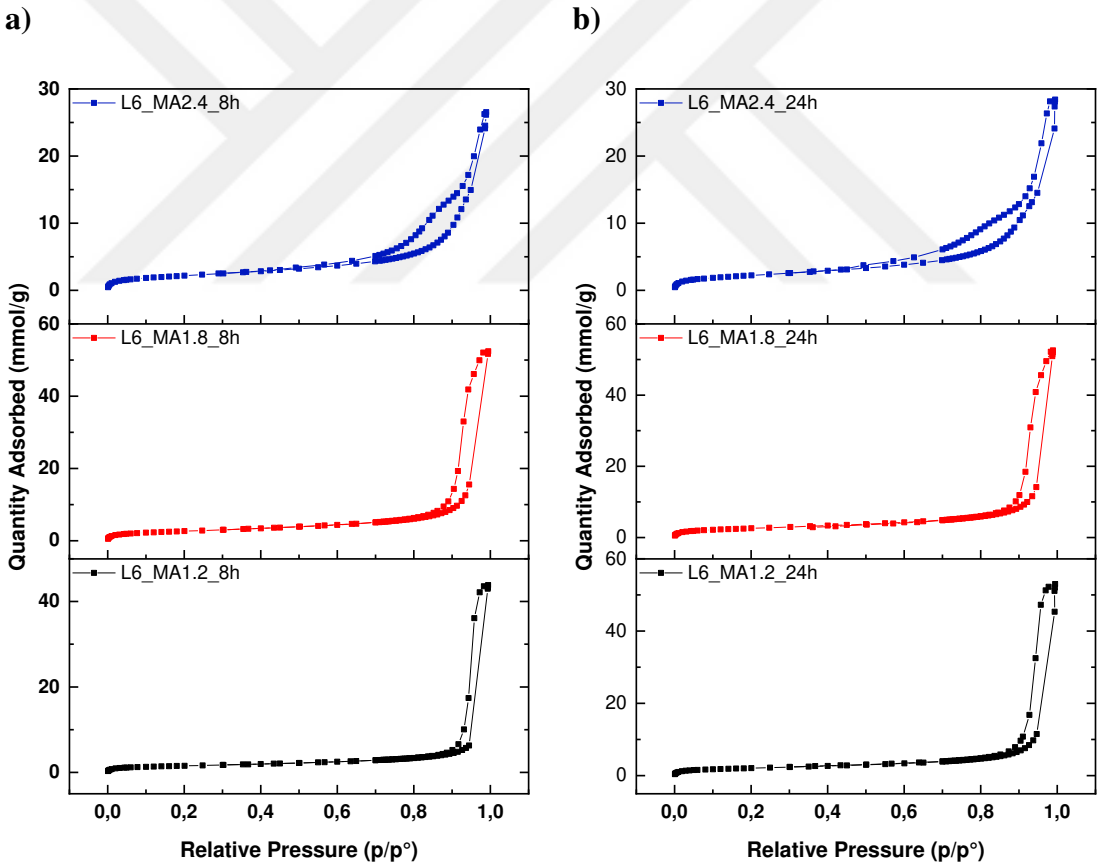

Figure 4.11. BET Isotherms of CMC aerogels a) 8h frozen storage b) 24h frozen storage.

Figure 4.12 presents the mesoporous pore size distributions of CMC aerogels, which were differential pore volumes plotted against the pore width. The results indicated that increasing crosslinker concentration decreased pore diameter, pore volume, and

porosity. The observed decrease might be explained by a higher degree of crosslinking between the gel network strands, resulting in shrinkage of the gel structure, a reduction in overall pore volume, and a smaller average pore size.

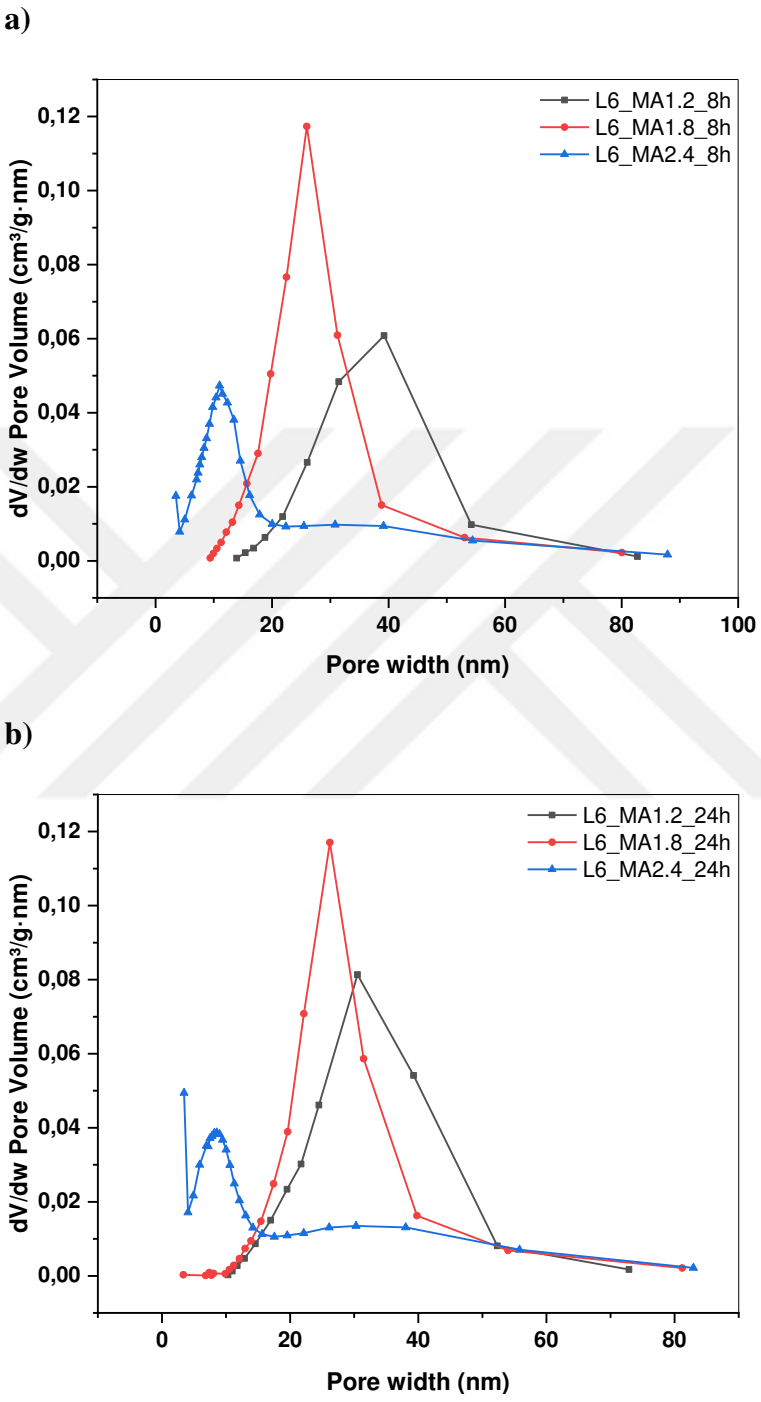

Figure 4.12. Mesoporous pore size distributions of CMC aerogels a) 8h frozen storage b) 24h frozen storage.

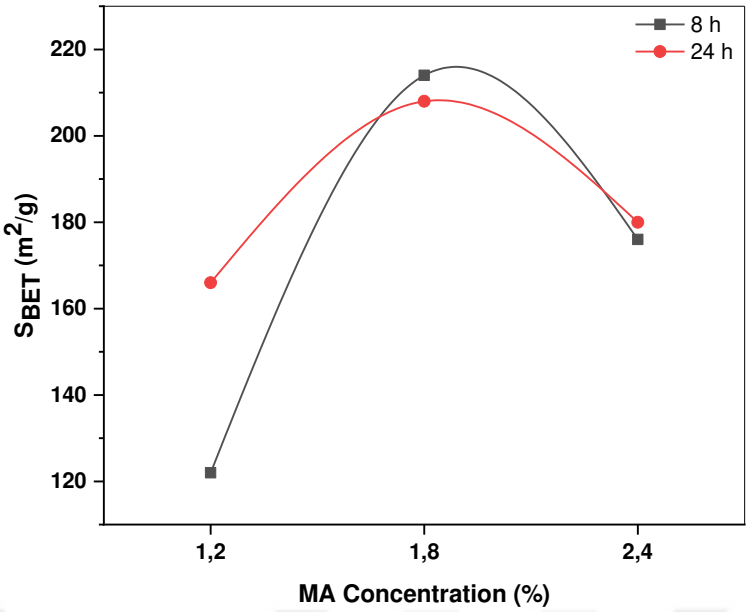

Figure 4.13. S_{BET} as a function of the crosslinker concentration.

The specific surface area of biopolymer aerogels can vary according to the chemical structure of the biopolymer used and the synthesis conditions. Generally, the specific surface areas of biopolymer aerogels are between 100 to 600 m²/g, and cellulose aerogels have been reported to have surface areas ranging from 150 to 485 m²/g [136]. Our results showed that the specific surface areas of low molecular weight CMC aerogels with 6 wt% CMC concentration were between 122 m²/g and 214 m²/g. Interestingly, the specific surface area of CMC aerogels first increased and then decreased with the increasing crosslinker concentration (Table 4.3 & Figure 4.13). The increase in the specific surface area can be explained by the more interconnected network with smaller particles and the narrowing of the pore size distribution (Figure 4.12), which stems from higher crosslinker concentration. Moreover, increased crosslinker concentration may strengthen and stabilize the porous structure of the gel, preventing pore collapse during supercritical drying and contributing to a larger total surface area. However, further increasing the crosslinker concentration decreased the specific surface area, which may be attributed to the higher volumetric shrinkage. Additionally, excessive crosslinking may lead to the formation of larger pores and block smaller pores, further decreasing the surface area. Additionally, frozen storage time did not significantly influence the specific surface area of aerogels.

SEM analysis indicated that the pore volume of CMC aerogels is primarily macroporous, and there is little mesoporosity consistent with nitrogen physisorption results (Figure 4.14). SEM images showed that CMC aerogels had a fibrous structure and

interconnected network with mesopores and macropores. SEM analysis also showed that L6_MA2.4 aerogels had a more uniformly distributed pore structure, which can be attributed to the higher crosslinker concentration. Results showed that frozen storage time influenced overall gelation time; however, it had no significant impact on aerogel pore morphology.

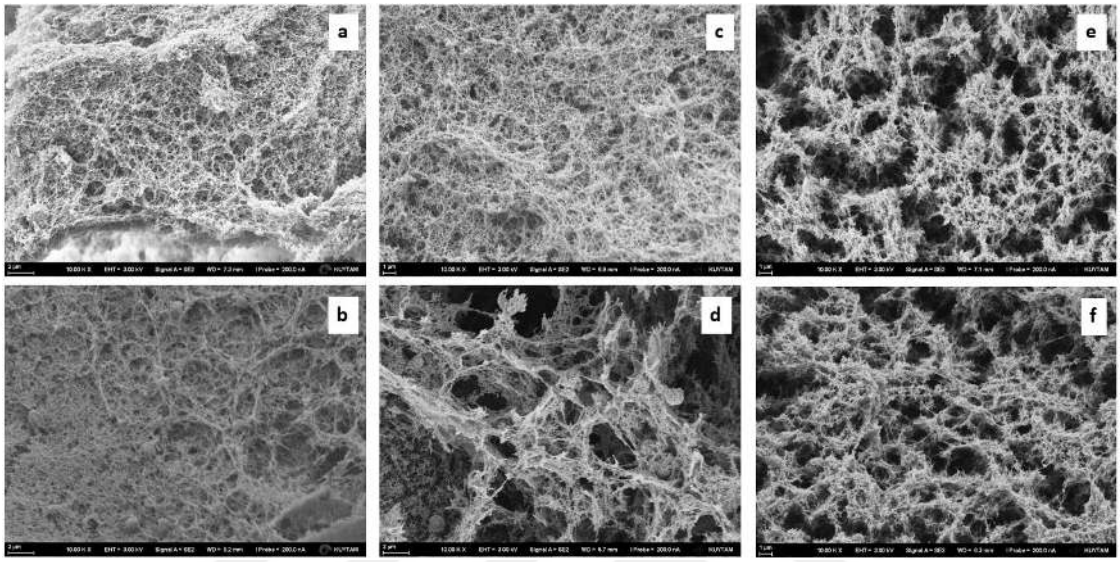

Figure 4.14. SEM images of CMC aerogels. a) L6_MA1.2_8h b) L6_MA1.2_24h c) L6_MA1.8_8h d) L6_MA1.8_24h e) L6_MA2.4_8h f) L6_MA2.4_24h, 10KX magnification.

4.6.2 Effect of molecular weight and concentration on morphology

Figure 4.15 shows the effect of molecular weight and concentration on aerogel density. As expected, increasing CMC concentration increased the aerogel density due to the higher solid content. Additionally, a slight increase in aerogel density was observed with the increase in molecular weight. It was assumed that high molecular weight promoted tighter packing of the network strands, leading to denser structures. Interestingly, low molecular CMC aerogel (7LF PH) with 4 wt% CMC concentration showed slightly higher density than medium molecular weight aerogel; this can be attributed to the higher volumetric shrinkage observed.

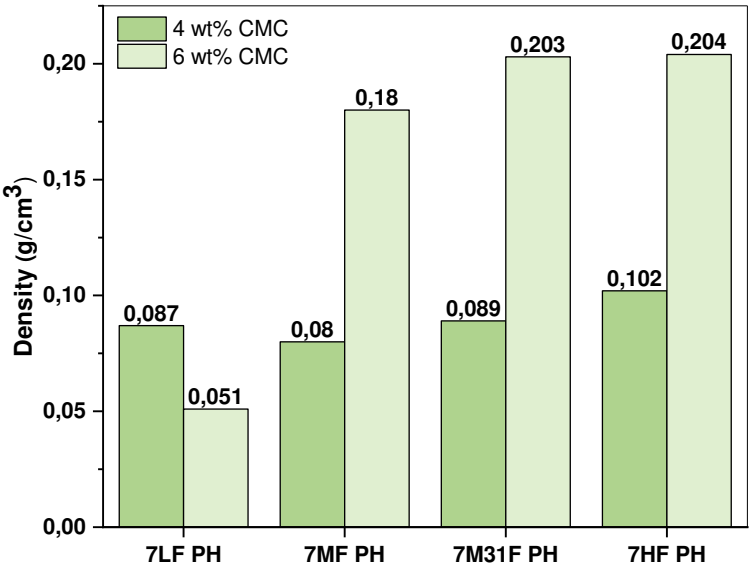

Figure 4.15. Densities of CMC aerogels from different CMC sources and aqueous concentrations.

The pore properties and the specific surface area (S_{BET}) of CMC aerogels from different CMC sources and aqueous concentrations were determined by N_2 physisorption and are listed in Table 4.4. According to the results, the porosity of CMC aerogels decreased with increasing CMC concentration in solution. Additionally, as the concentration increased, the specific pore volume decreased except for the low molecular weight CMC source. Moreover, with the increasing molecular weight, average pore size and total pore volume decreased except for the M6_MA1.8_8h, which may be attributed to the higher macropore volume content of M6_MA1.8_8h.

Table 4.4. Properties of CMC aerogels from different CMC sources and aqueous concentrations.

Sample	Porosity (%)	BET Surface Area (m^2/g)	Single point pore Volume (cm^3/g)	Total Pore Volume (cm^3/g)	Macropore Volume (cm^3/g)	Average Pore Size - BJH (nm)	Average Pore Size - Macropore (nm)
L6_MA1.8_8h	96.91	214	1.82	19.00	17.18	33.96	355
M6_MA1.8_8h	89.07	50	0.28	4.94	4.66	22.5	399
M31F6_MA1.8_8h	87.68	101	0.71	4.31	3.60	28.31	171
H6_MA1.8_8h	87.62	92	0.48	4.29	3.81	20.81	186
L4_MA1.2_8h	94.73	113	0.67	10.89	10.22	23.60	384
M4_MA1.2_8h	95.17	96	0.66	11.94	11.27	28.13	497
M31F4_MA1.2_8h	94.60	118	0.65	10.62	9.97	22.09	361
H4_MA1.2_8h	93.80	127	0.82	9.17	8.35	25.61	288

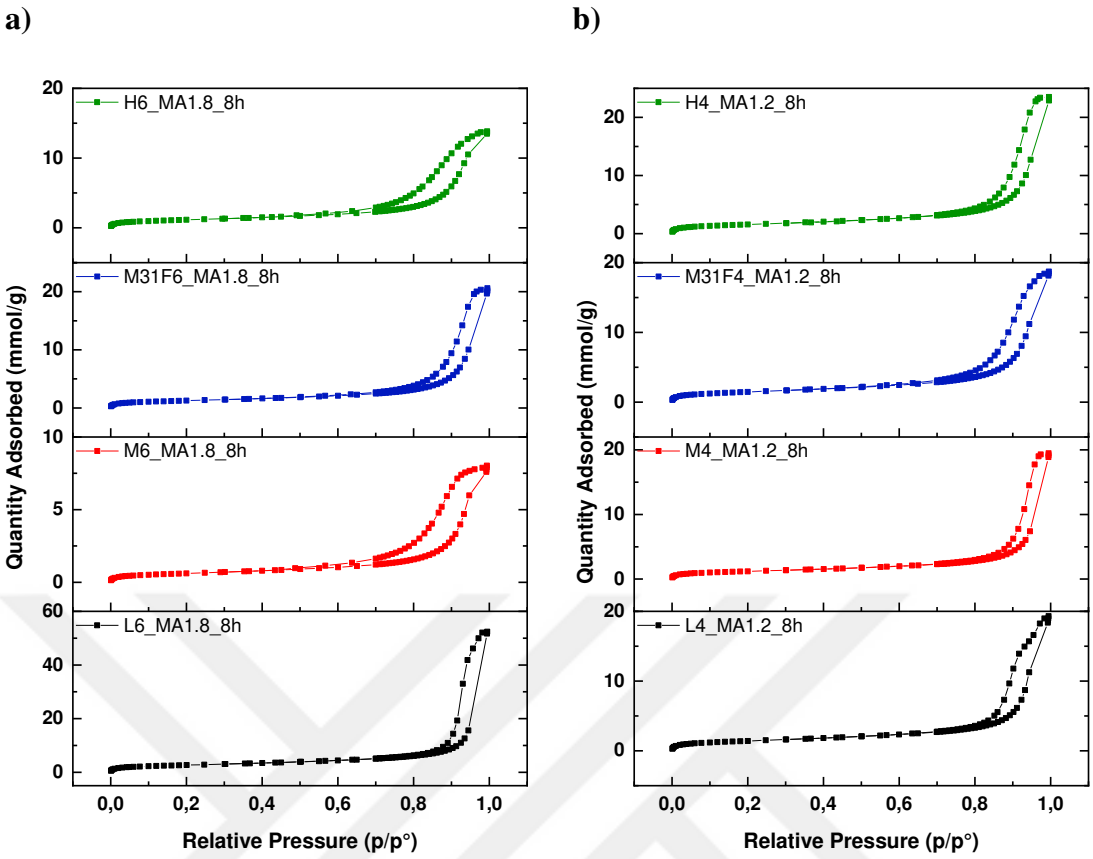

Figure 4.16. BET Isotherms of CMC aerogels from a) 6 wt% CMC aqueous solution b) 4 wt% CMC aqueous solution.

Nitrogen adsorption-desorption isotherms revealed that all CMC aerogels exhibited Type IV isotherm, characteristic of mesoporous materials (Figure 4.16). Further analysis using the BJH method and total pore volume calculations suggested the presence of additional macropores (Table 4.4).

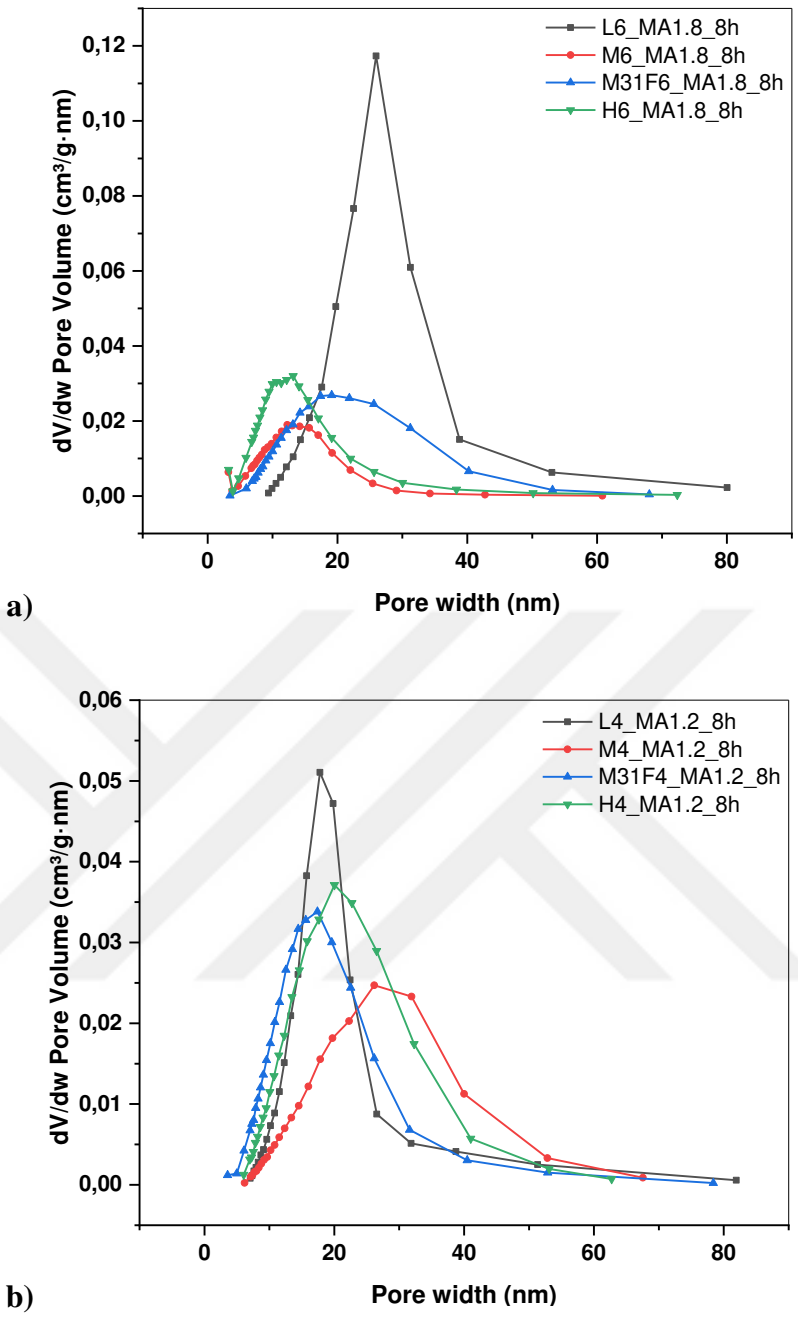

Figure 4.17. Mesoporous pore size distributions of CMC aerogels from a) 6 wt% CMC aqueous solution b) 4 wt% CMC aqueous solution.

The mesoporous pore size distributions of CMC aerogels from different CMC sources and aqueous concentrations are shown in Figure 4.17. A broad pore size distribution was observed for aerogels prepared from higher molecular weight CMC sources. As BJH pore volume approximation is valid only for mesopores (2–50 nm), the data showed major pore size distribution peaks beyond 50 nm and a peak in the range of 10–30 nm, which is in good agreement with the results of SEM (Figure 4.18 and Figure 4.19).

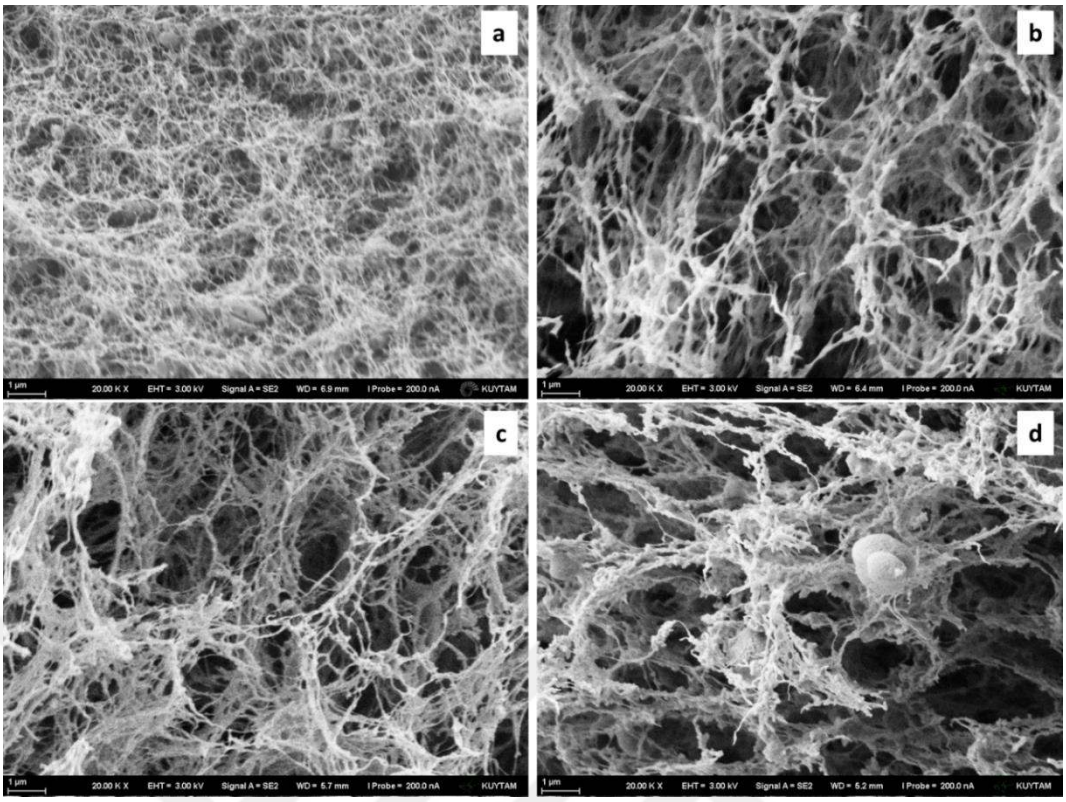

Figure 4.18. SEM images of CMC aerogels a) L6_MA1.8_8h b) M6_MA1.8_8h c) M31F6_MA1.8_8h d) H6_MA1.8_8h, 20KX magnification.

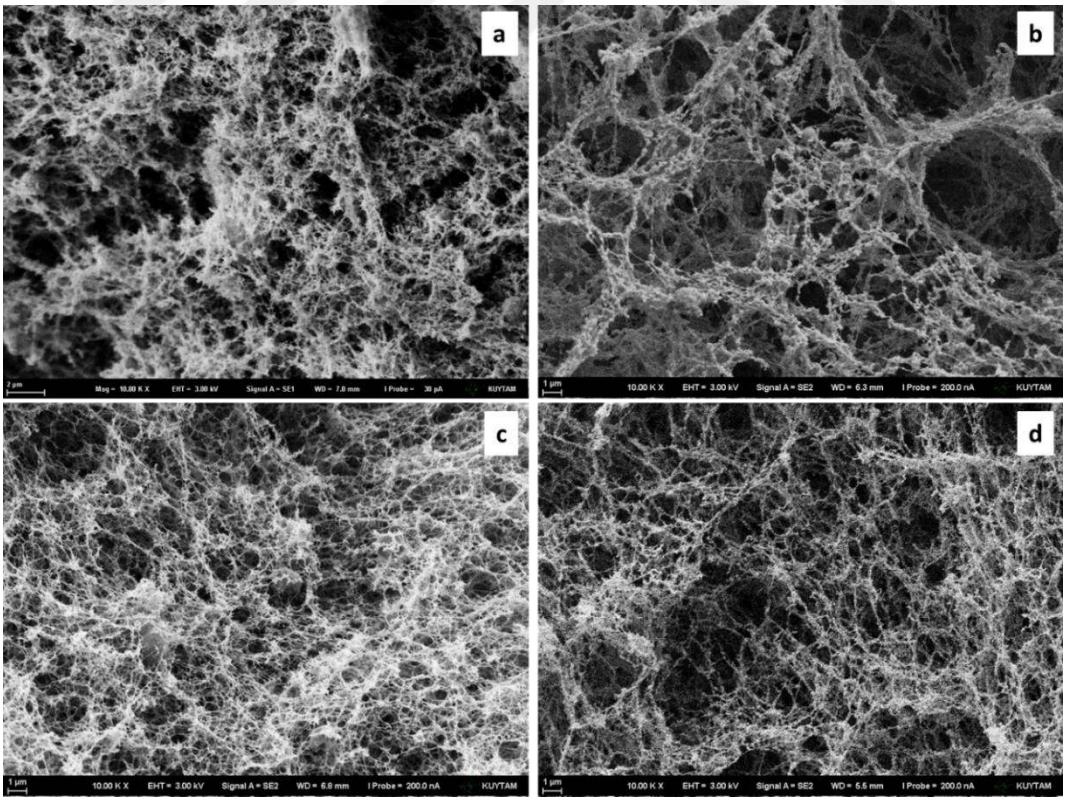

Figure 4.19. SEM images of CMC aerogels a) L4_MA1.2_8h b) M4_MA1.2_8h c) M31F4_MA1.2_8h d) H4_MA1.2_8h, 10KX magnification.

Investigating the specific surface area (S_{BET}) trends of CMC aerogels revealed intriguing dependencies on both CMC concentration and molecular weight (Figure 4.20). When aerogels from 4 different CMC sources were fabricated from a 6 wt% CMC solution, it was found that increasing molecular weight initially led to a significant decrease in specific surface area, followed by a subsequent increase of approximately 50 m²/g before declining by about 10 m²/g. Conversely, aerogels prepared from a 4 wt% CMC solution exhibited higher specific surface areas than aerogels from a 6 wt% solution, except for the lowest molecular weight. This suggests that while higher molecular weight initially led to decreased surface area, at lower CMC concentrations, the impact of molecular weight on surface area was less pronounced.

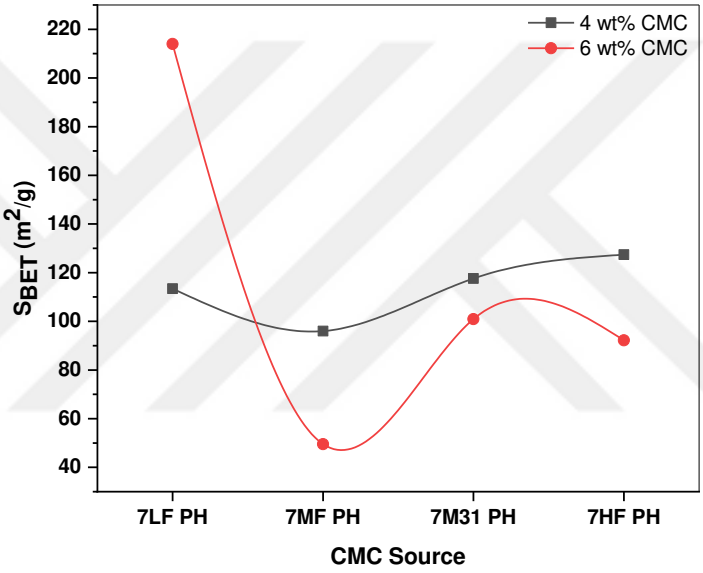

Figure 4.20. S_{BET} as a function of the CMC sources and aqueous concentrations.

4.7 Crosslinking of CMC aerogels

The proposed crosslinking mechanism between CMC-CMC-MA is given in Figure 4.21. FTIR and NMR analyses were conducted to determine the crosslinking mechanism of CMC aerogels.

FTIR spectra of NaCMC and MA are presented in Figure 4.22. The FTIR spectrum of NaCMC showed characteristic absorption peaks at 3255 cm^{-1} (O-H stretching), 2900 cm^{-1} (C-H stretching), 1587 cm^{-1} (C=O asymmetric carboxylate stretching), 1412 cm^{-1} (C-H symmetric carboxylate stretching), 1324 cm^{-1} (C-H symmetric carboxylate stretching) and 1018 cm^{-1} (C-O stretching) [103][98]. Maleic anhydride had a weak symmetric carbonyl (C=O) stretching peak at 1854 cm^{-1} and a strong asymmetric carbonyl (C=O) stretching peak at 1773 cm^{-1} [137].

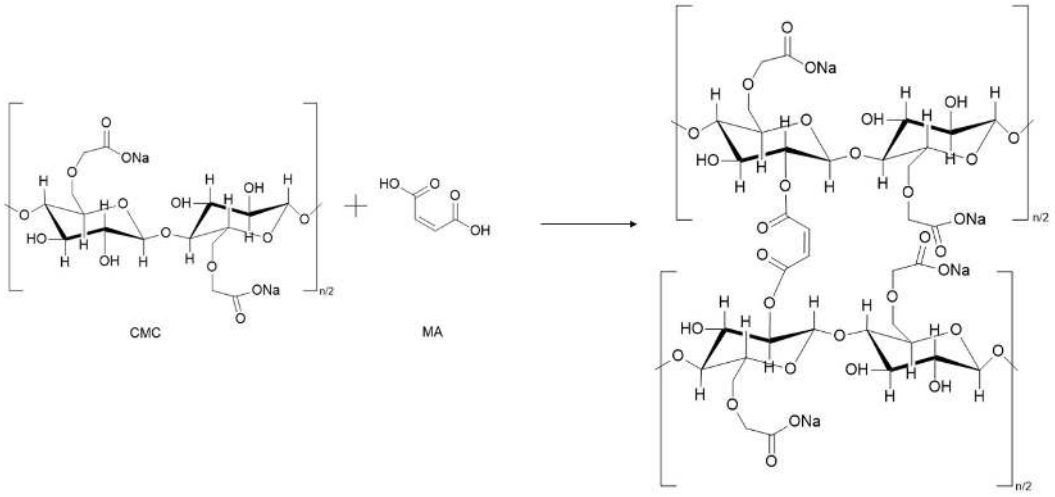

Figure 4.21. The proposed crosslinking mechanism between CMC-CMC-MA.

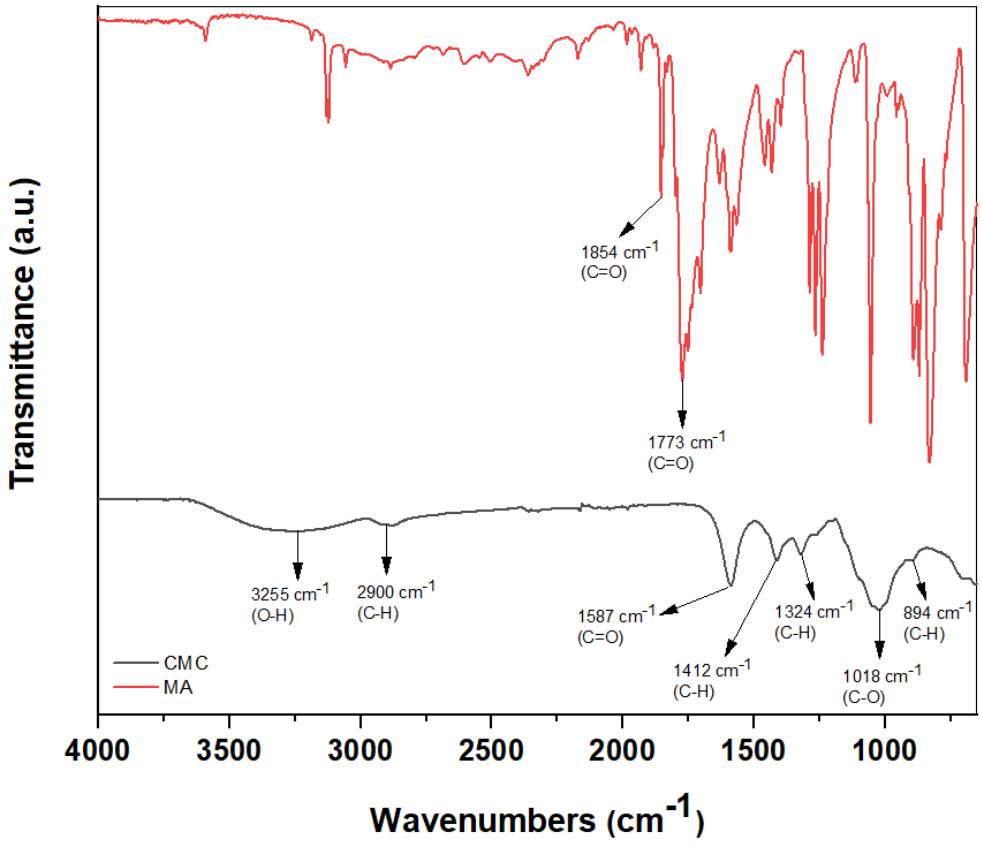

Figure 4.22. FTIR spectra of CMC and MA.

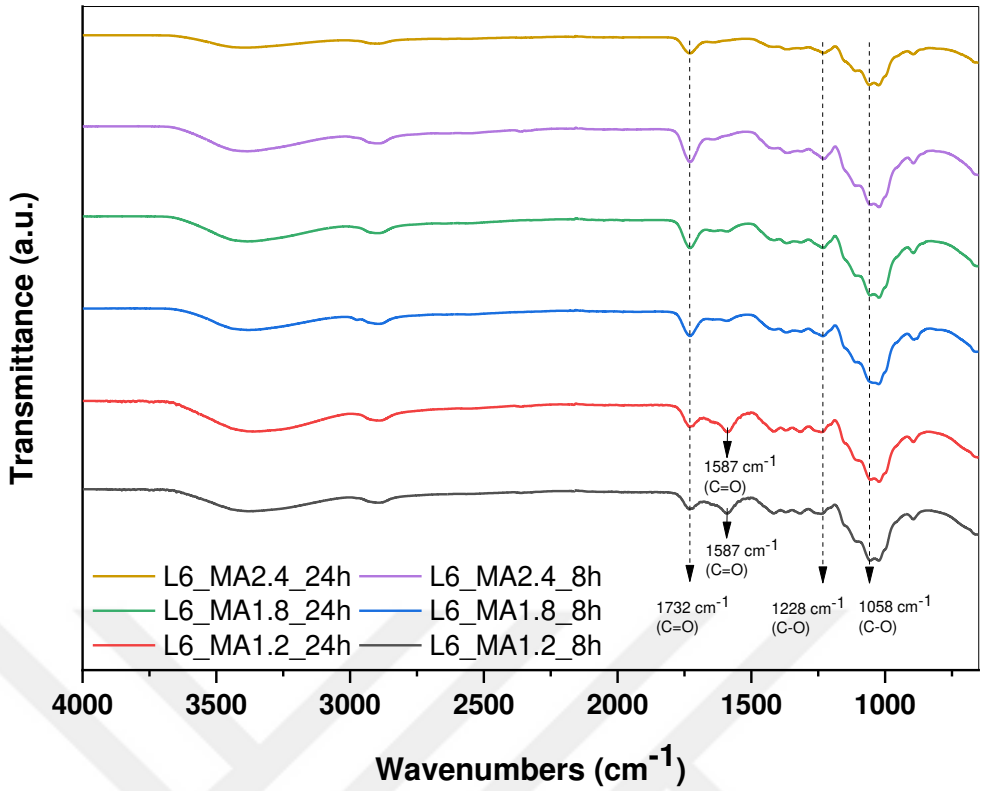

Figure 4.23. FTIR spectra of MA crosslinked CMC aerogels.

The FTIR spectra of all CMC aerogels (Figure 4.23) showed that new peaks arose at 1732-1730 cm^{-1} (C=O), 1228 cm^{-1} (C-O), and 1058 cm^{-1} (C-O), which indicated the formation of ester bonds between the hydroxyl groups of CMC and carboxyl groups of MA [103]. Additionally, no peaks at 1854 cm^{-1} and 1773 cm^{-1} confirmed the absence of non-reacted maleic anhydride [138]. With the increasing crosslinker concentration, a slight shift to higher wavenumbers was observed. This can be related to the crosslinking between the OH groups [95]. Aerogels with 20 % w/w polymer crosslinker showed peaks at 1589 cm^{-1}, which can be attributed to insufficient ester linkage and cross-linking.

The chemical structure and symbolic representation of carbon atoms of NaCMC and the solid state 13C-NMR spectrum of CMC aerogel are given in Figure 4.24. The carbon atom signals of NaCMC which are between 98-109 ppm (C1), 68-80 ppm (C2,3,5,7), 81-89 ppm (C4), 56-6 ppm (C6), and 175-183 ppm (COO-) were obtained from elsewhere [98]. The carbon atom signals of MA were obtained from elsewhere [135]. MA shows a sharp signal at 136 ppm (=C-H) and a carbonyl signal at 165 ppm (O-C=O) [135]. The broad peak of CMC aerogel at 172.43 ppm indicated the ester formation.

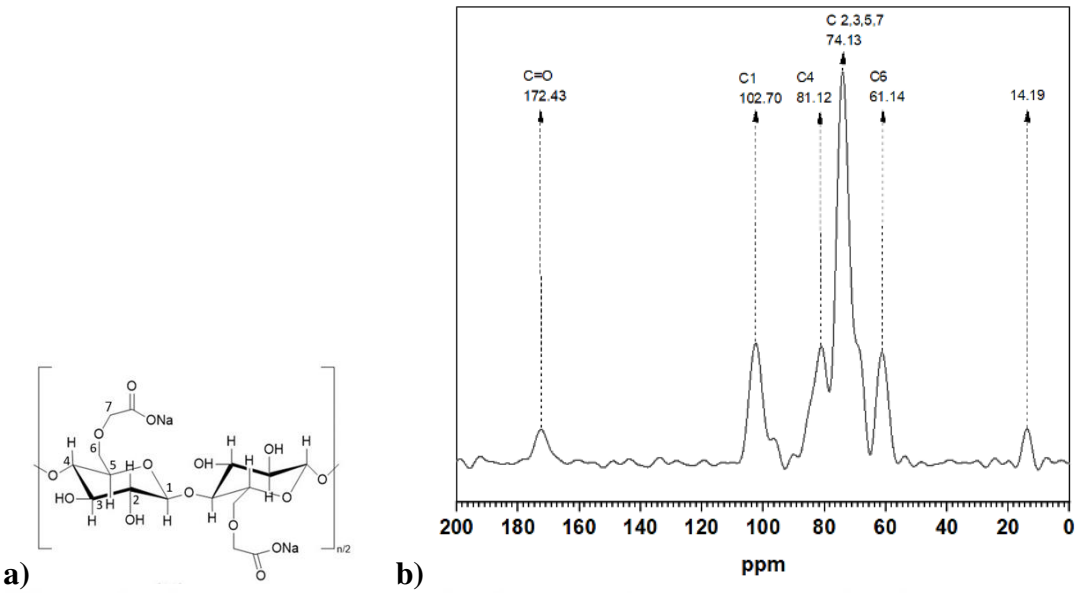

Figure 4.24. a) The chemical structure of NaCMC b) The solid-state 13C-NMR spectrum of CMC aerogel.

FTIR analyses of the CMC aerogels from different CMC sources and aqueous concentrations were also conducted (Figure 4.25 and Figure 4.26). It was noted that ester bonds were formed in all CMC aerogels; however, no significant difference in the intensity of peaks was observed depending on the molecular weight or concentration of the solution.

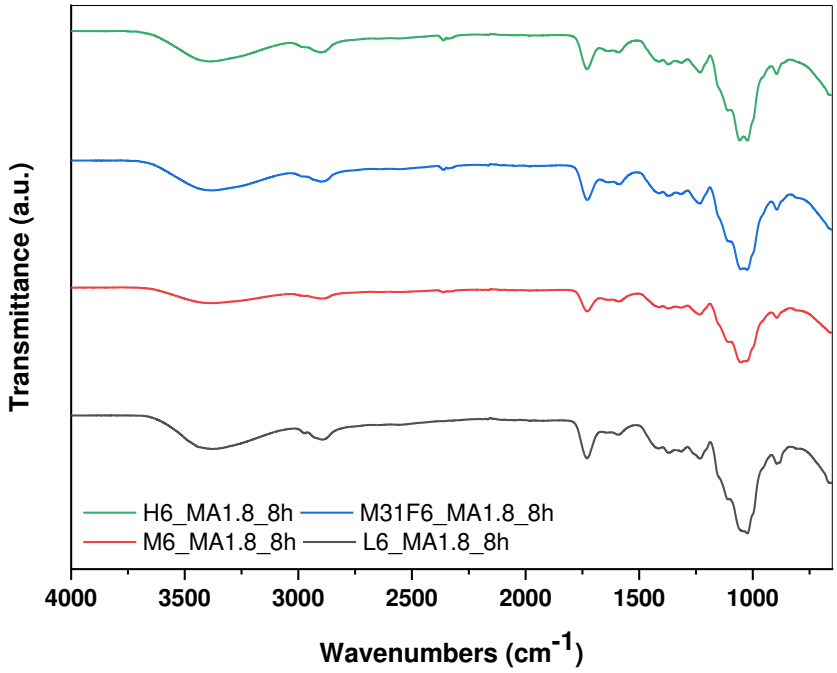

Figure 4.25. FTIR spectra of CMC aerogels from 6 wt% aqueous CMC concentration.

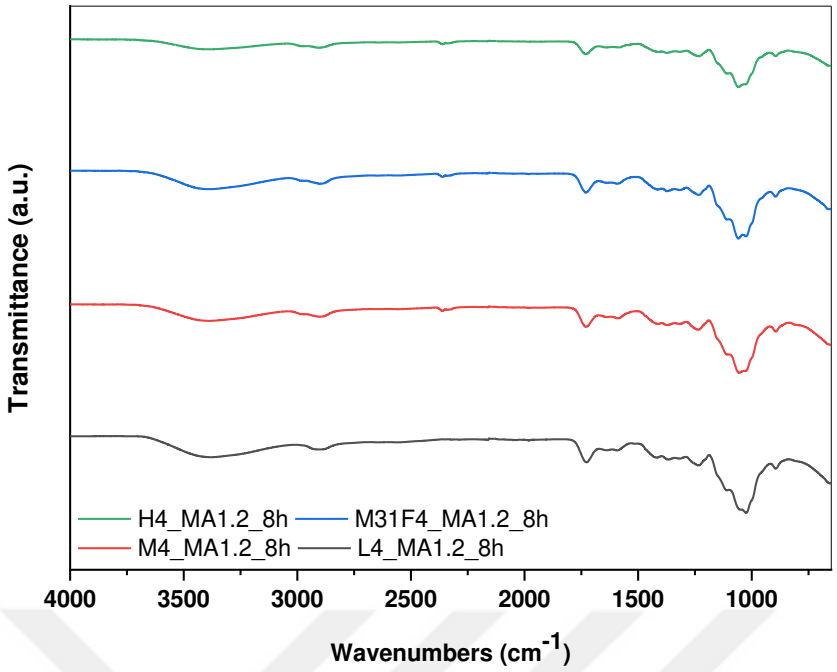

Figure 4.26. FTIR spectra of CMC aerogels from 4 wt% aqueous CMC concentration.

4.8 Thermal properties of CMC aerogels

The thermal conductivity values of prepared aerogels are given in Figure 4.27. Since the reliability of hot-disk measurement is poor, the results were used as a relative indicator [139]. Additionally, the thermal conductivity values of the samples were measured without dehumidification. Cellulose-based aerogels are typically hydrophilic, and humidity can significantly impact their thermal conductivity. As humidity increases, water molecules can adsorb onto the surface of the aerogel, potentially filling some of the pore space. This can further increase thermal conductivity as water is a better conductor of heat than air.

The lowest thermal conductivity was measured as 0.038 W/mK, which may be ascribed to the low density of L6_MA1.8 even though it had larger pore sizes than L6_MA2.4. In this case, the gas contribution to the thermal conductivity increases, and the solid backbone contribution decreases. According to Figure 4.27b, the thermal conductivity of aerogels prepared from 6 wt% CMC solution was higher than those prepared from 4 wt% CMC solution. Since density significantly affects solid thermal conductivity, this may be attributed to the higher density of aerogels prepared from 6 wt% CMC solution [140]. In addition, the results indicated that the molecular weight of CMC did not significantly impact the thermal conductivity of aerogels. When comparing aerogels prepared from a 6 wt% CMC solution, it was observed that the L6_MA1.8_8h

exhibited the lowest thermal conductivity. This phenomenon could be attributed to its higher porosity, as an increase in porosity not only reduces the density but also restricts the motions of phonons in the solid structure [60].

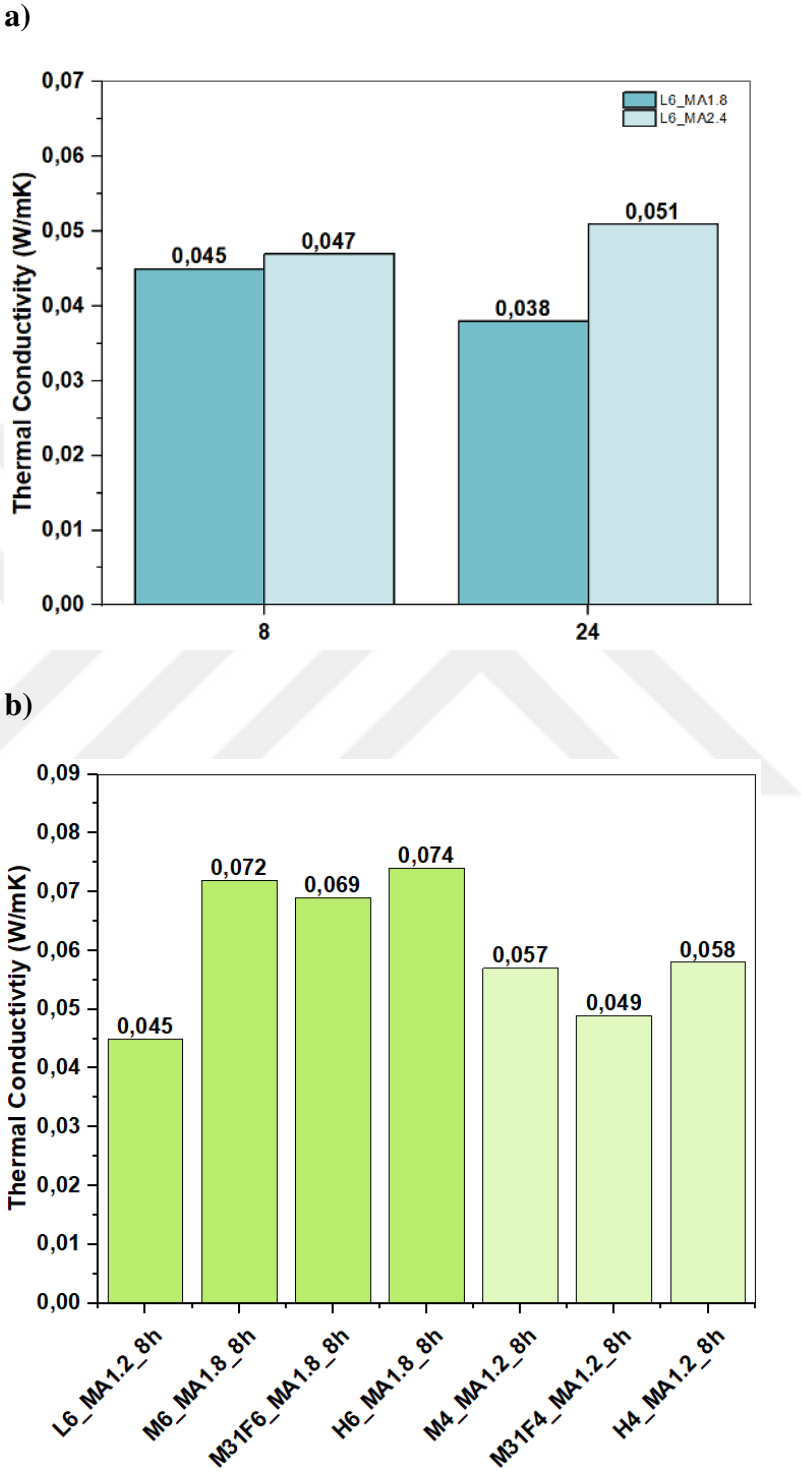

Figure 4.27. Thermal Conductivities of the CMC aerogels from a) different crosslinker concentrations and frozen storage times and b) different CMC sources and aqueous concentrations.

Theoretical thermal conductivity values for CMC (Carboxymethyl cellulose) aerogels

have been calculated (Figure 4.28, Appendix A.2) and compared with experimental values obtained through the hot-disk method. According to the results, the theoretically calculated values were lower than the experimental values measured using the hot-disk method.

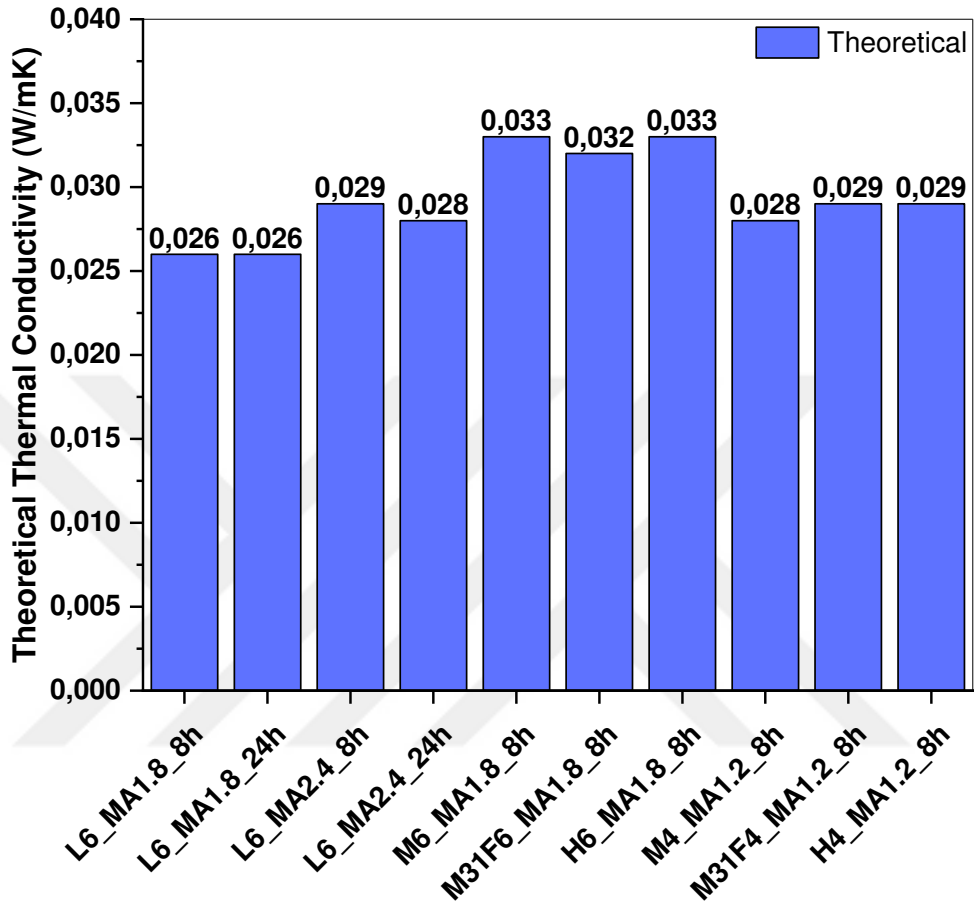

Figure 4.28. Theoretical thermal conductivity values of CMC aerogels.

4.9 Effect of intermolecular crosslinking on CMC aerogels

To promote intermolecular cross-linking in CMC aerogels, PVA was added to the CMC aqueous solution at a rate of one-third the weight of CMC. CMC/PVA hybrid aerogels were prepared in 3 main steps: first, CMC/PVA hybrid hydrogels were formed, then solvent exchange with ethanol took place, and finally, alcogels were supercritically dried with CO_2. A photo of CMC/PVA hybrid aerogel is given in Figure 4.29.

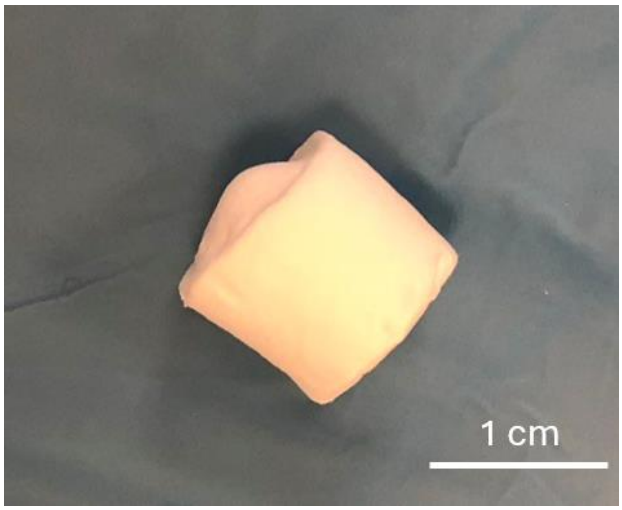

Figure 4.29. A photo of CMC/PVA hybrid aerogel.

4.9.1 Morphology of CMC/PVA hybrid aerogels

The volumetric shrinkages of CMC/PVA aerogels are illustrated and compared with those of CMC aerogels in Figure 4.30. The findings indicated that CMC/PVA hybrid aerogels exhibited slightly lower volumetric shrinkages than CMC aerogels. This difference may be attributed to the enhanced network strength resulting from intermolecular crosslinking.

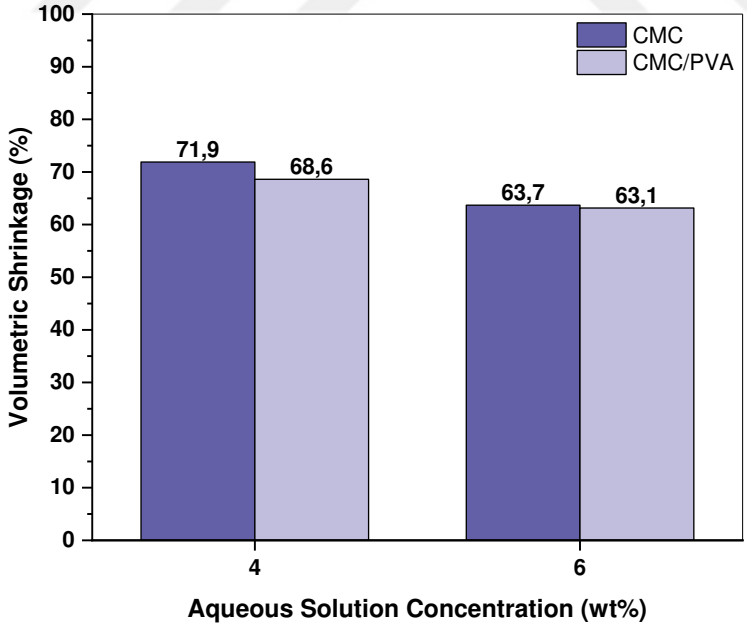

Figure 4.30. Volumetric Shrinkage of CMC and CMC/PVA hybrid aerogels.

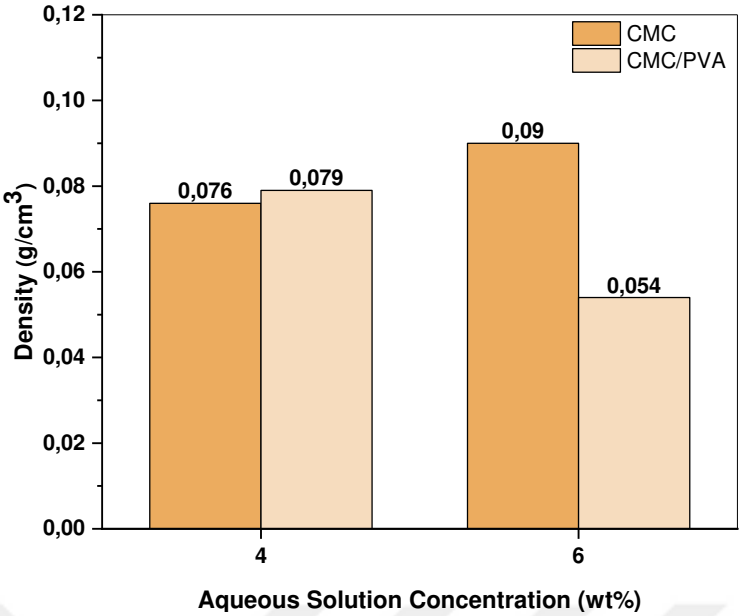

Figure 4.31. Densities of CMC and CMC/PVA hybrid aerogels.

Intriguing results were obtained after comparing the densities of CMC and CMC/PVA hybrid aerogels fabricated from various concentrations of aqueous solutions (Figure 4.31). Notably, aerogels produced from 4 wt% CMC and CMC/PVA aqueous solutions exhibited comparable densities. However, a significant density difference was observed in aerogels prepared from 6 wt% CMC and CMC/PVA aqueous solutions, which may be ascribed to the higher porosity and larger total pore volume of the CMC/PVA6 aerogels.

The skeletal density of the prepared CMC aerogels was measured as 1.69 g/cm^3. The pore properties and the specific surface area (S_{BET}) of CMC aerogels were determined by N_2 physisorption and are listed in Table 4.5.

Table 4.5. Properties of CMC and CMC/PVA hybrid aerogels.

Sample	Skeletal Density (g/cm^3)	Porosity (%)	S_{BET} (m^2/g)	Single point pore Volume (cm^3/g)	Total Pore Volume (cm^3/g)	Macropore Volume (cm^3/g)	Average Pore Size - BJH (nm)	Average Pore Size - Macropore (nm)
CMC4	1.65	95.38	23	0.13	12.55	12.42	22.64	2192
CMC/PVA4	1.69	95.33	184	0.65	12.07	11.41	12.14	262
CMC6	1.65	94.55	180	0.99	10.51	9.52	21.8	233
CMC/PVA6	1.69	96.75	144	0.61	17.59	16.97	16.57	488

Adsorption-desorption isotherms (Figure 4.32) showed that CMC/PVA hybrid aerogels had isotherms of Type IV, indicating the presence of mesopores [136]. Additionally, the difference between the BJH pore volume and the total pore volume indicated the existence of macropores (Table 4.5).

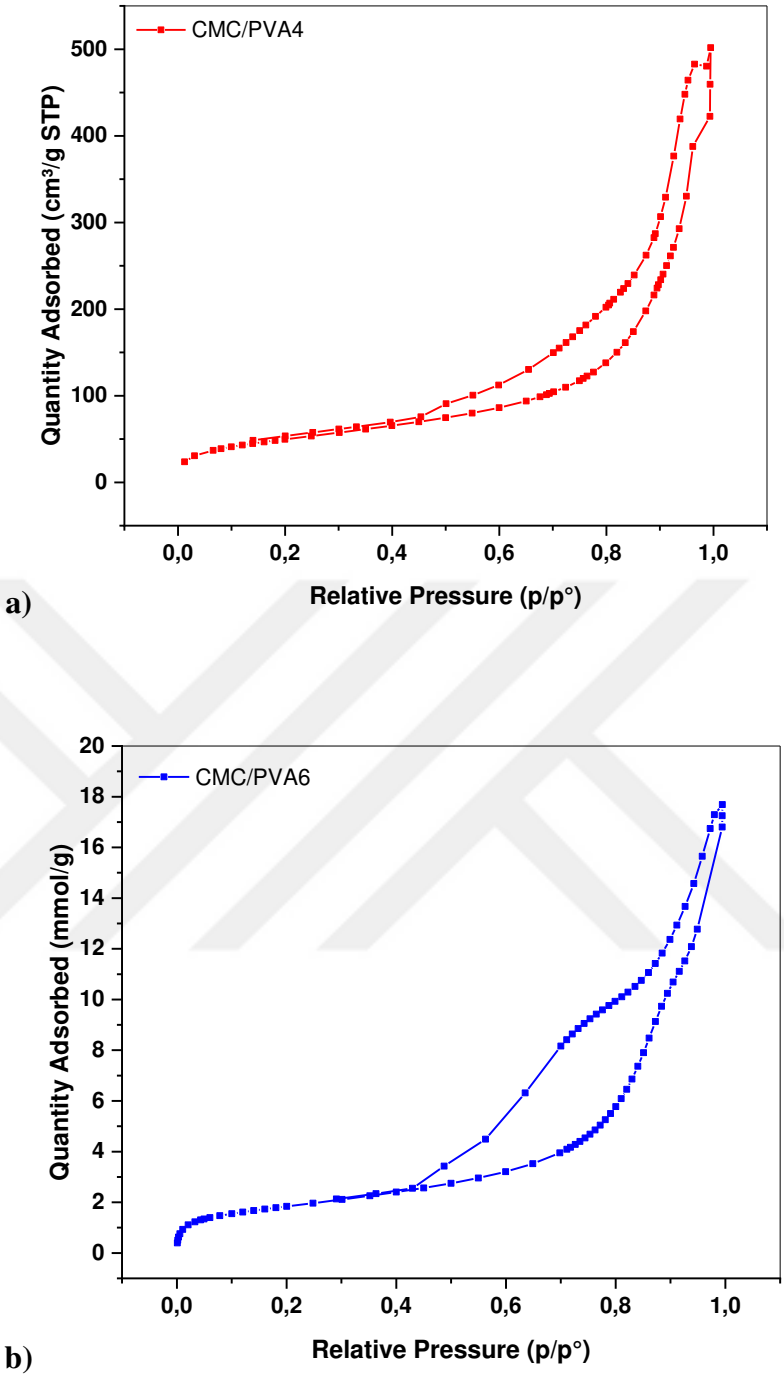

Figure 4.32. BET Isotherms of CMC/PVA hybrid aerogels from a) 4 wt% aqueous solution b) 6 wt% aqueous solution.

When comparing the aerogels from 6 wt% aqueous solutions, surprisingly, the S_{BET} of the CMC/PVA hybrid aerogel was smaller than the S_{BET} of the CMC aerogel. This phenomenon could be attributed to the presence of higher macropore volume and larger macropore sizes within the CMC/PVA aerogel matrix.

Figure 4.33 presents the mesoporous pore size distributions of CMC/PVA hybrid aerogels, which were differential pore volumes plotted against the pore width. The results displayed that adding PVA decreased the BJH average pore size but increased the average pore size and total pore volume owing to the formation of additional pores with small diameters. Interestingly, a comparison between CMC/PVA4 and CMC/PVA6 revealed that increasing polymer concentration increased the total pore volume, especially macropore volume and pore sizes.

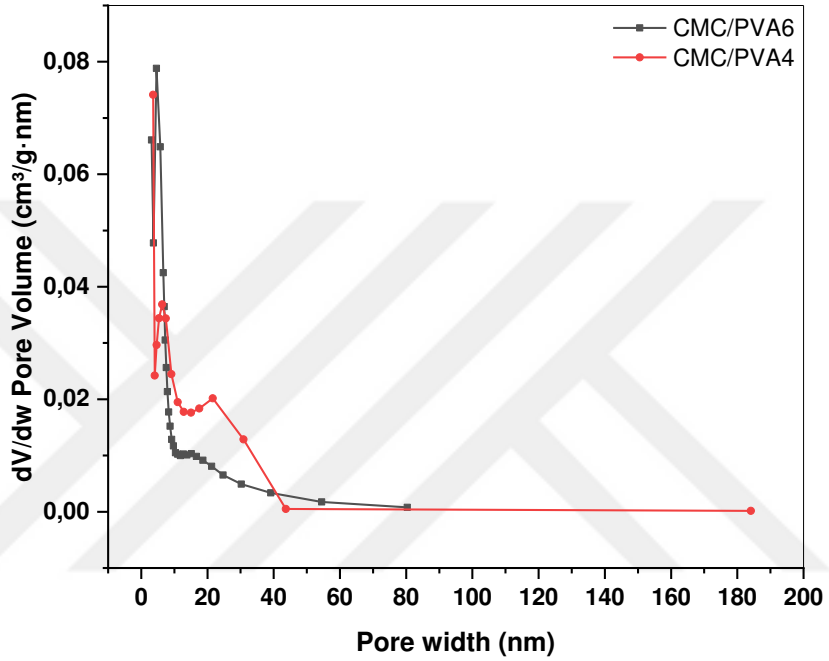

Figure 4.33. Mesoporous pore size distributions of CMC/PVA hybrid aerogels.

The presence of macroporous structures within the CMC/PVA hybrid aerogels was further supported by SEM analysis (Figure 4.34). The SEM images revealed fibrous structures characterized by interconnected networks featuring a combination of mesopores and macropores.

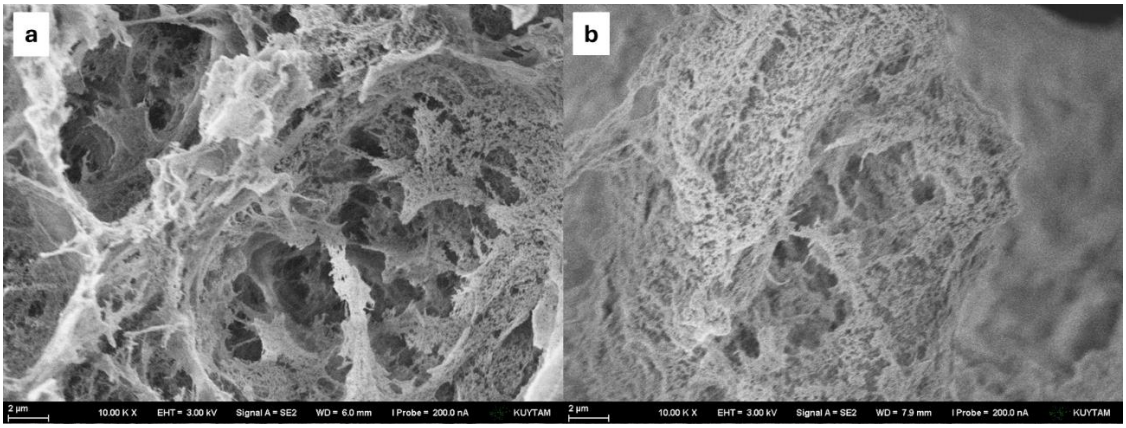

Figure 4.34. SEM images of CMC/PVA hybrid aerogels a) from 4 wt% aqueous concentration b) from 6 wt% aqueous concentration, 10KX magnification.

4.9.2 Crosslinking of CMC/PVA hybrid aerogels

The proposed crosslinking mechanism between CMC-PVA-MA is given in Figure 4.35. FTIR and NMR analyses were conducted to determine the crosslinking mechanism of CMC/PVA hybrid aerogels.

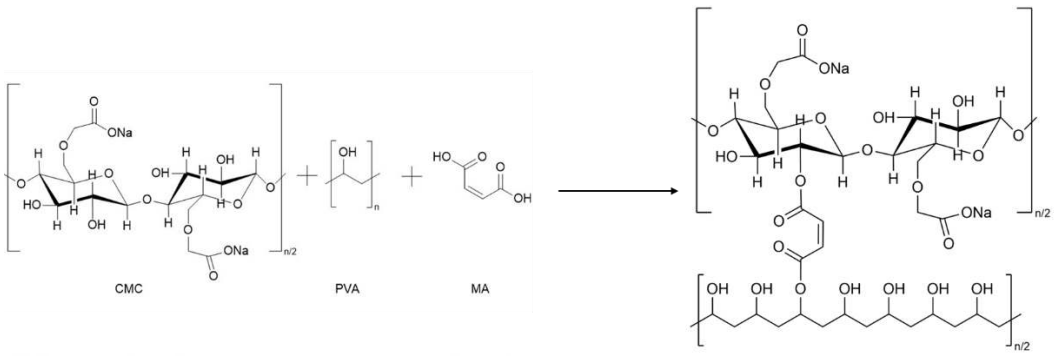

Figure 4.35. The proposed crosslinking mechanism between CMC-PVA-MA.

FTIR spectra of NaCMC, PVA and MA are presented in Figure 4.36. Characteristic absorption peaks of PVA are symmetric stretching 1418 cm^{-1} (C-H), and 1323 cm^{-1} (C-H), and C-O stretching at 1018 cm^{-1} [98].

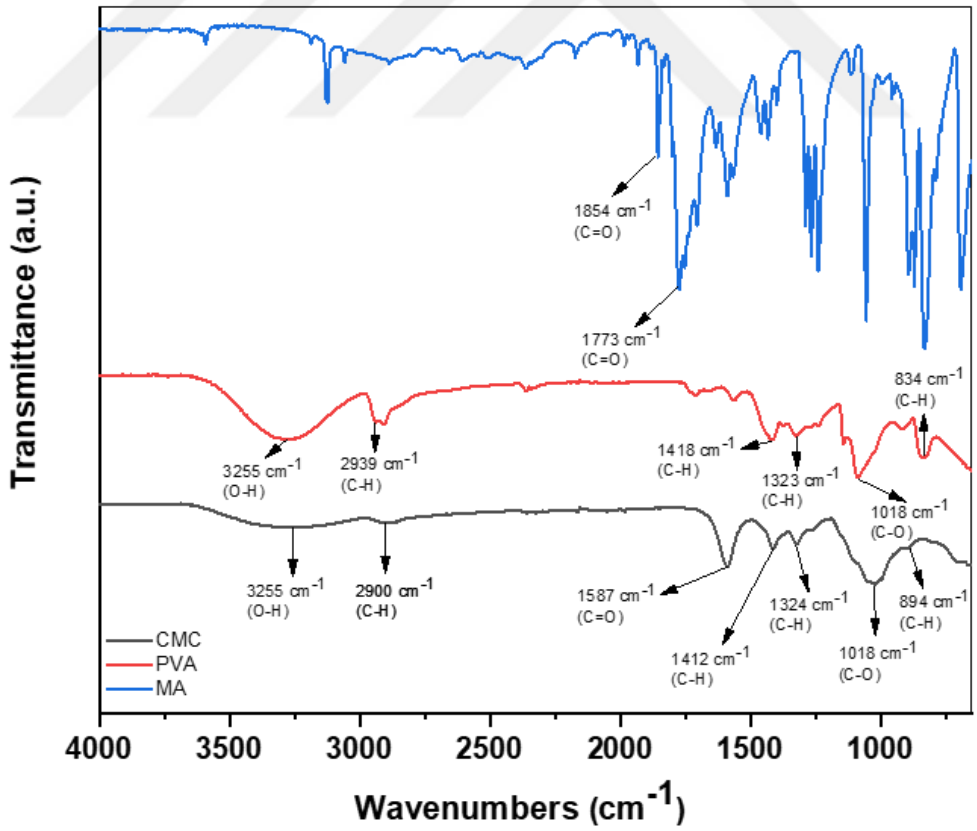

Figure 4.36. FTIR spectra of CMC, PVA and MA.

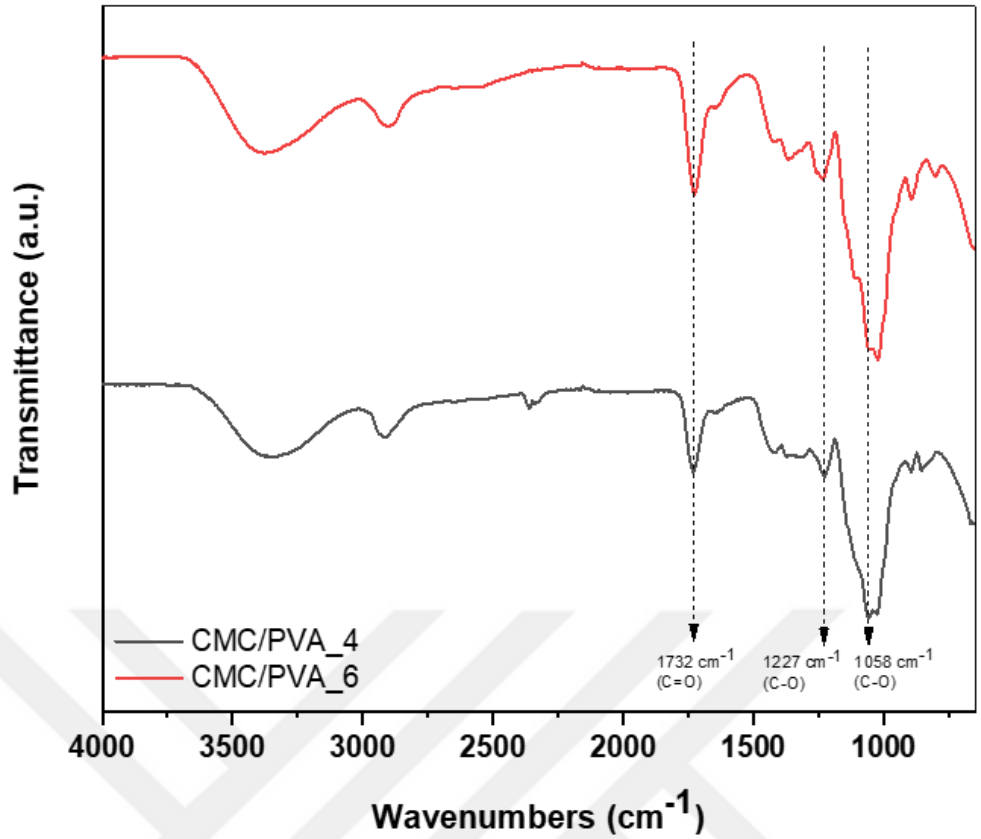

Figure 4.37. FTIR spectra of MA crosslinked CMC/PVA hybrid aerogels.

The FTIR spectra of CMC/PVA hybrid aerogels (Figure 4.37) showed that new peaks arose at 1732 cm^{-1} (C=O), 1227 cm^{-1} (C-O), and 1058 cm^{-1} (C-O), which indicated the formation of ester bonds between the hydroxyl groups of CMC and PVA and carboxyl groups of MA [98]. Additionally, no peaks at 1854 cm^{-1} and 1773 cm^{-1} confirmed the absence of non-reacted maleic anhydride [138].

The chemical structure and symbolic representation of carbon atoms of PVA and the solid state 13C-NMR spectrum of CMC/PVA hybrid aerogel are given in Figure 4.38. The carbon atom signals of PVA, which are between 60-80 ppm (Ca) and 46.16 ppm (Cb), were obtained from elsewhere [98]. The broad peak of CMC/PVA hybrid aerogel at 174.23 ppm indicated the ester formation.

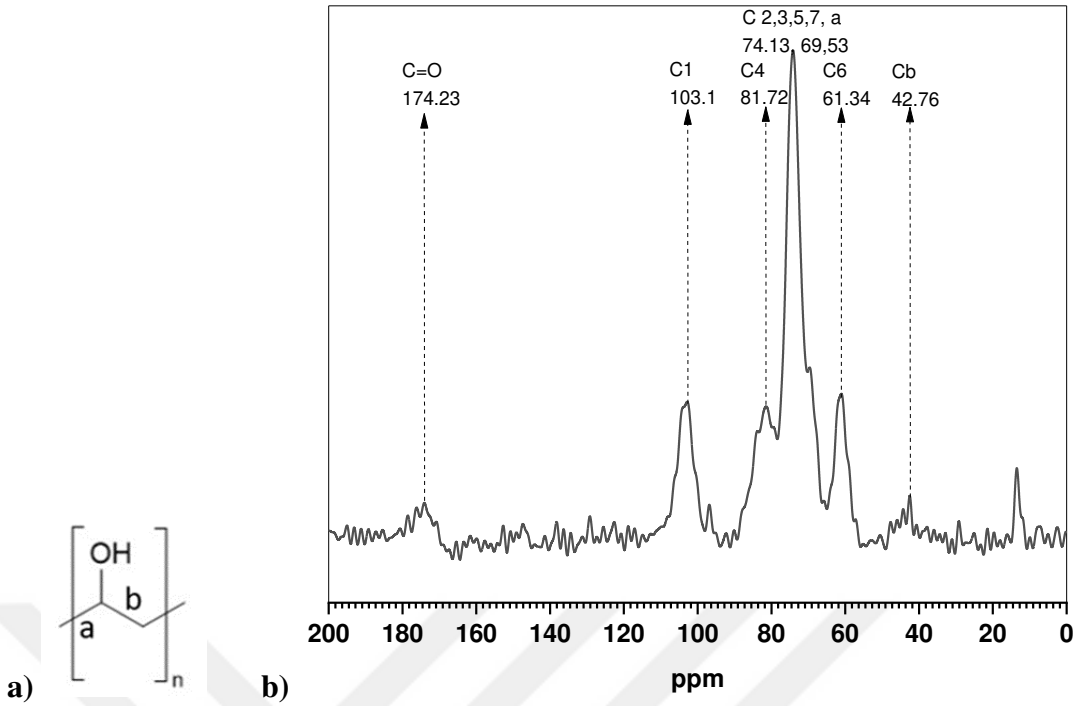

Figure 4.38. a) The chemical structure of PVA b) The solid-state 13C-NMR spectrum of CMC/PVA hybrid aerogel.

4.9.3 Thermal properties of CMC/PVA hybrid aerogels

The thermal conductivity of CMC/PVA6 aerogel was measured as 0.055 W/mK, which was slightly higher than CMC aerogel, which may be attributed to the higher macropore volume and larger average pore diameter of CMC/PVA6 aerogel.

4.10 Effect of acid catalyst on CMC aerogels

Sulfuric acid serves as a catalyst in esterification reactions by protonating the carboxyl group of the carboxylic acid, making it more electrophilic and thus more reactive towards nucleophilic attack. Additionally, sulfuric acid can also act as a dehydrating agent, helping to drive off water formed in the reaction, which can further push the equilibrium towards ester formation, thereby enhancing the efficiency of the esterification process.

Hydrogel, alcogel, and aerogel images obtained using sulfuric acid as a catalyst are given in Figure 4.39. Unlike CMC aerogels, no voids were observed on the outer surfaces of the aerogels obtained by acid catalysis. In addition, it was observed that sulfuric acid reduced gelation time to 3 FT cycles.

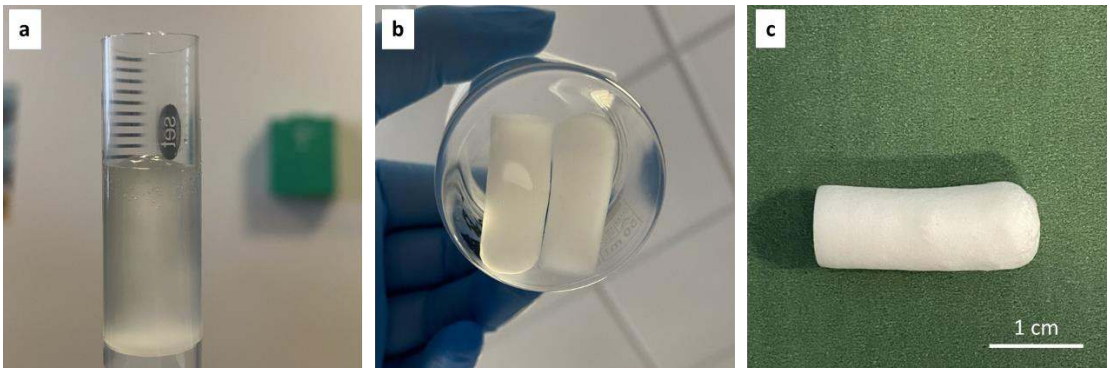

Figure 4.39. The sulfuric acid catalyzed a) hydrogel b) alcogel c) aerogel.

4.10.1 Morphology of sulfuric acid catalyzed CMC aerogels

The volumetric shrinkages and densities of sulfuric acid catalyzed CMC aerogels are illustrated in Figure 4.40. Contrary to expectations, it was observed that the volumetric shrinkage of aerogels with sulfuric acid was close to that of aerogels without sulfuric acid addition. Additionally, as the sulfuric acid concentration increased, the volumetric shrinkage decreased. The increase in the sulfuric acid concentration also increased the bulk density.

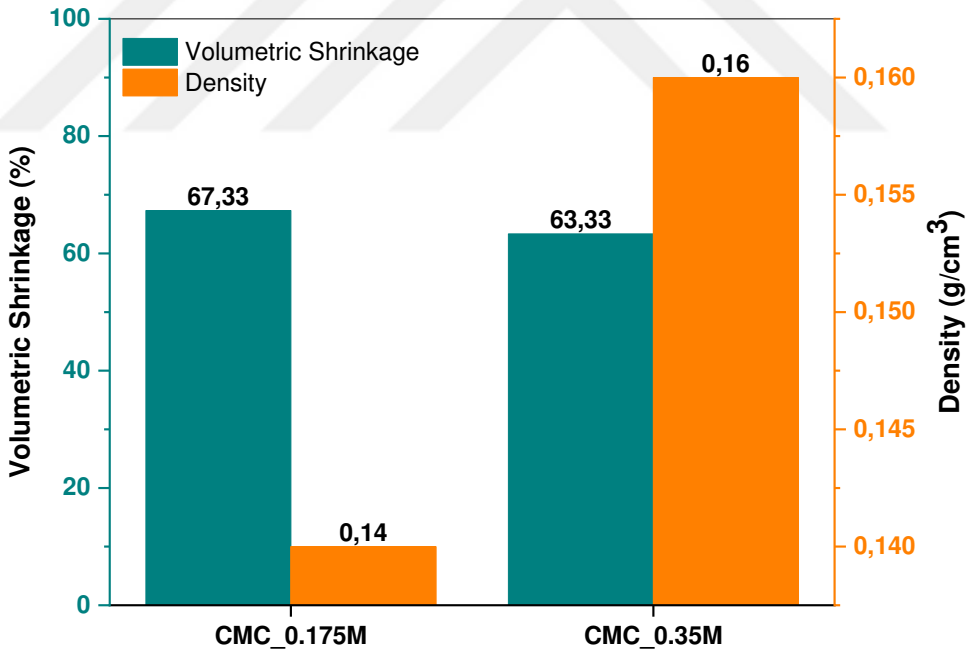

Figure 4.40. Volumetric shrinkages and densities of sulfuric acid catalyzed CMC aerogels.

The pore properties and the specific surface area (S_{BET}) of CMC aerogels were determined by N_2 physisorption and are listed in Table 4.6. Incorporating sulfuric acid as a catalyst resulted in notable alterations to the structural properties of the aerogels. Specifically, it was observed that sulfuric acid reduced porosity, specific surface area, and

total pore volume within the aerogel matrix. After the addition of sulfuric acid, the exchange of Na^+ and H^+ generated more carboxylic acid groups, which led to enhanced hydrogen bonding between the closely arranged polymers. This phenomenon suggested a significant formation of dense, non-porous polymer regions. Additionally, the average pore sizes of the aerogels were increased.

Table 4.6. Properties of sulfuric acid catalyzed CMC aerogels.

Sample	Skeletal Density (g/cm^3)	Porosity (%)	S_{BET} (m^2/g)	Single point pore Volume (cm^3/g)	Total Pore Volume (cm^3/g)	Macropore Volume (cm^3/g)	Average Pore Size - BJH (nm)	Average Pore Size - Macropore (nm)
CMC_0.175M	1.65	91.5	14	0.09	6.54	6.45	25.67	1909
CMC_0.35M	1.65	90.3	14	0.10	5.64	5.5	28.09	1613

The adsorption-desorption isotherms (illustrated in Figure 4.41) revealed that CMC aerogels catalyzed by sulfuric acid exhibited Type IV isotherms, suggesting the presence of mesopores. Furthermore, the difference between the BJH pore volume and the total pore volume (Table 4.6) suggested the presence of macropores.

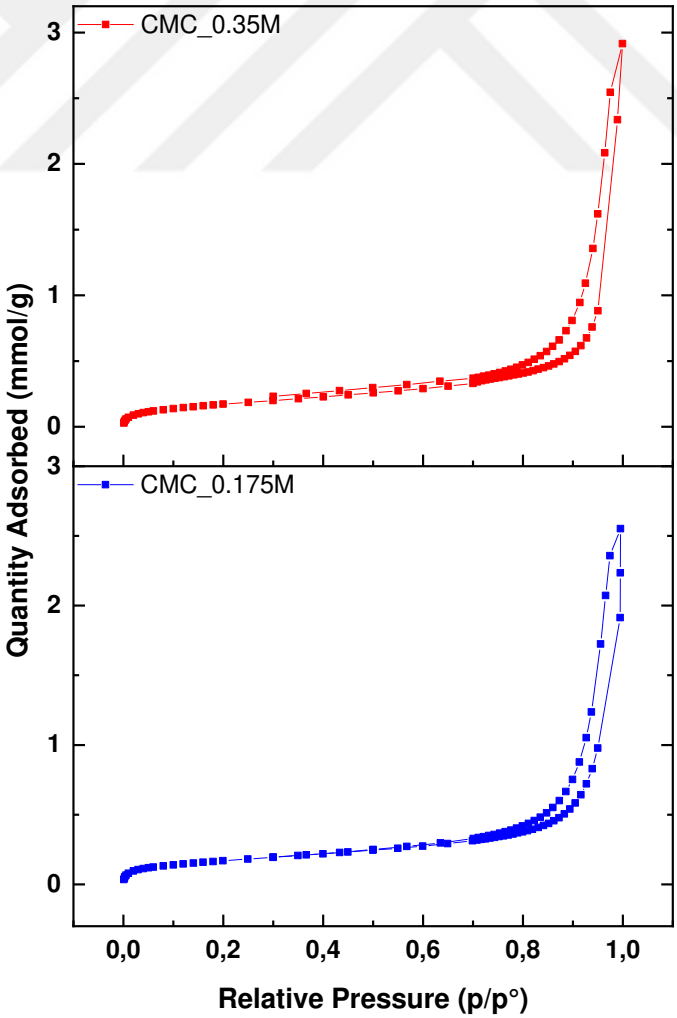

Figure 4.41. BET Isotherms of sulfuric acid catalyzed CMC aerogels.

Figure 4.42 presents the mesoporous pore size distributions of sulfuric acid catalyzed CMC aerogels, which were differential pore volumes plotted against the pore width. The pore size distribution, valid only for mesopores, showed a broad range with a peak around 30 nm.

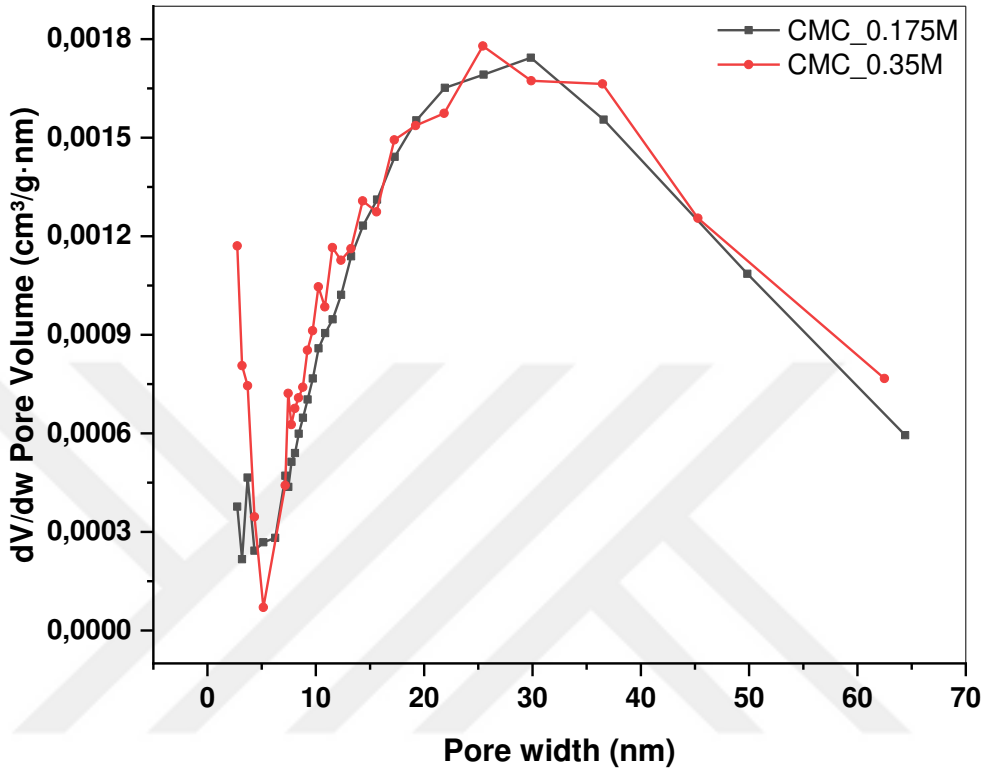

Figure 4.42. Mesoporous pore size distributions of sulfuric acid catalyzed CMC aerogels.

The presence of macroporous structures within the sulfuric acid catalyzed CMC aerogels was further supported by SEM analysis (Figure 4.43). The SEM images revealed fibrous structures characterized by interconnected networks featuring a combination of mesopores and macropores.

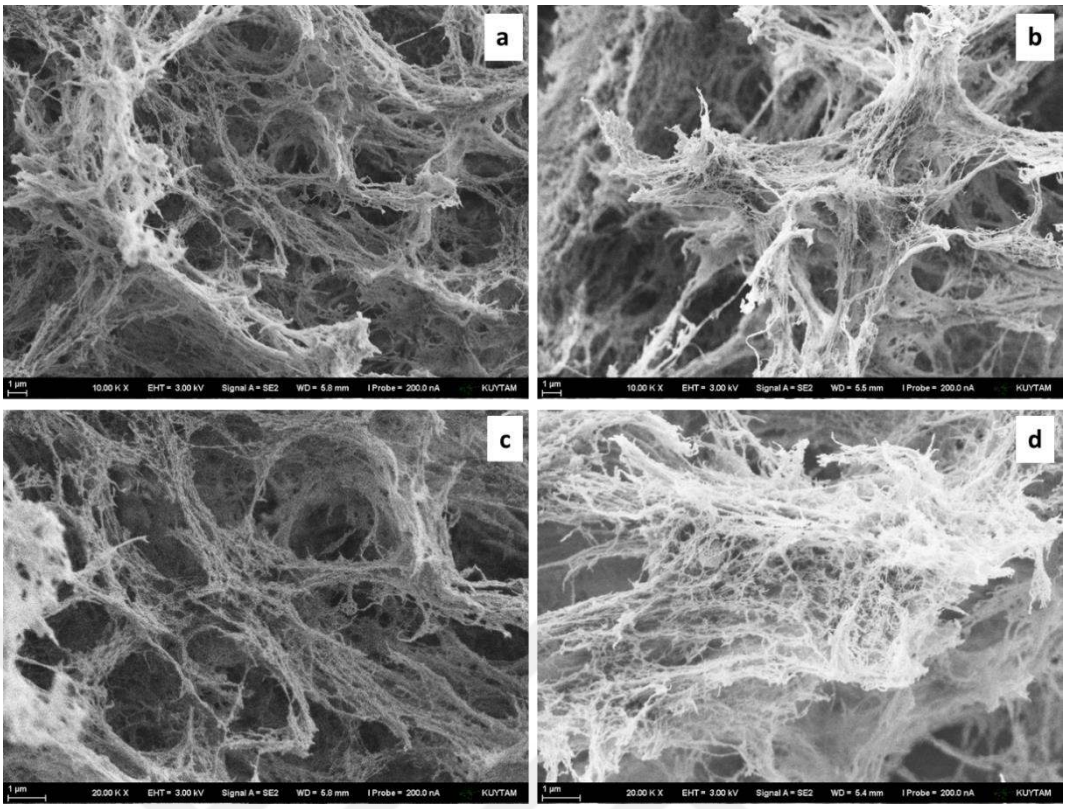

Figure 4.43. SEM images of sulfuric acid catalyzed CMC aerogels (a,c) 0.175M and (b,d) 0.35M.

4.10.2 Crosslinking of acid catalyzed CMC aerogels

The FTIR spectra of sulfuric acid catalyzed CMC aerogels (as illustrated in Figure 4.44) revealed the emergence of additional peaks at 1729 cm^{-1} (C=O), 1228 cm^{-1} (C-O), and 1054 cm^{-1} (C-O). These findings confirmed the formation of ester bonds between the hydroxyl groups of CMC and carboxyl groups of MA [98]

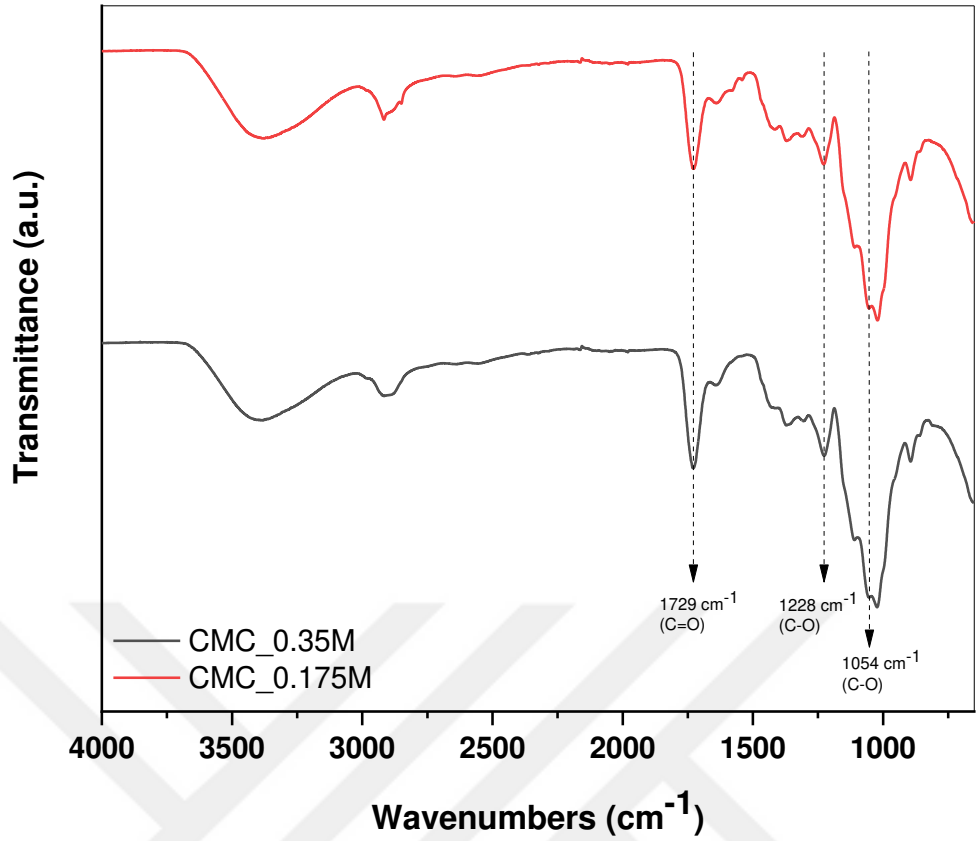

Figure 4.44. FTIR spectra of sulfuric acid catalyzed CMC aerogels.

4.10.3 Thermal properties of sulfuric acid catalyzed CMC aerogels

The thermal conductivities of sulfuric acid catalyzed CMC aerogels are presented in Table 4.7. Although the 0.35M acid catalyzed aerogel exhibited high density and low porosity, its thermal conductivity was lower than that of the 0.175M acid catalyzed aerogel. This can be ascribed to its higher ratio of mesopore volume to macropore volume. Furthermore, smaller average pore sizes likely contributed to its reduced thermal conductivity.

Table 4.7. The thermal conductivities of sulfuric acid catalyzed CMC aerogels

Sample	Thermal Conductivity (W/mK)
CMC_0.175M	0.066
CMC_0.35M	0.057

CHAPTER 5 CONCLUSION

In this study, low density, open porous carboxymethyl cellulose aerogels were successfully fabricated by the freeze-thaw induced gelation method followed by supercritical CO_2 drying. Maleic anhydride was used as a crosslinker to obtain covalently bonded gels, and the influence of the crosslinker concentration on CMC gelation and aerogel properties was examined. The impact of frozen storage time on the gelation of CMC was thoroughly explored in this study. Furthermore, our investigation delved into the effect of the molecular weight of CMC and the initial concentration of the solution, shedding light on gelation and pore properties. Additionally, the impacts of intermolecular crosslinking and acid catalysts were studied.

Our findings indicated that higher crosslinker concentrations reduced the number of freeze-thaw cycles required for hydrogel preparation. Moreover, prolonged frozen storage times diminished the requisite freeze-thaw cycles. Furthermore, higher molecular weight and CMC concentration resulted in a reduced number of freeze-thaw cycles needed for gel formation while concurrently enhancing the strength of the gel produced.

The bulk densities of CMC aerogels were measured between 0.051 and 0.204 g/cm^3, with high porosities (>93). The results showed that increasing crosslinker concentration increased the gel stability and decreased the swelling during solvent exchange, which caused a decrease in the pore diameter. Prepared aerogels showed specific surface areas in the range of 49.5 m^2/g and 214 m^2/g, which are also close to the other polysaccharide aerogels. SEM analysis showed that the porous network morphology of CMC aerogels depended on crosslinker concentration. Therefore, changing the crosslinker concentration may provide tuning of the aerogel pore properties. Furthermore, the study revealed a clear inverse relationship between solid content and porosity in CMC aerogels. Additionally, the increase in solid content and molecular weight generally led to reductions in specific pore volume. FTIR and NMR analysis also supported the proposed crosslinking reaction between CMC and MA; moreover, it proved

ester linkages between the hydroxyl groups of CMC and carboxyl groups of MA. The thermal conductivity values, which were used as a relative indicator, were measured between 0.038 and 0.051 W/mK.

CMC/PVA hybrid aerogels were prepared from 4 and 6 wt% aqueous solutions, and the bulk densities of these aerogels were 0.079 and 0.054 g/cm^3, respectively. The specific surface areas were measured as 184 and 144 m^2/g. The results showed that incorporating PVA increased the macropore volume and average pore size. FTIR and NMR analysis confirmed the proposed esterification reaction between CMC, PVA and MA. The thermal conductivity of CMC/PVA hybrid aerogel was measured as 0.055 W/mK.

Sulfuric acid was used as a catalyst to increase the esterification reaction rate and improve the crosslinking. Two distinct concentrations of sulfuric acid, 0.175 M and 0.35 M, were evaluated. The introduction of sulfuric acid as a catalyst led to a notable reduction in gelation time, achieving a cycle time of 3 FT. Remarkably, the surfaces of the prepared hydrogels, alcogels, and aerogels exhibited a uniform structure without any voids. The bulk densities measured were 0.14 g/cm³ and 0.16 g/cm³, while porosities surpassed 90%. Surprisingly, despite these favorable characteristics, the specific surface area and pore volume significantly decreased with the addition of sulfuric acid.

In light of these studies, the thermal conductivity of aerogels can be reduced by decreasing the macropore volume and increasing the mesopore volume. Aerogels with better thermal insulation properties can be obtained by preparing low-concentration solutions with high molecular weight carboxymethyl celluloses. Additionally, the influence of the degree of substitutions on gelation and aerogel properties should be investigated. Exploring the impact of lower concentrations of acid catalysts, as well as different acid types, would provide valuable insights. Further understanding and improvement of the crosslinking mechanism are still necessary. Moreover, it is essential to evaluate the thermal conductivity of CMC aerogels using a heat flow meter, a method known for its higher accuracy.

Bibliography

[1] BP PLC. Statistical Review of World Energy 2023. Vol. 70, BP Energy Outlook 2023. 2023. p. 8–20.

[2] IEA. Energy Efficiency Indicators Highlights 2020 [Internet]. 2020. Available from: https://www.iea.org/reports/energy-efficiency-indicators

[3] In focus: A new generation of EU energy labels [Internet]. 2020 [cited 2020 Aug 17]. Available from: https://ec.europa.eu/info/news/focus-new-generation-eu-energy-labels-2020-aug-13_en

[4] Liang Y, Wu H, Huang G, Yang J, Wang H. Thermal performance and service life of vacuum insulation panels with aerogel composite cores. Energy Build [Internet]. 2017;154:606–17. Available from: https://doi.org/10.1016/j.enbuild.2017.08.085

[5] Kistler SS. Coherent Expanded Aerogels. J Phys Chem. 1928;318(1896):52–64.

[6] Hüsing N, Schubert U. Aerogels - Airy Materials: Chemistry, Structure, and Properties. Angew Chemie - Int Ed. 1998;37(1–2):22–45.

[7] Smirnova I, Gurikov P. Aerogel production: Current status, research directions, and future opportunities. J Supercrit Fluids. 2018;134:228–33.

[8] Baetens R, Jelle BP, Gustavsen A. Aerogel insulation for building applications: A state-of-the-art review. Vol. 43, Energy and Buildings. 2011. p. 761–9.

[9] Jones SM. Aerogel: Space exploration applications. In: Journal of Sol-Gel Science and Technology. 2006. p. 351–7.

[10] Feng J, Le D, Nguyen ST, Tan Chin Nien V, Jewell D, Duong HM. Silica–cellulose hybrid aerogels for thermal and acoustic insulation applications. Colloids Surfaces A Physicochem Eng Asp. 2016;506:298–305.

[11] Strobach E, Bhatia B, Yang S, Zhao L, Wang EN. High temperature annealing for structural optimization of silica aerogels in solar thermal applications. J Non Cryst Solids. 2017;462:72–7.

[12] Ulker Z, Erkey C. An advantageous technique to load drugs into aerogels: Gas antisolvent crystallization inside the pores. J Supercrit Fluids. 2017 Feb 1;120:310–9.

[13] Ulker Z, Erkey C. An emerging platform for drug delivery: Aerogel based systems. J Control Release. 2014;177(1):51–63.

[14] Mirtaghavi A, Luo J, Muthuraj R. Recent Advances in Porous 3D Cellulose Aerogels for Tissue Engineering Applications: A Review. J Compos Sci. 2020;4(4):152.

[15] Bozbag SE, Zhang LC, Aindow M, Erkey C. Carbon aerogel supported nickel nanoparticles and nanorods using supercritical deposition. J Supercrit Fluids. 2012 Jun 1;66:265–73.

[16] Barım ŞB, Bayrakçeken A, Bozbağ SE, Zhang L, Kızılel R, Aindow M, et al. Control of average particle size of carbon aerogel supported platinum nanoparticles by supercritical deposition. Microporous Mesoporous Mater. 2017 Jun 1;245:94–103.

[17] Ünsal S, Yağcı MB, Bozbağ SE, Deljoo B, Aindow M, Erkey C. Supercritical Deposition Coupled with Ammonia Treatment: A New Route to Co-Promoted N-Doped Carbon Aerogels with High Oxygen Reduction Reaction Activity. Energy Technol. 2019 Nov 1;7(11):1900450.

[18] Barim SB, Raptapoulos G, Rommel S, Aindow M, Paraskevopoulou P, Erkey C. Polyamide aerogel-derived n-doped carbon aerogel decorated with platinum nanoparticles as highly active and stable electrocatalysts for oxygen reduction reaction. Electrochim Acta. 2022 Dec 1;434:141251.

[19] Barim SB, Bozbag SE, Yu H, Kızılel R, Aindow M, Erkey C. Mesoporous carbon aerogel supported PtCu bimetallic nanoparticles via supercritical deposition and their dealloying and electrocatalytic behaviour. Catal Today. 2018 Jul 15;310:166–75.

[20] Sarac Oztuna FE, Barim SB, Bozbag SE, Yu H, Aindow M, Unal U, et al. Graphene Aerogel Supported Pt Electrocatalysts for Oxygen Reduction Reaction by Supercritical Deposition. Electrochim Acta. 2017 Oct 1;250:174–84.

[21] Lee JH, Park SJ. Recent advances in preparations and applications of carbon aerogels: A review. Carbon N Y. 2020;163:1–18.

[22] Yousefzadeh H, Akgün IS, Barim SB, Sari TB, Eris G, Uzunlar E, et al. Supercritical fluid reactive deposition: A process intensification technique for

synthesis of nanostructured materials. Chem Eng Process - Process Intensif. 2022 Jun 1;176:108934.

[23] Anas M, Gönel AG, Bozbag SE, Erkey C. Thermodynamics of Adsorption of Carbon Dioxide on Various Aerogels. J CO2 Util. 2017 Oct 1;21:82–8.

[24] Jayne D, Zhang Y, Haji S, Erkey C. Dynamics of removal of organosulfur compounds from diesel by adsorption on carbon aerogels for fuel cell applications. Int J Hydrogen Energy. 2005 Sep 1;30(11):1287–93.

[25] Maleki H. Recent advances in aerogels for environmental remediation applications: A review. Chem Eng J. 2016;300:98–118.

[26] Yang J, Li Y, Zheng Y, Xu Y, Zheng Z, Chen X, et al. Versatile Aerogels for Sensors. Small. 2019;15(41).

[27] Biener J, Stadermann M, Suss M, Worsley MA, Biener MM, Rose KA, et al. Advanced carbon aerogels for energy applications. Energy Environ Sci. 2011;4(3):656–67.

[28] Alwin S, Sahaya Shajan X. Aerogels: promising nanostructured materials for energy conversion and storage applications. Mater Renew Sustain Energy. 2020;9(2).

[29] Ratke L, Gurikov P. Introduction. In: The Chemistry and Physics of Aerogels [Internet]. Cambridge University Press; 2021. p. 1–10. Available from: https://www.cambridge.org/core/product/identifier/9781108778336%23c1/type/book_part

[30] Pierre A.C. RA. SiO2 Aerogels. In: Aegerter M., Leventis N. KM, editor. Aerogels Handbook Advances in Sol-Gel Derived Materials and Technologies. Springer, New York, NY; 2011. p. 21–45.

[31] Pekala RW. Organic aerogels from the polycondensation of resorcinol with formaldehyde. J Mater Sci. 1989;24(9):3221–7.

[32] Mulik S. S-LC. Resorcinol–Formaldehyde Aerogels. In: Aegerter M., Leventis N. KM, editor. Aerogels Handbook Advances in Sol-Gel Derived Materials and Technologies. Springer, New York, NY; 2011. p. 215–34.

[33] Ganesan K, Budtova T, Ratke L, Gurikov P, Baudron V, Preibisch I, et al.

Review on the production of polysaccharide aerogel particles. Materials (Basel). 2018;11(11):1–37.

[34] Schwan M, Nefzger S, Zoghi B, Oligschleger C, Milow B. Improvement of Solvent Exchange for Supercritical Dried Aerogels. Front Mater. 2021;8(April):1–13.

[35] Şahin İ, Özbakır Y, İnönü Z, Ulker Z, Erkey C. Kinetics of Supercritical Drying of Gels. Gels. 2017;4(1):3.

[36] Gurikov P, S. P. R, Griffin JS, Steiner SA, Smirnova I. 110th Anniversary: Solvent Exchange in the Processing of Biopolymer Aerogels: Current Status and Open Questions. Ind Eng Chem Res. 2019;58(40):18590–600.

[37] Tripathi A, Parsons GN, Khan SA, Rojas OJ. Synthesis of organic aerogels with tailorable morphology and strength by controlled solvent swelling following Hansen solubility. Sci Rep. 2018;8(1):2106.

[38] Zhu Z, M. B. F. Snellings G, M. Koebel M, J. Malfait W. Superinsulating Polyisocyanate Based Aerogels: A Targeted Search for the Optimum Solvent System. ACS Appl Mater & Interfaces. 2017 May 18;9(21):18222–30.

[39] Lebedev A, Suslova E, Troyankin A, Lovskaya D. Investigation of Aerogel Production Processes: Solvent Exchange under High Pressure Combined with Supercritical Drying in One Apparatus. Vol. 7, Gels. 2021.

[40] Subrahmanyam R, Gurikov P, Dieringer P, Sun M, Smirnova I. On the road to biopolymer aerogels—dealing with the solvent. Gels. 2015;1(2):291–313.

[41] García-González CA, Alnaief M, Smirnova I. Polysaccharide-based aerogels - Promising biodegradable carriers for drug delivery systems. Carbohydr Polym. 2011;86(4):1425–38.

[42] Robitzer M, David L, Rochas C, Di Renzo F, Quignard F. Nanostructure of Calcium Alginate Aerogels Obtained from Multistep Solvent Exchange Route. Langmuir. 2008 Oct 10;24(21):12547–52.

[43] Mehling T, Smirnova I, Guenther U, Neubert RHH. Polysaccharide-based aerogels as drug carriers. J Non Cryst Solids. 2009 Dec 1;355(50–51):2472–9.

[44] Bisson A, Rigacci A, Lecomte D, Rodier E, Achard P. Drying of Silica Gels to

Obtain Aerogels:Phenomenology and Basic Techniques. Dry Technol. 2003 Jan 6;21(4):593–628.

[45] Payanda Konuk O, Alsuhile AAAM, Yousefzadeh H, Ulker Z, Bozbag SE, García-González CA, et al. The effect of synthesis conditions and process parameters on aerogel properties. Front Chem. 2023;11(October):1–26.

[46] Maleki H, Durães L, Portugal A. An overview on silica aerogels synthesis and different mechanical reinforcing strategies. J Non Cryst Solids [Internet]. 2014;385:55–74. Available from: http://dx.doi.org/10.1016/j.jnoncrysol.2013.10.017

[47] Leventis N, Sotiriou-Leventis C, Zhang G, M. Rawashdeh A-M. Nanoengineering Strong Silica Aerogels. Nano Lett. 2002 Aug 23;2(9):957–60.

[48] Brunner G. Supercritical process technology related to energy and future directions – An introduction. J Supercrit Fluids. 2015 Jan 1;96:11–20.

[49] Jin H, Nishiyama Y, Wada M, Kuga S. Nanofibrillar cellulose aerogels. 2004;240:63–7.

[50] Ciftci D, Ubeyitogullari A, Huerta RR, Ciftci ON, Flores RA, Saldaña MDA. Lupin hull cellulose nanofiber aerogel preparation by supercritical CO2 and freeze drying. J Supercrit Fluids. 2017 Sep 1;127:137–45.

[51] Chang CJ, Day C-Y, Ko C-M, Chiu K-L. Densities and P-x-y diagrams for carbon dioxide dissolution in methanol, ethanol, and acetone mixtures. Fluid Phase Equilib [Internet]. 1997;131(1):243–58. Available from: https://www.sciencedirect.com/science/article/pii/S0378381296032086

[52] Stergar J, Maver U. Review of aerogel-based materials in biomedical applications. J Sol-Gel Sci Technol. 2016;77(3):738–52.

[53] Bedilo AF, Klabunde KJ. Synthesis of high surface area zirconia aerogels using high temperature supercritical drying. Nanostructured Mater. 1997;8(2):119–35.

[54] Jung H, Choi H, Kim S, Ki W, Park H. The effect of surfactant type and concentration on the pore structure of alumina aerogels. J Non Cryst Solids. 2023;610:122325.

[55] F. Baumann T, E. Gash A, C. Chinn S, M. Sawvel A, S. Maxwell R, H. Satcher J.

Synthesis of High-Surface-Area Alumina Aerogels without the Use of Alkoxide Precursors. Chem Mater. 2004 Dec 24;17(2):395–401.

[56] Zuo L, Zhang Y, Zhang L, Miao YE, Fan W, Liu T. Polymer/Carbon-Based Hybrid Aerogels: Preparation, Properties and Applications. Vol. 8, Materials. 2015. 6806–6848 p.

[57] Alnaief M, Alzaitoun MA, García-González CA, Smirnova I. Preparation of biodegradable nanoporous microspherical aerogel based on alginate. Carbohydr Polym [Internet]. 2011;84(3):1011–8. Available from: http://dx.doi.org/10.1016/j.carbpol.2010.12.060

[58] Rigacci A. AP. Cellulosic and Polyurethane Aerogels. In: Aegerter M., Leventis N. KM, editor. Aerogels Handbook Advances in Sol-Gel Derived Materials and Technologies. Springer, New York, NY; 2011. p. 191–214.

[59] Gavillon R, Budtova T. Aerocellulose: New highly porous cellulose prepared from cellulose-NaOH aqueous solutions. Biomacromolecules. 2008;9(1):269–77.

[60] Illera D, Mesa J, Gomez H, Maury H. Cellulose aerogels for thermal insulation in buildings: Trends and challenges. Coatings. 2018;8(10):1–13.

[61] Pekala RW, Alviso CT, Kong FM, Hulsey SS. Aerogels derived from multifunctional organic monomers. J Non Cryst Solids. 1992;145(C):90–8.

[62] Zhuo H, Hu Y, Tong X, Zhong L, Peng X, Sun R. Sustainable hierarchical porous carbon aerogel from cellulose for high-performance supercapacitor and CO2 capture. Ind Crops Prod [Internet]. 2016;87:229–35. Available from: http://dx.doi.org/10.1016/j.indcrop.2016.04.041

[63] Allahbakhsh A, Bahramian AR. Self-assembled and pyrolyzed carbon aerogels: An overview of their preparation mechanisms, properties and applications. Nanoscale. 2015;7(34):14139–58.

[64] Hu L, He R, Lei H, Fang D. Carbon Aerogel for Insulation Applications: A Review. Int J Thermophys. 2019;40(4):1–25.

[65] Biesmans G. Polyurethane based organic aerogels and their transformation into carbon aerogels. 1998;64–8.

[66] Leventis N. LH. Polymer-Crosslinked Aerogels. In: Aegerter M., Leventis N.

KM, editor. Aerogels Handbook Advances in Sol-Gel Derived Materials and Technologies. Springer, New York, NY; 2011. p. 251–85.

[67] Mackenzie JD, Angeles L. Hybrid Organic — Inorganic Materials The Sol — Gel Approach. 2000;226–36.

[68] Demilecamps A, Beauger C, Hildenbrand C, Rigacci A, Budtova T. Cellulose-silica aerogels. Carbohydr Polym [Internet]. 2015;122:293–300. Available from: http://dx.doi.org/10.1016/j.carbpol.2015.01.022

[69] Yao C.J., Liu X. RWM. Biopolymer-Containing Aerogels: Chitosan-Silica Hybrid Aerogels. In: Aegerter M., Leventis N. KM, editor. Aerogels Handbook Advances in Sol-Gel Derived Materials and Technologies. Springer, New York, NY; 2011. p. 385–401.

[70] He YL, Xie T. Advances of thermal conductivity models of nanoscale silica aerogel insulation material. Appl Therm Eng [Internet]. 2015;81:28–50. Available from: http://dx.doi.org/10.1016/j.applthermaleng.2015.02.013

[71] Tang GH, Bi C, Zhao Y, Tao WQ. Thermal transport in nano-porous insulation of aerogel: Factors, models and outlook. Energy. 2015;90:701–21.

[72] Zhao JJ, Duan YY, Wang XD, Zhang XR, Han YH, Gao Y Bin, et al. Optical and radiative properties of infrared opacifier particles loaded in silica aerogels for high temperature thermal insulation. Int J Therm Sci [Internet]. 2013;70:54–64. Available from: http://dx.doi.org/10.1016/j.ijthermalsci.2013.03.020

[73] Inonu Z, Keskin S, Erkey C. An Emerging Family of Hybrid Nanomaterials: Metal-Organic Framework/Aerogel Composites. ACS Appl Nano Mater. 2018;1(11):5959–80.

[74] Luo X, Shen J, Ma Y, Liu L, Meng R, Yao J. Robust, sustainable cellulose composite aerogels with outstanding flame retardancy and thermal insulation. Carbohydr Polym [Internet]. 2020;230(July 2019):115623. Available from: https://doi.org/10.1016/j.carbpol.2019.115623

[75] Pinkert A, Marsh KN, Pang S, Staiger MP. Ionic liquids and their interaction with cellulose. Chem Rev. 2009;109(12):6712–28.

[76] Lindman B, Karlström G, Stigsson L. On the mechanism of dissolution of cellulose. J Mol Liq [Internet]. 2010;156(1):76–81. Available from:

http://dx.doi.org/10.1016/j.molliq.2010.04.016

[77] French AD. Glucose, not cellobiose, is the repeating unit of cellulose and why that is important. Cellulose. 2017;24(11):4605–9.

[78] Pircher N, Carbajal L, Schimper C, Bacher M, Rennhofer H, Nedelec JM, et al. Impact of selected solvent systems on the pore and solid structure of cellulose aerogels. Cellulose. 2016;23(3):1949–66.

[79] Duchemin BJC, Staiger MP, Tucker N, Newman RH. Aerocellulose based on all-cellulose composites. J Appl Polym Sci [Internet]. 2010 Jan 5;115(1):216–21. Available from: https://doi.org/10.1002/app.31111

[80] Sescousse R, Gavillon R, Budtova T. Aerocellulose from cellulose-ionic liquid solutions: Preparation, properties and comparison with cellulose-NaOH and cellulose-NMMO routes. Carbohydr Polym. 2011;83(4):1766–74.

[81] Seddiqi H, Oliaei E, Honarkar H, Jin J, Geonzon LC, Bacabac RG, et al. Cellulose and its derivatives: towards biomedical applications [Internet]. Vol. 28, Cellulose. Springer Netherlands; 2021. 1893–1931 p. Available from: https://doi.org/10.1007/s10570-020-03674-w

[82] Arca HC, Mosquera-Giraldo LI, Bi V, Xu D, Taylor LS, Edgar KJ. Pharmaceutical Applications of Cellulose Ethers and Cellulose Ether Esters. Biomacromolecules. 2018;19(7):2351–76.

[83] Jain S, Sandhu PS, Malvi R, Gupta B. Cellulose derivatives as thermoresponsive polymer: An overview. J Appl Pharm Sci. 2013;3(12):139–44.

[84] Feller R, Wilt M. Evaluation of Cellulose Ethers for Conservation [Internet]. Vol. 3, Research in Conservation. 1990. 1–161 p. Available from: http://www.bcin.ca/Interface/openbcin.cgi?submit=submit&Chinkey=109521

[85] Zhang W, Liu Y, Xuan Y, Zhang S. Synthesis and Applications of Carboxymethyl Cellulose Hydrogels. Gels. 2022;8(529).

[86] Chang C, Zhang L. Cellulose-based hydrogels: Present status and application prospects. Carbohydr Polym [Internet]. 2011;84(1):40–53. Available from: http://dx.doi.org/10.1016/j.carbpol.2010.12.023

[87] Książek E. Citric Acid: Properties, Microbial Production, and Applications in

Industries. Molecules. 2024;29(1):22.

[88] Ghanbarzadeh B, Almasi H, Entezami AA. Improving the barrier and mechanical properties of corn starch-based edible films: Effect of citric acid and carboxymethyl cellulose. Ind Crops Prod [Internet]. 2011;33(1):229–35. Available from: http://dx.doi.org/10.1016/j.indcrop.2010.10.016

[89] Pérez-Calderón J, Santos MV, Zaritzky N. Synthesis, characterization and application of cross-linked chitosan/oxalic acid hydrogels to improve azo dye (Reactive Red 195) adsorption. React Funct Polym [Internet]. 2020;155(June):104699. Available from: https://doi.org/10.1016/j.reactfunctpolym.2020.104699

[90] Enache AA, Serbezeanu D, Vlad-Bubulac T, Ipate AM, Suflet DM, Drobotă M, et al. Tunable Properties via Composition Modulations of Poly(vinyl alcohol)/Xanthan Gum/Oxalic Acid Hydrogels. Materials (Basel). 2022;15(7):2657.

[91] Popescu I, Constantin M, Pelin IM, Suflet DM, Ichim DL, Daraba OM, et al. Eco-Friendly Synthesized PVA/Chitosan/Oxalic Acid Nanocomposite Hydrogels Embedding Silver Nanoparticles as Antibacterial Materials. Gels. 2022;8(5).

[92] Diciccio AM, Coates GW. Ring-opening copolymerization of maleic anhydride with epoxides: A chain-growth approach to unsaturated polyesters. J Am Chem Soc. 2011;133(28):10724–7.

[93] Bettahar F, Bekkar F, Pérez-Álvarez L, Ferahi MI, Meghabar R, Vilas-Vilela JL, et al. Tough hydrogels based on maleic anhydride, bulk properties study and microfiber formation by electrospinning. Polymers (Basel). 2021;13(6).

[94] Zhang W, Li G, Fang Y, Wang X. Maleic anhydride surface-modification of crosslinked chitosan membrane and its pervaporation performance. J Memb Sci. 2007;295(1–2):130–8.

[95] Ayouch I, Kassem I, Kassab Z, Barrak I, Barhoun A, Jacquemin J, et al. Crosslinked carboxymethyl cellulose-hydroxyethyl cellulose hydrogel films for adsorption of cadmium and methylene blue from aqueous solutions. Surfaces and Interfaces [Internet]. 2021;24(March):101124. Available from: https://doi.org/10.1016/j.surfin.2021.101124

[96] Liuyun J, Yubao L, Chengdong X. Preparation and biological properties of a novel composite scaffold of nano-hydroxyapatite/chitosan/carboxymethyl cellulose for bone tissue engineering. J Biomed Sci. 2009;16(1):1–10.

[97] Congming Xiao YGC. Preparation and Properties of Physically Crosslinked Sodium Carboxymethylcellulose/Poly(vinyl alcohol) Complex Hydrogels. J Appl Polym Sci. 2007;107:1568–1572.

[98] Ghorpade VS, Dias RJ, Mali KK, Mulla SI. Citric acid crosslinked carboxymethylcellulose-polyvinyl alcohol hydrogel films for extended release of water soluble basic drugs. J Drug Deliv Sci Technol. 2019;52(March):421–30.

[99] Baldino L, Zuppolini S, Cardea S, Diodato L, Borriello A, Reverchon E, et al. Production of biodegradable superabsorbent aerogels using a supercritical CO2 assisted drying. J Supercrit Fluids [Internet]. 2020;156:104681. Available from: https://doi.org/10.1016/j.supflu.2019.104681

[100] Li J, Chen F, Lin X, Ding T. Hydrogen-bonding-assisted toughening of hierarchical carboxymethyl cellulose hydrogels for biomechanical sensing. Carbohydr Polym [Internet]. 2021;269(May):118252. Available from: https://doi.org/10.1016/j.carbpol.2021.118252

[101] Christian Demitri, Roberta Del Sole, Francesca Scalera, Alessandro Sannino, Giuseppe Vasapollo, Alfonso Maffezzoli, Luigi Ambrosio LN. Novel Superabsorbent Cellulose-Based Hydrogels Crosslinked with Citric Acid. J Appl Polym Sci. 2008;110:2453–60.

[102] Seki Y, Altinisik A, Demircioğlu B, Tetik C. Carboxymethylcellulose (CMC)-hydroxyethylcellulose (HEC) based hydrogels: Synthesis and characterization. Cellulose. 2014;21(3):1689–98.

[103] Wang C, Ma R, Huang Z, Liu X, Wang T, Chen K. Preparation and characterization of carboxymethylcellulose based citric acid cross-linked magnetic aerogel as an efficient dye adsorbent. Int J Biol Macromol [Internet]. 2021;181:1030–8. Available from: https://doi.org/10.1016/j.ijbiomac.2021.04.078

[104] Yu S, Budtova T. Creating and exploring carboxymethyl cellulose aerogels as drug delivery devices. Carbohydr Polym [Internet]. 2024;332(January):121925.

Available from: https://doi.org/10.1016/j.carbpol.2024.121925

[105] Lozinsky VI, Galaev IY, Plieva FM, Savina IN, Jungvid H, Mattiasson B. Polymeric cryogels as promising materials of biotechnological interest. Trends Biotechnol. 2003;21(10):445–51.

[106] Lozinsky, V.I., Okay O. Basic Principles of Cryotropic Gelation. Okay O, editor. Vol. 263, Advances in Polymer Science. Springer, Cham; 2014. 49–101 p.

[107] Zhao Y, Shen W, Chen Z, Wu T. Freeze-thaw induced gelation of alginates. Carbohydr Polym [Internet]. 2016;148:45–51. Available from: http://dx.doi.org/10.1016/j.carbpol.2016.04.047

[108] Szekalska M, Sosnowska K, Wróblewska M, Basa A, Winnicka K. Does the Freeze–Thaw Technique Affect the Properties of the Alginate/Chitosan Glutamate Gels with Posaconazole as a Model Antifungal Drug? Int J Mol Sci. 2022;23(12).

[109] Jiang F, Hsieh Y Lo. Super water absorbing and shape memory nanocellulose aerogels from TEMPO-oxidized cellulose nanofibrils via cyclic freezing-thawing. J Mater Chem A. 2014;2(2):350–9.

[110] Hassan CM, Peppas NA. Structure and morphology of freeze/thawed PVA hydrogels. Macromolecules. 2000;33(7):2472–9.

[111] Wang LY, Wang MJ. Removal of Heavy Metal Ions by Poly(vinyl alcohol) and Carboxymethyl Cellulose Composite Hydrogels Prepared by a Freeze-Thaw Method. ACS Sustain Chem Eng. 2016;4(5):2830–7.

[112] Ülker Z, Sanli D, Erkey C. Applications of Aerogels and Their Composites in Energy-Related Technologies. In: Supercritical Fluid Technology for Energy and Environmental Applications. Elsevier B.V.; 2014. p. 157–80.

[113] Razeghi M. Fundamentals of Solid State Engineering. 3rd Editio. Springer, New York, NY; 2009.

[114] HP. E. Thermal Properties of Aerogels. In: Aegerter M., Leventis N. KM, editor. Aerogels Handbook Advances in Sol-Gel Derived Materials and Technologies. Springer, New York, NY; 2011. p. 537–64.

[115] Zhang ZM. Nano/Microscale Heat Transfer. 2nd ed. Springer International

Publishing; 2020. XXVI, 761.

[116] Bi C, Tang GH. Effective thermal conductivity of the solid backbone of aerogel. Int J Heat Mass Transf. 2013;64:452–6.

[117] Dames C, Chen G. Theoretical phonon thermal conductivity of Si/Ge superlattice nanowires. J Appl Phys. 2004;95(2):682–93.

[118] Chen G. Thermal conductivity and ballistic-phonon transport in the cross-plane direction of superlattices. 1998;57(23):958–73.

[119] X. Lu, M. C. Arduini-Schuster, J. Kuhn, O. Nilsson JF and RWP. Thermal Conductivity of Monolithic Organic Aerogels. Science (80-). 1992;255(5047):971–2.

[120] Zeng SQ, Hunt A, Greif R. Mean free path and apparent thermal conductivity of a gas in a porous medium. J Heat Transfer. 1995;117(3):758–61.

[121] Kistler SS. The Relation between Heat Conductivity and Structure in Silica Aerogel. J Phys Chem. 1935;39(1):79–86.

[122] Swimm K, Vidi S, Reichenauer G, Ebert HP. Coupling of gaseous and solid thermal conduction in porous solids. J Non Cryst Solids [Internet]. 2017;456:114–24. Available from: http://dx.doi.org/10.1016/j.jnoncrysol.2016.11.012

[123] Lu X, Caps R, Fricke J, Alviso CT, Pekala RW. Correlation between structure and thermal conductivity of organic aerogels. J Non Cryst Solids. 1995;188(3):226–34.

[124] Bi C, Tang GH, Tao WQ. Prediction of the gaseous thermal conductivity in aerogels with non-uniform pore-size distribution. J Non Cryst Solids. 2012;358(23):3124–8.

[125] Zeng SQ, Hunt A, Greif R. Transport properties of gas in silica aerogel. J Non Cryst Solids. 1995;186:264–70.

[126] Guo JF, Tang GH. A theoretical model for gas-contributed thermal conductivity in nanoporous aerogels. Int J Heat Mass Transf [Internet]. 2019;137:64–73. Available from: https://doi.org/10.1016/j.ijheatmasstransfer.2019.03.106

[127] Howell, J.R., Mengüç M.P., Daun, K., Siegel R. Thermal Radiation Heat

Transfer. 7th ed. Boca Raton: CRC Press; 2020. 1040 p.

[128] Zhang H, Wang X, Li Y. Measuring radiative properties of silica aerogel composite from FTIR transmittance test using KBr as diluents. Exp Therm Fluid Sci [Internet]. 2018;91(September 2017):144–54. Available from: https://doi.org/10.1016/j.expthermflusci.2017.10.010

[129] Rahman MS, Hasan MS, Nitai AS, Nam S, Karmakar AK, Ahsan MS, et al. Recent developments of carboxymethyl cellulose. Polymers (Basel). 2021;13(8):1345.

[130] Groult S, Budtova T. Thermal conductivity/structure correlations in thermal super-insulating pectin aerogels. Carbohydr Polym [Internet]. 2018;196(March):73–81. Available from: https://doi.org/10.1016/j.carbpol.2018.05.026

[131] Davidovich-Pinhas M, Gravelle AJ, Barbut S, Marangoni AG. Temperature effects on the gelation of ethylcellulose oleogels. Food Hydrocoll [Internet]. 2015;46:76–83. Available from: http://dx.doi.org/10.1016/j.foodhyd.2014.12.030

[132] Gorgieva S, Kokol V. Synthesis and application of new temperature-responsive hydrogels based on carboxymethyl and hydroxyethyl cellulose derivatives for the functional finishing of cotton knitwear. Carbohydr Polym [Internet]. 2011;85(3):664–73. Available from: http://dx.doi.org/10.1016/j.carbpol.2011.03.037

[133] Sarkar N. Thermal gelation properties of methyl and hydroxypropyl methylcellulose. J Appl Polym Sci. 1979;24(4):1073–87.

[134] Benslimane A, Bahlouli IM, Bekkour K, Hammiche D. Thermal gelation properties of carboxymethyl cellulose and bentonite-carboxymethyl cellulose dispersions: Rheological considerations. Appl Clay Sci [Internet]. 2016;132–133:702–10. Available from: http://dx.doi.org/10.1016/j.clay.2016.08.026

[135] Tallon MA. Reactions Involving Maleic Anhydride. Musa OM, editor. Springer, Cham; 2016. 59–149 p.

[136] Horvat G, Pantić M, Knez Ž, Novak Z. A Brief Evaluation of Pore Structure Determination for Bioaerogels. Gels. 2022;8(7):1–18.

[137] Parker SF, Wilson CC, Tomkinson J, Keen DA, Shankland K, Facility I, et al.

Structure and Dynamics of Maleic Anhydride. J Phys Chem A. 2001;105(13):3064–70.

[138] de Melo JCP, da Silva Filho EC, Santana SAA, Airoldi C. Maleic anhydride incorporated onto cellulose and thermodynamics of cation-exchange process at the solid/liquid interface. Colloids Surfaces A Physicochem Eng Asp. 2009;346(1–3):138–45.

[139] Malfait WJ, Ebert HP, Brunner S, Wernery J, Galmarini S, Zhao S, et al. The poor reliability of thermal conductivity data in the aerogel literature: a call to action! J Sol-Gel Sci Technol. 2024;

[140] Lu X, Arduini-Schuster MC, Kuhn J, Nilsson O, Fricke J, Pekala RW. Thermal Conductivity of Monolithic Organic Aerogels. Science (80-). 1992;255(5047):971–2.

[141] Coquard R, Baillis D. Thermal conductivity of Kelvin cell cellulosic aerogels: analytical and Monte Carlo approaches. J Mater Sci. 2017;52(19):11135–45.

[142] Merillas B, Vareda JP, Martín-de León J, Rodríguez-Pérez MÁ, Durães L. Thermal Conductivity of Nanoporous Materials: Where Is the Limit? Polymers (Basel). 2022;14(13):2556.

APPENDIX

A1. Mass Loss Calculation

The mass loss values of CMC aerogels were calculated by using Equation A.1 as:

$$m_{loss}(\%) = \frac{(m_{CMC,gel}+m_{MA,gel})-m_{CMC,aerogel}}{(m_{CMC,gel}+m_{MA,gel})} \times 100 \quad \text{(A.1)}$$

where $m_{CMC,gel}$, $m_{MA,gel}$ and $m_{CMC,aerogel}$ are the mass of the CMC, MA, and aerogel, respectively and can be calculated from following equations:

$$m_{CMC,gel} = \frac{m_{CMC,sol}}{m_{CMC,sol}+m_{MA,sol}+m_{DIW,sol}} \times m_{gel} \quad \text{(A.2)}$$

$$m_{MA,gel} = \frac{m_{MA,sol}}{m_{CMC,sol}+m_{MA,sol}+m_{DIW,sol}} \times m_{gel} \quad \text{(A.3)}$$

$$m_{DIW,gel} = \frac{m_{DIW,sol}}{m_{CMC,sol}+m_{MA,sol}+m_{DIW,sol}} \times m_{gel} \quad \text{(A.4)}$$

where $m_{CMC,sol}$, $m_{MA,sol}$, and $m_{DIW,sol}$ are the mass of the CMC, MA, and DIW in solution, respectively, $m_{DIW,gel}$ is the mass of the DIW in gel, and m_{gel} is the mass of the gel.

A2. Theoretical Thermal Conductivity Calculation

The gas convection was neglected because the pore diameters of CMC aerogels were below 1 mm. The theoretical thermal conductivity values were calculated from Equation A.5 as:

$$\lambda_{aerogel} = (\lambda_{cmc} \times cmc(\%)) + (\lambda_{air} \times macropore(\%)) \quad \text{(A.5)}$$

where $\lambda_{aerogel}$, λ_{cmc}, and λ_{air} are the thermal conductivities of aerogel, CMC and air, respectively. λ_{cmc}, and λ_{air} were 100 W/mK and 26 W/mK, respectively [141][142].

$$cmc(\%) = \frac{V_{cmc}}{V_{total}} \quad \text{(A.6)}$$

$$macropore(\%) = \frac{V_{macropore}}{V_{total}} \quad \text{(A.7)}$$

where V_{cmc}, $V_{macropore}$, and V_{total} are the volume of CMC, macropores, and total in cm^3/g, respectively. V_{total} and V_{cmc} were calculated from the equations below:

$$V_{total} = \frac{1}{\rho_{aerogel}} \quad \text{(A.8)}$$

$$V_{cmc} = V_{total} - (V_{macropore} + V_{mesopore}) \quad \text{(A.9)}$$

where $V_{macropore}$ and $V_{mesopore}$ were obtained from N_2 physisorption.